

**IMPROVED MULTI INVERSION TIME ARTERIAL SPIN  
LABELING MRI OF THE BRAIN**

by

**Dilek Betül ARSLAN**

B.S., in Biomedical Engineering, Erciyes University, 2013

M.S., in Biomedical Engineering, Boğaziçi University, 2016

Submitted to the Institute of Biomedical Engineering

in partial fulfillment of the requirements

for the degree of

Doctor

of

Philosophy

Boğaziçi University

2021

## ACKNOWLEDGEMENTS

I would like to express my deep and sincere gratitude to my supervisor, Assoc. Prof. Dr. Esin Öztürk Işık, for her understanding and continuous support. It was a great privilege and honor to work under her guidance. I am extremely grateful for what she has offered me.

This thesis could not have been completed in its current form without the support of Prof. Dr. Matthias van Osch. His dynamic and methodological research approach has deeply inspired me. He has patiently taught me how to handle our research problem and to visualize what happens in the brain. Furthermore, I would like to thank the rest of my thesis committee members, Prof. Dr. Ahmet Ademođlu, Assoc. Prof. Dr. Özgür Kocatürk and Prof. Dr. Ibrahim Hakan Gürvit, for their encouragement and valuable suggestions. Additionally, I am very grateful to Prof. Dr. Ibrahim Hakan Gürvit for supporting and inspiring me during the process of writing my first article. I would like to thank Lena Václavů, whom I have had the pleasure of working with, for her support. Also, I was fortunate to be a part of the Leiden University Medical Center group for some time. Moreover, I would like to thank my colleagues, Sevim Cengiz and Gökçe Hale Hatay, for their guidance and friendship. Also, I would like to thank my friend Samet Aytaç for being with me with all his truth. I am also thankful to my mother, Gülser Arslan, for her support. She has always stood behind me. I am also thankful to Utku Sarıdede for his friendship, love, support and encouragement. He always motivated me while I was writing my thesis and was always there for me. I would not be brave enough to take the last step to complete my thesis without him.

This thesis was supported by TÜBİTAK project #115S219 and the Ministry of Development project #2010K120330, the EU under the Horizon2020 program (project: CDS-QUAMRI), and by Philips Healthcare.

## ACADEMIC ETHICS AND INTEGRITY STATEMENT

I, Dilek Betül Arslan, hereby certify that I am aware of the Academic Ethics and Integrity Policy issued by the Council of Higher (YÖK) and I fully acknowledge all the consequences due to its violation by plagiarism or any other way.

Name :

---

Signature:

---

Date:

---

## ABSTRACT

### IMPROVED MULTI INVERSION TIME ARTERIAL SPIN LABELING MRI OF THE BRAIN

Arterial spin labeling magnetic resonance imaging (ASL MRI) measures cerebral blood flow (CBF) quantitatively without using any contrast agent or radiation. The calculation of labelled blood arrival time to tissue and arterial vessels provides hemodynamic information, which may be useful in understanding neurodegenerative disorders. Separate pseudo-continuous ASL (pCASL) MR can be done at multiple inversion times (TI) to avoid inaccurate CBF estimation due to uncertainties in arrival times, which is time consuming and limits the number of averages. ASL MRI using Look-Locker (LL) readout and the time-encoded pCASL MRI (te-pCASL) using Hadamard matrix are two approaches for acquiring ASL data at multiple TIs. ASL-MRI with LL readout requires a complex model to accurately estimate CBF. On the other hand, te-pCASL MRI has a shine-through effect, which might cause errors in CBF estimation. In the first part of this thesis, the brain perfusion deficits in Parkinson's disease with mild cognitive impairment (PD-MCI) were investigated using ASL MRI with LL readout. PD-MCI patients displayed a posterior hypoperfusion pattern, which classified these patients with over 90% accuracy in comparison to healthy controls. Moreover, genetically risky PD with microtubule-associated protein tau gene (MAPT) H1/H1 haplotype had visual hypoperfusion as compared with non-risky PD. In the second part of the thesis, the possible reasons of shine-through effect in te-pCASL MRI were assessed using simulations and in-vivo data. Based on the theoretical model, pCASL and te-pCASL MRI resulted in the same ASL signals. On the other hand, our experimental results showed that the use of selective background suppression inversion pulses could lead to the appearance of the shine-through effect.

**Keywords:** Arterial spin labeling, Parkinson's disease, mild cognitive impairment, te-pCASL, Look-Locker readout, Parkinson's disease, shine-through effect.

## ÖZET

### BEYNİN GELİŞTİRİLMİŞ ÇOKLU TERS ÇEVİRME SÜRELİ ATARDAMAR FIRIL ETİKETLEME MRG'Sİ

Atardamar fırıl etiketleme manyetik rezonans görüntüleme (ASL MRG), herhangi bir kontrast maddesi veya radyasyon kullanmadan beyin kan akışını (SKA) nicel olarak ölçer. Dokuya ve arteriyel damarlara etiketlenmiş kan varış süresinin hesaplanması, nörodejeneratif bozuklukların anlaşılmasında faydalı olabilecek hemodinamik bilgiler sağlar. Bu nedenle, zaman alan ve ortalama sayısını sınırlayan varış sürelerindeki belirsizliklerden kaynaklanan hatalı SKA'yı önlemek için birkaç farklı görüntüleme zamanında ayrı pCASL yapılabilir. Birden çok ters T1larda ASL veri toplamak için Look-Locker (LL) okumasının kullanımına dayanan ASL MR ve Hadamard matrisini kullanan zaman kodlu sözde sürekli ASL MRI (te-pCASL) iki yaklaşımdır. LL okumalı ASL-MRI, SKA'yı doğru bir şekilde hesaplamak için karmaşık bir model gerektirir. Öte yandan, te-pCASL MRI, SKA hesaplamasında hatalara neden olabilecek bir parlama etkisine sahiptir. Bu tezin ilk bölümünde, hafif bilişsel bozukluğu olan Parkinson Hastalığında (PH) beyin perfüzyon eksiklikleri, LL okumalı ASL MRG kullanılarak araştırılmıştır. Hafif bilişsel bozukluğu olan PH'nin sağlıklı kontrole kıyasla %90'ın üzerinde doğrulukla posterior hipoperfüzyon göstermiştir. Ayrıca, mikrotübül ilişkili protein tau geni (MAPT) H1/H1 haplotipine sahip genetik olarak riskli PD, riskli olmayan PD'ye göre görsel hipoperfüzyona sahiptir. Tezin ikinci bölümünde, te-pCASL MRG'de parlama etkisinin olası nedenleri simülasyonlar ve in-vivo veriler kullanılarak değerlendirilmiştir. Teorik modele dayalı olarak, pCASL ve te-pCASL MRI, aynı ASL sinyalleriyle sonuçlandı. Öte yandan, deneysel sonuçlarımız, seçmeli arka plan bastırma çevirme darbelerinin kullanımının, parlama etkisinin ortaya çıkmasına yol açabileceğini gösterdi.

**Anahtar Sözcükler:** Atardamar fırıl etiketleme, Parkinson hastalığı, hafif kognitif bozukluk, te-pCASL, Look-Locker okuması, parlama etkisi

## TABLE OF CONTENTS

ACKNOWLEDGEMENTS . . . . .	iii
ACADEMIC ETHICS AND INTEGRITY STATEMENT . . . . .	iv
ABSTRACT . . . . .	v
ÖZET . . . . .	vi
LIST OF FIGURES . . . . .	ix
LIST OF TABLES . . . . .	xii
LIST OF SYMBOLS . . . . .	xiii
LIST OF ABBREVIATIONS . . . . .	xiv
1. INTRODUCTION . . . . .	1
2. BACKGROUND . . . . .	4
2.1 Circle of Willis . . . . .	4
2.2 Cerebral Blood Flow . . . . .	5
2.3 Regulation of Cerebral Blood Flow . . . . .	6
2.3.1 Cerebral Autoregulation . . . . .	6
2.3.2 Neurovascular Coupling . . . . .	7
2.4 Perfusion Measurement . . . . .	7
2.5 Arterial Spin Labelling MRI . . . . .	8
2.5.1 ASL MRI Techniques . . . . .	9
2.5.2 ASL MRI Models of Quantification . . . . .	10
2.5.3 Background Suppression in ASL MRI . . . . .	14
2.5.4 Multi Inversion Time ASL MRI . . . . .	17
2.5.4.1 Look-Locker Readout . . . . .	18
2.5.4.2 Time-Encoded pCASL MRI . . . . .	20
2.6 Perfusion Deficits in Parkinson’s Disease . . . . .	23
2.7 Aim . . . . .	25
3. MATERIALS and METHODS . . . . .	27
3.1 ASL MRI with LL readout data . . . . .	27
3.2 te-pCASL MRI data . . . . .	40
4. RESULTS . . . . .	51

4.1	ASL MRI with LL readout data . . . . .	51
4.1.1	Comparison of Subjects' NPT scores . . . . .	51
4.1.2	Voxel-Based Comparison of Subject Groups . . . . .	53
4.1.3	Comparison of Subjects Groups with Different genotypes . . . . .	57
4.1.4	Comparison of Subjects Groups in General cognitive, executive, and visual domains . . . . .	59
4.2	te-pCASL MRI data . . . . .	61
4.2.1	Simulation . . . . .	61
4.2.2	Comparison of te-pCASL and traditional pCASL datasets . . . . .	64
4.2.3	Shine-through effect . . . . .	67
5.	DISCUSSION . . . . .	72
6.	CONCLUSION . . . . .	79
7.	APPENDIX A: Publications . . . . .	80
	REFERENCES . . . . .	88

## LIST OF FIGURES

Figure 2.1	The structure of Circle of Willis.	5
Figure 2.2	Background suppression scheme and changes in longitudinal magnetization for three tissue types with different relaxation times over time.	15
Figure 2.3	The schemes of the control (a) and label (b) sequences with interleaved BGS and Hadamard sequence with (c) and without (d) interleaved BGS.	17
Figure 2.4	the Look-Locker readout pulses in ASL sequence, changes in the longitudinal magnetization with low flip-angle excitation pulses and perfusion-weighted images over time.	19
Figure 2.5	The schematic of the pCASL control (a), label (b) sequences and te-pCASL with Hadamard-8 sequence (c).	21
Figure 2.6	The schematic of the pCASL control (a), label (b) sequences and te-pCASL with Hadamard-8 sequence (c).	22
Figure 3.1	The demonstration of six slices at different eight TIs.	31
Figure 3.2	ASL images of different slices were realigned at each TI for each repeat.	32
Figure 3.3	The creation of difference images by subtracting the mean realigned control and label images.	33
Figure 3.4	The changes of longitudinal magnetization of control images during LL readout.	34
Figure 3.5	M0 curve fit for one example pixel.	36
Figure 3.6	Masking of a mean control image (a) using 0.3 (b), 0.5 (c) and 0.7 (d) intensity thresholds, respectively.	36
Figure 3.7	Registered T <sub>1</sub> w image (b) and CBF map (c) of one example HC subject onto MNI152 brain atlas (a).	37
Figure 3.8	The overlay of standard probability map of GM in SPM (grey) and the GM mask created for subject population (yellow).	38
Figure 3.9	The schematic model of the ASL MRI technique.	41

Figure 3.10	Generated arterial vessels, GM and WM maps.	44
Figure 3.11	Generated ATT and TTT maps.	44
Figure 3.12	The scheme of Hadamard-8 matrix that was applied in this study.	45
Figure 3.13	The scheme of te-pCASL for Hadamard size 4.	46
Figure 3.14	The GUI of te-pCASL.	47
Figure 3.15	The schematic of the MRI experiments performed at LUMC.	49
Figure 3.16	The GM and vessels masks of the volunteer.	50
Figure 4.1	$M_0$ (a), CBF (b), aBV (c), and ATT (d) maps for a healthy control subject.	54
Figure 4.2	The areas showing statistically significant differences of CBF between HC, PD-CN, and PD-MCI observed with ANOVA and post hoc comparisons. The color bars represent peak F value in the ANOVA and t values in the pair-wise comparisons. R: Right, L: Left.	55
Figure 4.3	The areas showing significantly lower CBF in MAPT H1/H1 haplotype compared to H1/H2 haplotype, including the all-PD or the PD-MCI patients, respectively. The color bars represent t values. R: Right, L: Left.	59
Figure 4.4	Regions of significant CBF decreases of LP compared to HP in all of the participants according to general cognitive and executive domain scores. The color bars represent t values. R: Right, L: Left.	61
Figure 4.5	The changes of longitudinal magnetization of control protons, first and last labeled protons versus time.	62
Figure 4.6	The curves of ASL signal of general kinetic model and two compartment model versus time.	62
Figure 4.7	The perfusion-weighted images of pCASL (a), encoded (b) and perfusion-weighted (c) images of te-pCASL.	63
Figure 4.8	Subtraction of perfusion-weighted images of simulated pCASL and te-pCASL MRI.	63
Figure 4.9	The SNR images of simulated pCASL and te-pCASL MRI.	63

Figure 4.10	Perfusion-weighted images of te-pCASL (a) and pCASL (b) and tStdv images of te-pCASL (c) and pCASL (d) from first single scan session.	64
Figure 4.11	Box-plot showing mean tStdv of vessels (a) and GM (b) values of pCASL and te-pCASL images.	65
Figure 4.12	Perfusion-weighted images of te-pCASL (a) and pCASL (b) and tStdv images of te-pCASL (c) and pCASL (d) from second single scan session.	65
Figure 4.13	Box-plot showing mean tStdv of vessels (a) and GM (b) values of pCASL and te-pCASL images.	66
Figure 4.14	The Bland-Altman test results for the differences of the mean tStdv values of pCASL and te-pCASL in GM and vessels regions acquired from first (a, b) and second (c, d) scan sessions.	67
Figure 4.15	Perfusion-weighted images of fully acquired te-pCASL images.	68
Figure 4.16	tStdv images of fully acquired te-pCASL dataset.	68
Figure 4.17	Perfusion-weighted images of fully acquired te-pCASL and seven separate te-pCASL experiments for one slice.	69
Figure 4.18	Perfusion-weighted images of te-pCASL with RF at only sub-boli 3 with either selective BGS (a) or global BGS (b) and of interleaved te-pCASL with RF at only sub-boli 3 with selective BGS (c).	70
Figure 4.19	Perfusion-weighted (a) and tStdv images (b) of te-pCASL without any labeling RF pulses with either selective or global BGS for one slice.	71

## LIST OF TABLES

Table 3.1	Demographics of subjects.	28
Table 4.1	Comparison of neuropsychological test scores and the P values calculated by a Kruskal-Wallis test followed by post-hoc Dunn-Sidak tests.	52
Table 4.2	Comparisons of neuropsychological test scores between two genetic groups according to MAPT haplotypes within the all-PD group and the PD-MCI group, and the P values calculated by a Mann-Whitney U test.	53
Table 4.3	The regions of CBF differences between groups detected by one-way ANOVA, with cluster forming $P < 0.005$ , cluster level FWE corrected threshold at $P < 0.05$ , and cluster size of 50 voxels.	56
Table 4.4	The regions of CBF differences between two groups within all-PD and PD-MCI groups according to MAPT haplotypes at cluster-forming $P < 0.005$ , cluster-level FWE-corrected threshold of $P < 0.05$ , and cluster size of 50 voxels.	58
Table 4.5	Regions of CBF differences between two groups defined based on composite z-scores in general cognitive domain and executive domain within the entire subject group, separately.	60

## LIST OF SYMBOLS

$h(\tau)$	Transport function of tracers
$f$	Brain Blood flow
$T_1$	Longitudinal relaxation time
$\lambda$	Blood partition coefficient of water
$T_{1blood}$	Longitudinal relaxation time of the arterial blood
$T_{1tissue}$	Longitudinal relaxation time of the tissue
$\alpha$	Labeling efficiency
$\Delta TI$	Time between the RF pulses
$M_z$	Longitudinal magnetization
$M_{label}$	Longitudinal magnetization per ml of arterial blood
$M_0$	Magnetization under fully relaxed condition
$M_z$	Longitudinal magnetization per gram of venous
$\Delta$	Arrival time
$\Delta ta$	Arterial arrival time
$\tau$	Labeling duration
$\tau_a$	Bolus duration (seconds) of the arterial bolus
$q_0$	Quantity of labeled blood in beginning
$aBV$	Arterial blood volume fraction
$\Delta TI$	Time between the application of excitation RF pulses
$\Delta M_{art}$	Signal of intravascular component
$\Delta M_{tiss}$	Signal of tissue compartment
$\Delta M$	Total signal of the perfusion-weighted image
$\alpha$	Flip angle
$R(t)$	Residue function
$TI$	Inversion time
$q$	Correction factor
$q(t)$	Total amount of remaining tagged blood in brain

## LIST OF ABBREVIATIONS

aBV	Arterial Blood Volume
ACE-R	Addenbrooke's Cognitive Examination Revised
AD	Alzheimer's Disease
AG	Angular Gyrus
ASL	Arterial Spin Labeling
ATT	Arterial Transit Time
BA	Broadman Area
BGS	Background Suppression
CA	Cerebral Autoregulation
CASL	Continuous Arterial Spin Labeling
CBF	Cerebral Blood Flow
CO <sub>2</sub>	Carbon Dioxide
CoW	Circle of Willis
CPP	Cerebral Perfusion Pressure
CVR	Cerebrovascular Resistance
DAN	Dorsal Attention Network
DMN	Default-Mode Network
DTI	Diffusion Tensor Imaging
EPI	Echo Planar Imaging
FAIR	Flow Sensitive Alternating Inversion Recovery
FOV	Field Of View
FPN	Frontoparietal Network
FSL	FMRIB Software Library
GM	Gray Matter
GRAPPA	Generalized Auto Calibrating Partially Parallel Acquisition
GUI	Graphical User Interface
HC	Healthy Control
HP	High Performers

IV	Intravascular
LL	Look-Locker
ICP	Intracranial Pressure
ICNs	Intrinsic Connectivity Networks
IPL	Inferior Parietal Lobule
ITS-FAIR	Inflow Turbo Sampling Flow Sensitive Alternating Inversion Recovery
JLO	Benton Judgment of Line Orientation Test
kNN	k-Nearest Neighbor
LE	Labeling Efficiency
LL	Look-Locker
LP	Low Performers
MAP	Mean Arterial Pressure
MAPT	Microtubule-Associated Protein Tau Gene
MMSE	Mini-Mental State Examination
MNI	Montreal Neurological Institute
MOCA	Montreal Cognitive Assessment
MR	Magnetic Resonance
MRI	Magnetic Resonance Imaging
MT	Magnetization Transfer
NPT	Neurophysiological Test
O <sub>2</sub>	Oxygen
PASL	Continuous Arterial Spin Labeling
PCASL	Pseudo Continuous Arterial Spin Labeling
PD	Parkinson's Disease
PD-CN	Parkinson's Disease with Cognitively Normal
PDD	Parkinson's Disease with Dementia
PD-MCI	Parkinson's Disease with Mild Cognitive Impairment
PET	Positron Emission Tomography
PPC	Posterior Parietal Cortex
RF	Radio Frequency
ROI	Region of Interest

rs-fMRI	Resting-State Functional Magnetic Resonance Imaging
SAR	Specific Absorption Rate
SDMT	Symbol Digit Modalities
SENSE	Sensitivity Encoding
SMOTE	Synthetic Minority Class Over-Sampling
SNR	Signal to Noise Ratio
SPECT	Single Photon Emission Computerized Tomography
SPL	Superior Parietal Lobule
SPM	Statistical Parameter Mapping
STAR	Signal Targeting with Alternating Radiofrequency
SENSE	Sensitivity Encoding
stdv	Standard Deviation
SVM	Support Vector Machine
$T_1w$	$T_1$ -weighted
TE	Echo Time
te-pCASL	Time Encoded Arterial Spin Labeling
TI	Inversion Time
TE	Echo Time
TR	Repetition Time
tStdv	Temporal Standard Deviation
TTT	Tissue Transit Time
VN	Visual Network
VSM	Vascular Smooth Muscle
UPDRS	Unified Parkinson Disease Rating Scale
WCST	Wisconsin Card Sorting Test
WM	White Matter

## 1. INTRODUCTION

The Circle of Willis (CoW) is an important anatomical structure providing the collateral pathway for the distribution of and keeping cerebral blood flow (CBF) through brain [1]. CBF is a measurable parameter showing the blood volume passing per unit mass per unit time in brain tissue. CBF is regulated by the mechanisms to maintain the required substrates (glucose and oxygen) to brain and to remove carbon dioxide (CO<sub>2</sub>) and metabolic waste products from the brain [2]. Because CBF provides information about neural metabolism, it is considered as a prospective biomarker to detect and track neurological changes, in especially neurodegenerative diseases, such as Parkinson's disease (PD). Mild cognitive impairment (MCI), which represents a state between cognitively normal condition and dementia, is a symptom of progressive neurodegenerative diseases. PD with MCI (PD-MCI) is currently diagnosed based on an arbitrarily predefined standard deviation (stdv) of neuropsychological test scores, and more objective biomarkers for PD-MCI diagnosis are needed [3]. Although the detection of abnormal patterns in cerebral perfusion could be an anticipated biomarker, the measurement of it can be invasive when techniques, such as positron emission tomography (PET), and single-photon emission computed tomography (SPECT), are used due to their use of contrast agents and radiation emission [4, 5].

Arterial spin labeling magnetic resonance imaging (ASL MRI) is a non-invasive MRI technique to measure CBF quantitatively [6]. This technique is based on the subtraction of images containing either inflow inverted or non-inverted spins of the protons within the blood in brain. Firstly, the spins of the protons within inflow blood are inverted by applying 1800 RF pulses in the neck area. After a time called as inversion time (TI), label image is acquired. This experiment is repeated without applying any RF pulse to acquire control images. The perfusion-weighted images are generated by subtracting these two images, which are then fit into a model to calculate CBF [6–8]. Several techniques for ASL-MRI have been developed, which include continuous ASL (CASL) MRI, pulsed ASL (PASL) MRI and pseudo continuous ASL (pCASL) MRI.

pCASL MRI technique is of choice in the clinics, which combines CASL MRI's high SNR and PASL MRI's higher labeling efficiency [9]. Unlike PET and SPECT, ASL MRI is non-invasive and doesn't use any contrast agents or radiation. Despite these advantages, it is known that ASL MRI suffers mainly from low signal-to-noise (SNR) when compared to other methods measuring CBF, which might adversely affect the quantification of CBF [10]. A background suppression (BGS) scheme consisting saturation and inversion pulses has been proposed to optimize the SNR in ASL MRI [11]. However, the routine application of ASL has been somewhat limited due to the low SNR, which necessitates long acquisition time. Moreover, the uncertainty of transit time remains an unsolved problem [12]. Therefore, the signal of ASL MRI has been sampled at different TIs, which gives more precise information for estimating CBF maps.

Instead of performing separate traditional pCASL-MRI experiments, two techniques, which are ASL MRI with Look-Locker (LL) readout [8] and time encoded pCASL (te-pCASL) MRI [13], have been developed to enable the acquisition of ASL-MRI signals at different TIs within one scan. In ASL MRI with LL readout, the images are acquired by applying low flip angle radio frequency (RF) pulses at multiple times. On the other hand, te-pCASL MRI acquires the images by dividing the long labeling duration into a Hadamard size number,  $N$ , and changing the situation (label or control) in accordance with the sign of Hadamard matrix order. Perfusion-weighted images with certain TI and label duration are then reconstructed by adding or subtracting the acquired images considering the sign of Hadamard matrix order.

Multi-TI ASL MRI with LL readout requires fitting data into a complex model to produce accurate CBF maps, but enables estimation of CBF by taking into account the arrival time of labeled blood. On the other hand, te-pCASL MRI has been proposed as a technique to solve long acquisition time problem and to better estimate CBF map with high SNR within a single scan by using a Hadamard matrix. However, signal fluctuations causing the errors in CBF maps are seen in te-pCASL images, which is called as shine-through effect [14, 15]. There are theoretically prospective reasons causing the shine-through effect. These mechanisms could involve high vascular signal

or noise at short sub-boli/TIs, the switching between control and label situations in the consecutive sub-boli, the imperfect interleaving of control and label sub-boli, and the effect of BGS.

The aims of this thesis study were twofold. First, an in-house program was developed for estimating CBF maps out of ASL-MRI with LL readout data by combining general kinetic model and arterial blood volume correction. Then, this program was used to define perfusion deficits related to cognitive decline in PD including patients with risky gene carriers. Next, a study was conducted to understand the possible mechanisms behind the shine-through effect in te-pCASL MRI using simulations and in-vivo data.

## 2. BACKGROUND

### 2.1 Circle of Willis

The brain receives blood from a network of arteries. The junction of these arteries forms the CoW structure at the base of the brain [1, 16]. The CoW consists of ring-like vessels connecting the anterior and posterior circulations of the brain (Figure 2.1). This ring-like vessel includes three cerebral arteries, including paired internal carotid, paired posterior and paired anterior cerebral arteries, and two communicating areas, including posterior and anterior communicating arteries.

Blood is delivered to the brain through the paired internal carotid arteries and the paired vertebral arteries. Paired internal carotid cerebral arteries supply the blood from the neck into the brain and then branches into the paired anterior cerebral arteries which provide the anterior circulation supplying the blood to the majority of the cerebral hemispheres, including the frontal lobes, parietal lobes, lateral temporal lobes and anterior part of deep cerebral hemispheres. The paired vertebral arteries form the basilar artery that divides into paired posterior cerebral arteries which enable the posterior circulation by supplying the blood to the brainstem, cerebellum, occipital lobes, medial temporal lobes and posterior part of the deep hemisphere, mainly the thalamus. The CoW structure is completed by two communicating arteries, including posterior and anterior communicating arteries.

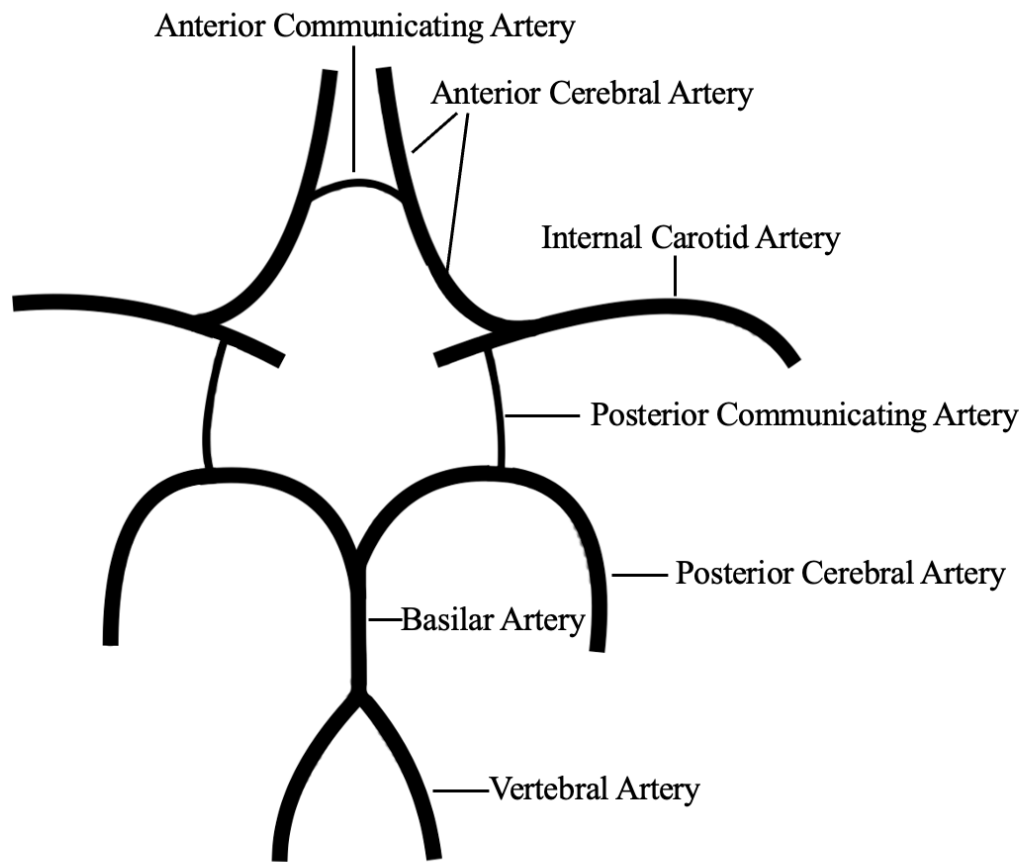


**Figure 2.1** The structure of Circle of Willis.

## 2.2 Cerebral Blood Flow

CBF indicates how much blood passes through the tissue in units of milliliters of blood per 100 g of brain tissue per minute (ml/100g/min). In the literature, it has been reported that the CBF values range from 40 to 100 ml/100 g of tissue/min in gray matter (GM) [5,10]. The measurement of CBF is important for the assessment of tissue viability and function, because CBF has a correlation with neuronal metabolism [15].

## 2.3 Regulation of Cerebral Blood Flow

Even though the brain is only 2-3% of the total body weight, it requires approximately 15% of the body's total cardiac output and approximately 20% of the body's total oxygen consumption at rest [2]. Unlike the other organs having a large store of glycogen, the brain lacks fuel stores of glucose and oxygen [2]. Therefore, the brain needs to be constantly supplied with oxygen and energy so as to maintain adequate perfusion. The regulation of CBF is essential to deliver the necessary substrates (glucose and oxygen) to the brain and to remove carbon dioxide (CO<sub>2</sub>) and metabolic waste products from the brain [2]. There are two local control mechanisms, which are cerebral autoregulation and neurovascular coupling, for regulating and maintaining an adequate blood supply to the brain [17].

### 2.3.1 Cerebral Autoregulation

Cerebral autoregulation (CA) is a homeostatic process that maintains constant CBF despite changes in cerebral perfusion pressure (CPP) and activates the vascular smooth muscle (VSM) for the regulation of CBF. CBF is not only dependent on changes in CPP but also on the cerebrovascular resistance (CVR). CA is responsible for adjusting CVR to keep stable CBF. Additionally, CPP is the subtraction of mean arterial pressure (MAP) and intracranial pressure (ICP). The relationship between these variables is presented in Eq. 2.1 and Eq. 2.2.

$$CBF = \frac{CPP}{CVR}, \quad (2.1)$$

$$CPP = MAP - ICP. \quad (2.2)$$

When MAP or CPP increases, CVR will increase by means of vasoconstriction in order to maintain CBF values constant. Conversely, CVR will be decreased when MAP or CPP decreases. When the CA mechanism is absent, an increase in MAP

causes not only an increase in CPP but also in CBF even if there is no change in the metabolic demand of the brain. Two of the most dominant and known mechanisms for the CBF regulation are the myogenic and metabolic mechanisms of CBF.

Myogenic mechanism is the ability to increase or decrease the size of vessel lumen by VSM to keep the blood flow constant within the vessels. Metabolic mechanisms provide autoregulation in accordance with the metabolic response controlled by several factors, such as  $O_2$  and  $CO_2$  levels [18].

### **2.3.2 Neurovascular Coupling**

Neurovascular coupling is described as a link between neurons and their energy demand. Neuronal activity causes more oxygen consumption. Consequently, vascular dilation occurs, which causes an increase in blood volume and flow to supply  $O_2$  and nutrients to the brain and to remove waste [19]. This is an example of a feedforward mechanism, because CBF is regulated before the difference between demand and supply occurs.

## **2.4 Perfusion Measurement**

The idea behind perfusion measurement has been to follow a tracer through the vascular system and to measure brain perfusion by assessing the amount of tracer taken up by the tissue of interest. In 1945, Kety and Schmidt [20] developed a method, based on Fick's idea [21], to measure CBF using inhaled, highly diffusible, and inert nitrous oxide as a tracer. The amount of gas taken up by the brain per unit time was equal to the difference of the gas brought to the brain by the arterial blood and gas carried away by the venous blood, which provided a simple calculation of global CBF. In 1954, the "indicator-dilution" theory was introduced as a model describing the passage of a tracer through the brain [22]. The tracer particles can take different paths, whereas the amount of these particles decreases in time. Levels outflow,  $h(\tau)$ , was defined as

the amount of tracer leaving the brain over time [23], which could be represented as,

$$\int_0^{\infty} h(\tau) d\tau = 1. \quad (2.3)$$

There have been several imaging techniques to measure CBF. Most commonly employed technologies are PET and SPECT, which both inject a tracer into the vasculature, and monitor its accumulation. The concentration of the tracer is measured using a suitable detector while the tracer accumulates in the brain. Although both of these techniques could provide accurate quantitative regional CBF measurements with excellent reproducibility, they have drawbacks such as limited spatial resolution, the usage of a contrast agent, long acquisition time and radiation exposure [4, 5]. MRI is another technique that could measure CBF non-invasively. One of the perfusion MRI techniques is dynamic susceptibility contrast magnetic resonance imaging (DSC MRI) that tracks the first passage of an exogenous, paramagnetic, non-diffusible contrast agent, such as gadolinium, through the tissue of interest [24]. This technique has some drawbacks, such as cost, limited availability, and some patient discomfort. Another technique to quantify CBF is ASL MRI [9]. Compared to SPECT and PET, ASL MRI is a non-invasive perfusion MRI modality and has several advantages, including lower cost, and shorter preparation and scan times [9, 25].

## 2.5 Arterial Spin Labelling MRI

ASL MRI measures CBF non-invasively without the use of either radioactive or gadolinium-based tracers. This technique has some advantages with respect to other techniques measuring perfusion. First, it can be repeated at multiple times to track relative changes of CBF over time [6]. Also, CBF maps calculated from ASL MRI have high spatial resolution [26]. Besides these advantages, ASL MRI suffers from poor SNR. The principle of ASL MRI is based on the tracer tracking approach. The longitudinal magnetization of protons within the inflow blood are inverted by applying a 180° pulse in the labeling region. Inverted protons travel to the brain through the arterial

vessels and are considered as magnetic tracers. After a delay time, which is called inversion time (TI), label images are acquired of the imaging volume. This experiment is repeated without magnetically labeling protons to create control images, where the longitudinal magnetization of protons is fully relaxed. The subtraction of the control and the label images eliminates static tissue signal. The remaining signal generates a perfusion-weighted image, which indicates the amount of the labeled protons that accumulated within the tissue during the delay time [6].

### 2.5.1 ASL MRI Techniques

ASL MRI techniques are classified into three main groups, which are CASL, PASL, and pCASL, based on their labeling schemes. CASL was proposed by Williams et al. in 1992 [6]. In CASL, long and continuous RF pulses with a gradient in the slice-selection direction are used in order to invert protons within the blood. Although CASL provides a high SNR, it suffers from magnetization transfer (MT) effects because of the long RF pulse, which causes partial saturation of macromolecule magnetization and thus errors in CBF calculations. Additionally, long inversion RF pulses causes large RF energy deposition and thus a high specific absorption rate (SAR) [9].

Another type of ASL MRI is PASL, which uses short, slab-selective RF pulses. In this approach, protons within the blood are inverted by short RF pulses in a specific area called the labeling region. Importantly, there is a need for a spatial gap between the distal edge of the labeling and imaging volumes due to the imperfect edges of the inversion pulses. For PASL, MT effects and SAR are less of an issue for CASL. Moreover, PASL has the advantage of a high labeling efficiency [9].

Garcia et al. [27] developed pCASL, which uses a train of RF pulses in conjunction with suitable gradients. It combines CASL's high SNR and PASL's higher tagging efficiency. This technique provides higher SNR than PASL and is easier implemented for clinical RF amplifiers than CASL. pCASL compensates for the MT effects and provides less RF power deposition than CASL [9].

### 2.5.2 ASL MRI Models of Quantification

There have been several techniques developed to quantify cerebral perfusion acquired by ASL MRI. The general idea behind the quantification of the CBF is based on the subtraction of the label and control images to produce perfusion-weighted images to remove the static tissue in the brain. Following that, a CBF map is generated by calibrating perfusion-weighted images based on a signal model and an estimation of  $M_0$ , i.e., the MR-signal of a voxel filled with fully relaxed blood.

#### *Single Compartment Model*

One of the CBF estimation models is single compartment model based on the modified Bloch equations. In this approach, the Bloch equations were modified to include single-compartment kinetics to produce an analytical formula for the longitudinal magnetization changes of the total magnetization of static tissue and inflowing labeled blood [6, 28]. This model assumes a well-mixed compartment between the microvasculature and tissue, and sets the magnetization of the venous blood relative to the magnetization of the labeled blood within the tissue. This approach assumes that the inflowing labeled protons are instantaneously exchanged with the tissue upon their arrival. Labeled blood enters the tissue voxel with the longitudinal magnetization,  $M_{label}(t)$ , and leaves with longitudinal magnetization of venous blood, which is equal to the average longitudinal magnetization,  $M(t)$ , weighted by the equilibrium ratio of water in brain compared to the blood partition coefficient,  $\lambda$ .

This first approach could be represented as;

$$\frac{dM(t)}{dt} = \frac{M_0 - M(t)}{T_1} + fM_{label}(t) - f\frac{M(t)}{\lambda}, \quad (2.4)$$

where  $M_0$  is the main magnetization of the blood under fully relaxed conditions, and  $T_1$  is longitudinal relaxation time of the magnetization in the absence of flow or exchange between blood and brain.  $fM_{label}(t)$  and  $f\frac{M(t)}{\lambda}$  are the magnetization of labeled protons entering and leaving the brain, respectively.

In the control experiment, no inversion pulses are applied in the labeling region which means that  $M_{label}(t)=M_{label}^0(t)$ . Therefore, the solution of Bloch equation is described over time as following,

$$\begin{aligned} M_{ctrl}(t) &= M_0(1 - e^{-\frac{t}{T_{1app}}}), \\ \frac{1}{T_{1app}} &= \frac{1}{T_1} + \frac{f}{\lambda}. \end{aligned} \quad (2.5)$$

In the label experiment, an inversion pulse is applied in the labeling region. So, the magnetization changes could be expressed as,

$$M_{label}^t = M_{label}^0(1 - 2\alpha e^{-\frac{t}{T_{1blood}}}), \quad (2.6)$$

where  $T_{1blood}$  is longitudinal relaxation time of the arterial blood and  $\alpha$  is labeling efficiency defined as,

$$\alpha = \frac{M_{label}^0 - M_{label}(t=0)}{2M_{label}^0}. \quad (2.7)$$

Under above conditions, Bloch equation could be solved as,

$$M_{label}(t) = M_0(1 - e^{-\frac{t}{T_{1app}}}) - 2\alpha M_0 \frac{f (e^{-\frac{t}{T_{1app}}} - e^{-\frac{t}{T_{1blood}}})}{\lambda (\frac{1}{T_{1a}} - \frac{1}{T_{1app}})} \quad (2.8)$$

The magnetization difference of the control and label experiments is thus equal to,

$$\Delta M(t) = M_{control}(t) - M_{label}(t) = 2\alpha M_0 \frac{f (e^{-\frac{t}{T_{1app}}} - e^{-\frac{t}{T_{1blood}}})}{\lambda (\frac{1}{T_{1a}} - \frac{1}{T_{1app}})}. \quad (2.9)$$

### ***General Kinetic Model***

This approach is based on the modeling of a "bolus" of labeled spins traveling through the vasculature. Buxton formulated the calculation of CBF as a convolution problem without starting from the Bloch equations [7]. In the general kinetic model, the transit delay and bolus duration are taken into account and tracer kinetic theory is used. The dynamic tissue concentration of any tracer delivered to the tissue by

blood flow is described mathematically in this theory. Labeled protons are considered as tracers in blood, and three functions are described within the general kinetic model. The function "arterial input function (AIF)" defines the delivery of the tracer, in which the labeled protons are modelled as a radioactive agent with the "half-life time of protons" dependent on the longitudinal relaxation time of blood,  $T_{1b}$ . The arterial concentration  $c(t)$  of the protons arriving at time  $t$  in the brain could be modelled as,

$$c(t) = \begin{cases} 0, & 0 < t < \Delta t \\ e^{\frac{-t}{T_{1blood}}} (Pulsed\ labeling), & \Delta t < t < \Delta t + \tau \\ e^{\frac{-\Delta t}{T_{1blood}}} (Continuous\ labeling), & \Delta t < t < \Delta t + \tau \\ 0. & 0 < t < \Delta t \end{cases} \quad (2.10)$$

where  $\Delta t$  is the arrival time of the labeled blood, i.e. the time it takes the blood to travel of the labeling region to the imaging volume. Therefore, *AIF* can be described as the following equation,

$$AIF = (M_{label}^0 - M_{label}(t = 0))c(t) = 2M_0\alpha c(t). \quad (2.11)$$

The second function is the residue function ( $r$ ), which reflects the fraction of labeled protons that still remain within the brain at a time  $t$  after their arrival. Total amount of remaining labeled protons in image voxel is described as,

$$q(t) = q_0 - q_0 H(t), \quad (2.12)$$

where,  $q_0$  is the quantity of labeled blood in the beginning, and  $q_0 H(t)$  is the total amount of tracer leaving the brain slice. So,  $r$  is described as [23],

$$r(t) = 1 - H(t) = \frac{q(t)}{q(0)} = e^{\frac{-ft}{\lambda}}, \quad (2.13)$$

The relaxation function is the third and the last function that incorporates the loss of labeled protons due to longitudinal relaxation time, which is denoted as,

$$m(t) = e^{\frac{-t}{T_1}}, \quad (2.14)$$

Putting everything together, Buxton describes the time dependent tissue signal as [7],

$$\Delta M(t) = f \int_0^t AIF(\tau)r(t-\tau)m(t-\tau)d\tau, \quad (2.15)$$

where  $\lambda$  is the labeling duration. As a result,  $\Delta M_{tissue}(t)$  can be modelled as,

$$\Delta M_{tissue}(t) = \begin{cases} 0, & 0 < t < \Delta t \\ 2M_0 f(t-\Delta t)\alpha e^{\frac{-t}{T_{1blood}}} q_p(t) (Pulsed\ labeling), & \Delta t < t < \Delta t + \tau \\ 2M_0 f\tau\alpha e^{\frac{-t}{T_{1blood}}} q_p(t) (Pulsed\ labeling), & \Delta t + \tau < t \end{cases} \quad (2.16)$$

and,

$$\begin{aligned} q_p(t) &= \frac{e^{kt}(e^{-k\Delta t} - e^{-kt})}{k(t-\Delta t)}, & \Delta t < \Delta t + \tau \\ q_p(t) &= \frac{e^{kt}(e^{-k\Delta t} - e^{-kt})}{k\tau}, & \Delta t < \Delta t + \tau \\ k &= \frac{1}{T_{1blood}} - \frac{1}{T_1}, \\ \frac{1}{T_1'} &= \frac{1}{T_{1tissue}} + \frac{f}{\lambda}. \end{aligned} \quad (2.17)$$

where  $T_{1tissue}$  is the tissue blood spin-lattice relaxation constant.

### ***Inflow Turbo Sampling FAIR (ITS-FAIR)***

Gunther et al. modified the general kinetic model to describe the signal obtained with FAIR labeling, which is a PASL type of ASL, in combination with a LL readout [8]. In the general kinetic model, 90° readout RF pulses are assumed to measure the signal. However, in ITS-FAIR, a LL readout is applied consisting of a train of small flip-angle readouts. So, signal is multiplied with sine of the flip angle, which is formulated as,

$$\Delta M(t) = M_z(t) \sin \alpha \quad (2.18)$$

The use of a train of readout pulses will decrease the label detected for later timepoints, the effectively decreasing longitudinal relaxation time equals to,

$$T_{1eff} = \frac{1}{\frac{1}{T_1} - \frac{\log(\cos\alpha)}{\Delta TI}} \quad (2.19)$$

where,  $\alpha$  is the readout flip angle and  $\Delta TI$  is the time between the application of excitation RF pulses. The general kinetic model can be modified to include the flip angle effect. Quantitative CBF can then be estimated using Eq. 2.20 based on the inflow turbo-sampling EPI-FAIR method, which is a variant of pulsed ASL with LL technique [8]. The difference magnetization is,

$$\Delta M_{tissue}(t) = \begin{cases} 0, & 0 < t \leq \Delta t \\ -2M_0 f \sin \alpha \frac{e^{\frac{-t}{T_{1blood}}} (1 - e^{\delta R_{ITS-FAIR}(t-\Delta t)})}{\delta R_{ITS-FAIR}}, & \Delta t < t \leq \Delta t + \tau \\ -2M_0 f \sin \alpha \frac{e^{\frac{-(\Delta t + \tau)}{T_{1blood}}} (1 - e^{\delta R_{ITS-FAIR}(\tau)}) e^{-R_{1app}(t-\Delta t-\tau)}}{\delta R_{ITS-FAIR}}, & \Delta t + \tau < t \end{cases} \quad (2.20)$$

and,

$$\delta R_{ITS-FAIR} = \frac{1}{T_{1blood}} - \left( \frac{1}{T_{1tissue}} + \frac{1}{\lambda} - \frac{\ln(\cos \alpha)}{\Delta TI} \right) = \frac{1}{T_{1blood}} - R_{1app} \quad (2.21)$$

### 2.5.3 Background Suppression in ASL MRI

The subtraction of control and label images could not fully cancel out the background signal coming from static tissue due to the physiological noise and motion artifacts. In 1991, Dixon introduced the BGS technique initially to eliminate static tissue signal by multiple inversion pulses for MRI angiography [11]. After that, BGS schemes with continuous labeling and pulsed labeling were applied in ASL [29,30]. One study compared the ASL performance with and without BGS on a pixel by pixel basis and found out that the standard deviation of the ASL signal measurement was lower for in ASL images with BGS [31]. In the BGS scheme, one saturation pulse and then several inversion pulses are applied at the imaging volume at certain time points before the readout [32]. The saturation pulse nulls the magnetization of all tissue types. As a result, the recovery of magnetization starts from zero. Then, the inversion pulse flips the direction of magnetization from positive to negative values. So, the recovery of magnetization starts from the negative. The rate of recovery is dependent on the  $T_1$  value of each tissue type. The readout is employed at a time when magnetization is about zero during the recovery of magnetization going from negative to positive. The suppression of the signal from multiple tissue types can be achieved by timing the

readout and inversion pulses based on the individual  $T_1$  values. Figure 2.2 shows an example of BGS scheme, consisting of one saturation pulse and two inversion pulses, and the magnetization changes of three tissue types with different  $T_1$  during the period from the application of saturation pulse to the start of the readout.

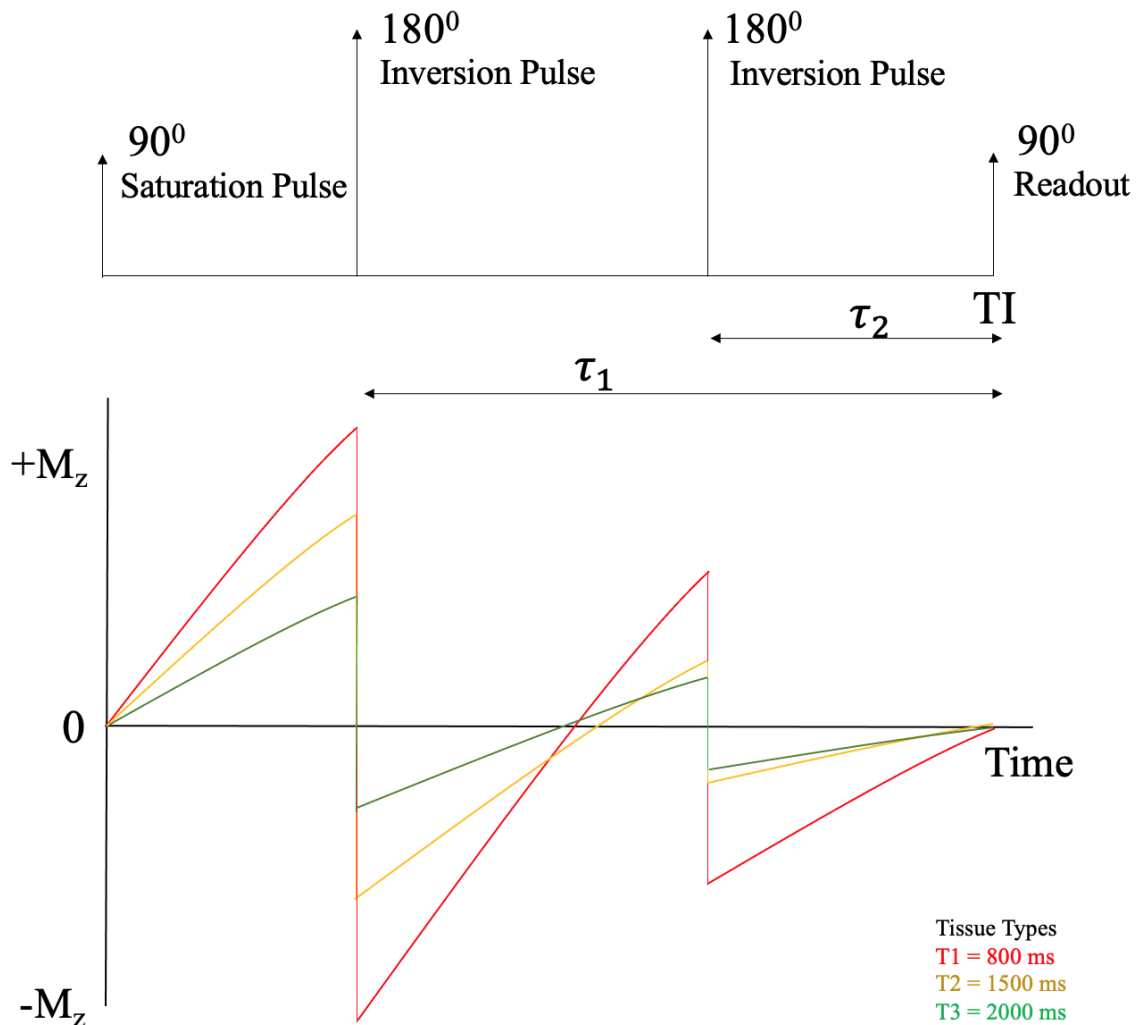


**Figure 2.2** Background suppression scheme and changes in longitudinal magnetization for three tissue types with different relaxation times over time.

Several studies about the implementation and optimization principles of BGS in ASL have been published [31, 33]. An initial saturation pulse is applied with slice-selective gradients in the imaging volume. Following the labeling inversion pulse, the inverted protons return back to equilibrium with relaxation time. The difference be-

tween inverted (label) and non-inverted spins (control) decays towards zero with the same time constant until readout. The direction of spins is changed by applying inversion BGS pulses, which has no impact on the difference value. At the application of readout, the ASL signal is protected, and the signal from static tissue is nearly eliminated.

In 2010, Dai et al. proposed the combination of long labeling duration and BGS to maximize the SNR, because long labeling duration leaves little options for the timing of the BGS pulses, resulting in ineffective of BGS pulses and lower SNR [34]. There are major difficulties associated with the implementation of BGS during labeling duration, one of which is the number of inversion pulses. It is necessary to limit the inversion pulses, because the ASL signal is decreased by the imperfect inversion efficiency of BGS pulses [31]. Secondly, all BGS must be slice-selective before and during labeling. Slice-selective saturation and inversion pulses of BGS are applied from the upper end of the labeling region to the upper end of the imaging volume. Additionally, the labeling condition must be switched to control or label and vice versa, because the magnetization direction of labeled blood that has left the labeling region is changed when the inversion BGS pulse is applied during a long labeling duration. Otherwise, the spins of inflowing blood that just enters the labeling region after the first inversion BGS pulse are first inverted by labeling RF pulses and then again by the second inversion BGS pulses. Consequently, the magnetization of these spins remains as like unlabeled. This scenario causes a mixture of the labeled and unlabeled blood and errors in the assessment of CBF. When inversion BGS pulses are applied during the labeling period, control and label situations have to be switched to ensure continuous labeled or unlabeled blood. These schemes are illustrated in Figure 2.3.

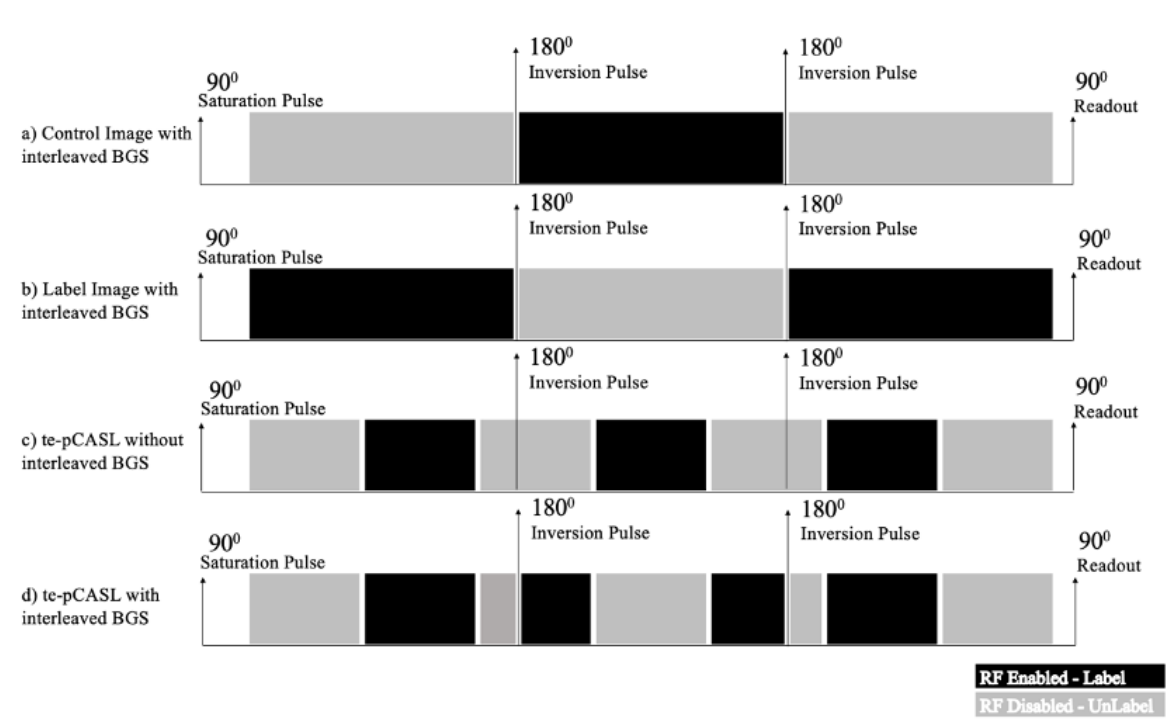


**Figure 2.3** The schemes of the control (a) and label (b) sequences with interleaved BGS and Hadamard sequence with (c) and without (d) interleaved BGS.

#### 2.5.4 Multi Inversion Time ASL MRI

pCASL has several advantages over other techniques. However, some problems can be seen in CBF maps of the pCASL MRI. One of them is uncertainty in labeling efficiency (LE) that is a measure of the inversion rate of flowing spins. LE, which is equal to  $(\text{arterial blood in the control scan} - \text{arterial blood in the label scan})/2$ , is assumed to be 0.85 in most studies [10]. The labeling mechanism of pCASL is not precisely an adiabatic inversion like CASL. As a result, B0 inhomogeneity, B1 inhomogeneity, and flow velocity may all affect labeling efficiency. It was reported that LE is an important parameter for achieving high SNR, as well as for minimization errors in CBF quantification [35]. The other problem of pCASL MRI is the uncertainty in longitudinal relaxation time of arterial blood, which affects the CBF calculation due to the time dependent decay of the signal [36]. In ASL MRI, the spins of the labeled protons will decay due to the longitudinal relaxation time after the magnetization has

been inverted. In the ASL consensus paper of 2015,  $T_1$  of blood was assumed to be the main determinant for the loss of labeled protons in the calculation of CBF maps [10]. However, the value would need to be changed in accordance with where the labeled protons are in the brain (white matter (WM), GM or blood) for more accurate CBF quantification. The other issue stems from the choice of TI, which is supposed to be long enough to ensure that all labeled protons within the blood have arrived to the tissue of interest. CBF estimates are affected by the uncertainties in the transit time of blood from the labeling site to the capillary bed of the brain area [12]. Inverted spins of labeled protons would return to their equilibrium state before reaching the tissue of interest when the arrival time of the labeled blood is too long in a subject with slow blood flow. On the other hand, setting the imaging time to match the arrival times could cause a significant reduction in SNR. Additionally, for the shorter TIs, i.e. shorter than the arrival time, labeled protons would still reside in the vascular compartment before imaging. Therefore, the choice of TI is important for acquiring ASL signal in a correct way to allow accurate quantification of blood flow. Separate pCASL scans can be done at several TIs in order to avoid inaccurate CBF resulting from uncertainties in arrival times, which is time-consuming and costly [37]. Additionally, the measurement of sufficient ASL signal is not possible in deep WM using pCASL with prolonged TI [38]. To compensate for such delays in blood transit without wasting time, some methods have been proposed for fast ASL acquisitions with multiple TIs. One of these techniques is based on the use of LL readout. The other technique is time-encoded pCASL MRI.

#### **2.5.4.1 Look-Locker Readout**

Look and Locker have proposed the LL readout in 1970. The aim of LL readout was to save scan time by producing a train of absorptions instead of waiting for equilibrium magnetization [39]. LL readout is one of the readouts for ASL MRI, that can speed up multi-TI acquisitions by acquiring multiple images with a range of TI times after a single labeling RF pulse is applied. In this readout, the recovery of longitudinal magnetization is perturbed by applying several excitation pulses with a low flip angle.

The application of LL in ASL MRI corresponds to the acquisition of multiple images after protons are inverted by the labeling RF pulse. The advantage of this technique is to acquire multiple images with higher temporal information in a single scan without increasing the scan time. However, this readout results in low SNR, due to the perturbations of longitudinal magnetization by multiple RF pulses [40]. Figure 2.4 shows the Look-Locker readout pulses in ASL sequence, changes in the longitudinal magnetization with low flip-angle excitation pulses and perfusion-weighted images corresponding at each low flip-angle excitation pulse.

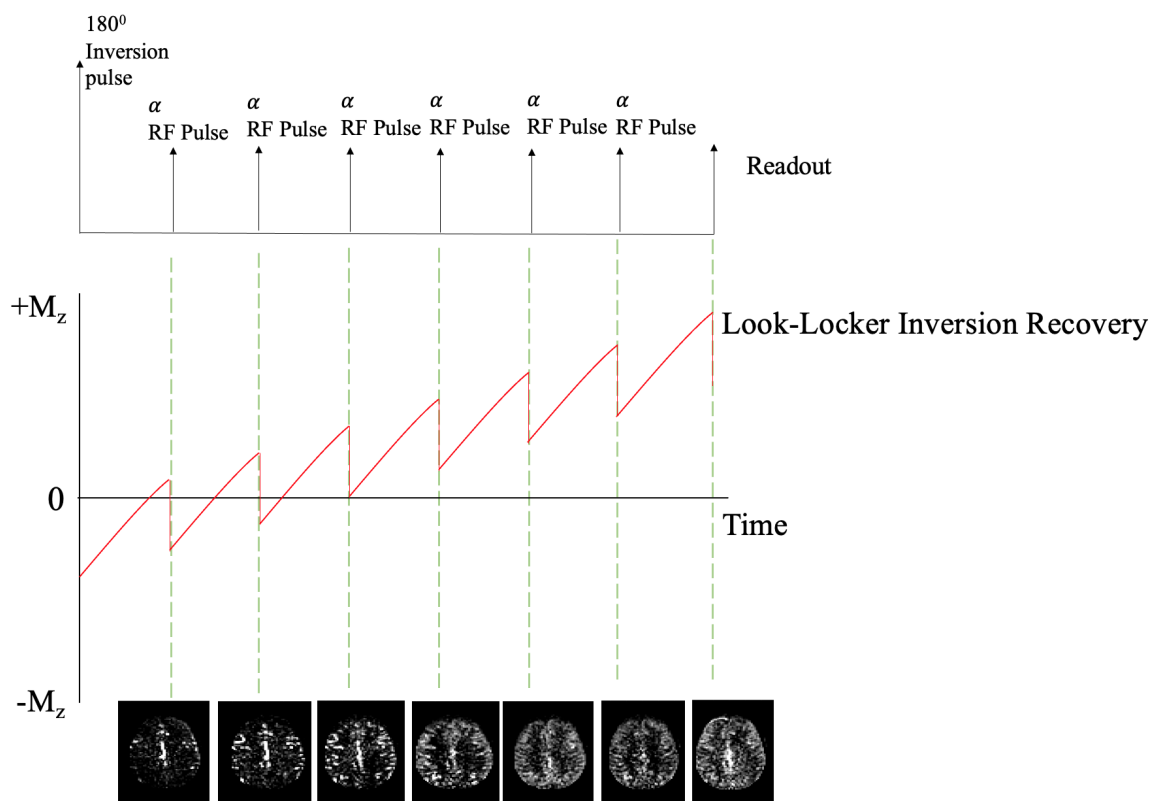


**Figure 2.4** the Look-Locker readout pulses in ASL sequence, changes in the longitudinal magnetization with low flip-angle excitation pulses and perfusion-weighted images over time.

In 2001, Gunther et al. used the combination of LL readout with a flow alternating inversion recovery (FAIR) labeling scheme, which is one of PASL sequences [8]. In 2006, Petersen et. al. combined signal targeting by alternating radiofrequency (STAR) labeling of arterial regions with LL readout in order to speed up the acquisition, while

acquiring multiple images at different time points in a single slice [41].

There are some disadvantages of LL, like the need of a relatively complex model for CBF calculation, because repeated image acquisitions by employing low flip angle RF pulses affects the labeled blood that has already reached the imaging volume [42]. So, the effect of LL readout needs to be taken into account for the quantification of CBF. Moreover, the loss of SNR is seen in images. Lastly, ASL MRI with LL doesn't cover the whole brain, because the repeated acquisitions allow only limited time for acquiring multiple slices.

#### 2.5.4.2 Time-Encoded pCASL MRI

In 2007, Gunther proposed te-pCASL to sample ASL signal with high time and SNR efficiency using a Hadamard matrix [13]. The Hadamard matrix is a square matrix consisting of either +1 or -1 entries. In ASL MR, each row of this matrix represents the labeling and the sum of the column widths of this matrix is equal to the total labeling duration. The main idea of this technique is to split the labeling into several small individual blocks called "sub-boli". Each sub-boli has different labeling duration and TI. Sub-boli is tagged as either "control" or "label" in accordance with the entry sign of the Hadamard matrix. Because the first column contains only label, this column doesn't generate a perfusion-weighted image. So, the first column of the Hadamard matrix is removed ( $N \times N-1$ ) [43]. Figure 2.5 shows the control and label pCASL sequence schematics, and also a te-pCASL with Hadamard-8 matrix sequence. In the Hadamard-8 matrix scheme, a long labeling duration (b) is divided into consecutive eight sub-boli with different labeling durations. In control situations (c) where the value of entry is "-1", labeling is not applied similar to the control image scheme (a). On the other hand, labeling is applied during "+1" sub-boli like in the label image scheme (b). Encoded image means the acquired image includes the summation of label and control signals coming from all the sub-boli during one row of the Hadamard matrix.

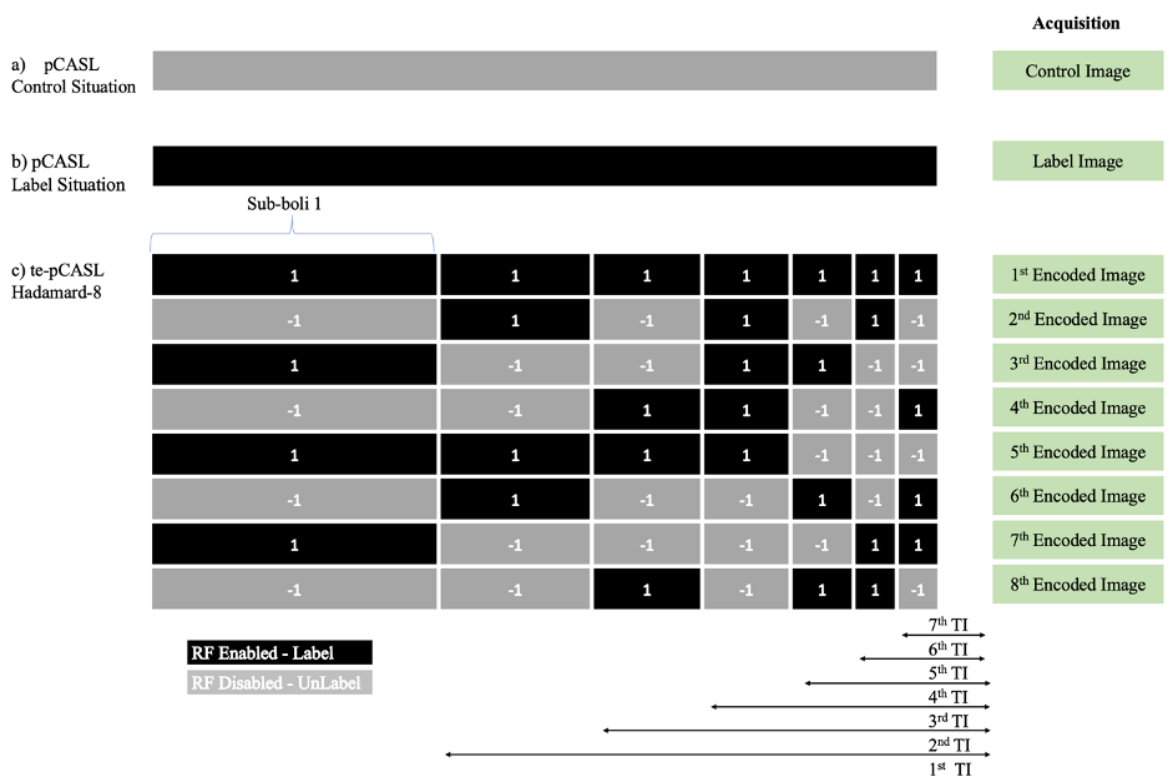


**Figure 2.5** The schematic of the pCASL control (a), label (b) sequences and te-pCASL with Hadamard-8 sequence (c).

In the decoding process, "1" and "-1" correspond to addition and subtraction, respectively. The ASL signal having unique combination of labeling duration and TI is calculated by either adding or subtracting encoded images in accordance with the signs (1 = "add" and -1 = "subtract") of entries in each column (Figure 2.6). When a decoded image is calculated for one column, its sign is applied to the encoded images. Each decoded image includes signals coming from just one column, because the signals coming from the other columns cancel each other out. Decoded images correspond to perfusion-weighted images with different TIs for each sub-boli. Figure 6 shows the calculation of the 1st decoded image. First, the entries of the first column are applied to all encoded images. While the total signal of first column (sub-boli) is equal to the subtraction of 4 label (4 L) and 4 control (4 C) signals, the label and control signals of all other columns (sub-boli) will cancel out. For example, for the second column, total signal is the summation of (L-L+C-C+L-L+C-C) and is equal to zero. As can be seen,

te-pCASL uses the natural ordering advantage of Hadamard matrix for decoding and encoding. Moreover, te-pCASL has higher time efficiency when compared to traditional pCASL. In pCASL,  $2 \times (N-1)$  measurements are needed to acquire images with different  $(N-1)$  TIs, because control and label images are acquired separately. On the other hand,  $N$  measurements are required to generate perfusion-weighted images with  $(N-1)$  different TIs in te-pCASL. Also, te-pCASL image has same SNR with respect to pCASL with the same labeling duration and the same TI [44]. It was also observed that ATT maps acquired with te-pCASL were very similar to that of quantitative STAR labeling of arterial region ASL-MRI technique [44]. Also, new combinations of Hadamard encoded labeling have been developed by adjusting the duration of each individual sub-boli to compensate for label decay.

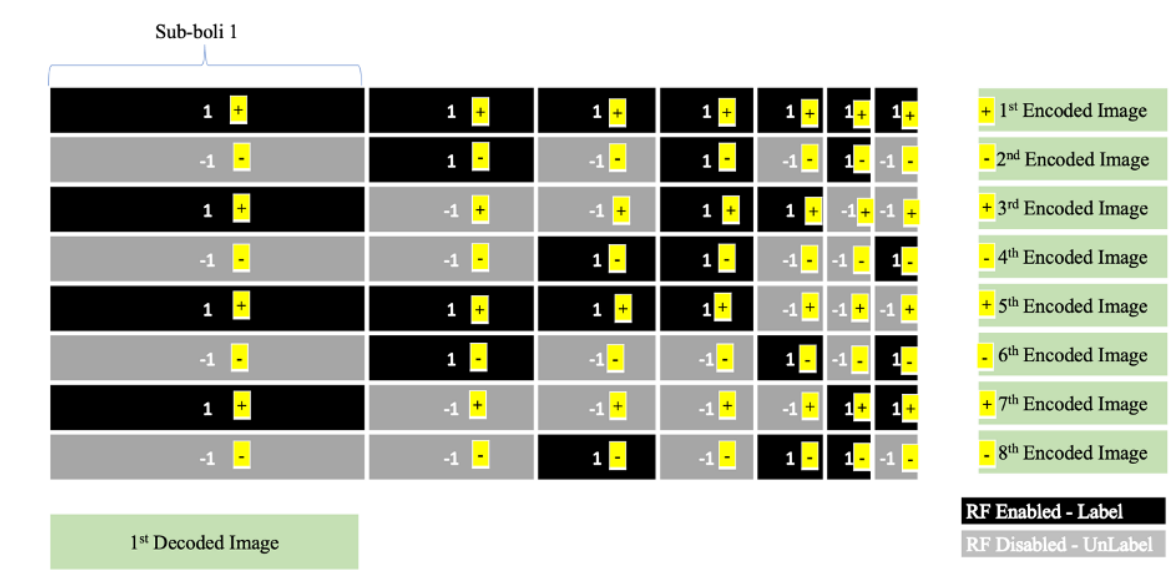


**Figure 2.6** The schematic of the pCASL control (a), label (b) sequences and te-pCASL with Hadamard-8 sequence (c).

There is one issue about te-pCASL MRI. Before decoding, acquired image includes all label and control encoded image information. During decoding, the information of sub-boli encoded images at other TIs is supposed to be zero in order to accurately calculate the ASL signal at one TI. If there are signal fluctuations in encoded images at any TI due to pulsatile flow, the difference of the signals coming

from the other sub-boli images is not zero, because these signal fluctuations cause the difference contrast in encoded images [14]. This has been dubbed the 'shine-through effect'.

## 2.6 Perfusion Deficits in Parkinson's Disease

Neurodegenerative diseases are a heterogeneous group of progressive neurological disorders that are characterized by progressive neuronal loss in the central nervous system. Common neurodegenerative diseases are Alzheimer's disease (AD), PD, amyotrophic lateral sclerosis and prion diseases [45]. The CBF values could provide information about the neuronal activity of the brain at both normal and diseased states [46]. Cerebral perfusion disturbances and hypoperfusion have been associated with impairment in cognition and eventually dementia [47–57].

The common consensus labels objectifiable cognitive impairment without functional impairment "mild cognitive impairment" (MCI), and considers it a transitional phase between normal cognition and dementia in progressive neurodegenerative diseases. However, determining cognitive impairment is far from objective, instead depending on the arbitrarily predefined stdv cutoffs of the neuropsychological test scores. This arbitrariness may be a particularly issue in PD, because a liberal stdv cut-off of -1 leads to as high as 92.1%, but a stringent one of -2 leads to as low as 9.9% prevalence of MCI among patients with PD [58]. Furthermore, the current diagnostic criteria of idiopathic PD rely solely on motor symptomatology [59]. However, considering the caudo-rostral progression of the PD pathology, starting from the lower brainstem, motor symptoms of the disease, reflecting the involvement of nigral dopaminergic neurons, already correspond to the midstages of the disease [60]. Nigro-striatal dopaminergic loss not only deprives the motor circuit, thus leading to the diagnostic motor symptoms, but also the parallel frontostriatal circuits, presumably subserving executive functions [61]. Therefore, hypothetically, a dysexecutive syndrome may well accompany the initial motor signs of the disease. Accordingly, MCI in PD (PD-MCI) was reported to be present at the time of the diagnosis, before the initiation of dopaminergic replacement,

in the so-called *denovo* patients [62]. A critical review of the relevant literature by the Movement Disorder Society (MDS) Task Force reported that PD-MCI was present in 26.7% of PD patients starting from the early stages of the disease [63].

Additionally, PD-MCI was associated with a higher likelihood of conversion into dementia in one longitudinal study [64]. However, every type of MCI may not be malignant in the context of PD, in the sense that there may be "benign" subtypes that do not progressively deteriorate, ultimately converting into dementia, and remain stable over time. Martinez-Horta and Kulisevsky proposed that while frontostriatal deficits leading to dysexecutive syndrome may be the benign, nonprogressive subtype, the impairment of specific functions that depend on posterior cortical regions, such as visuospatial, language, and memory functions, may represent the malignant, progressive subtype [65]. This distinction was called the "dual syndrome hypothesis" [66]. The authors suggested that, while frontostriatal defects appear more related to dopaminergic deficits, posterior-cortical defects might obey multiple neurotransmitter failures. After the above-mentioned critical review, the MDS Task Force subsequently published guidelines for the diagnosis of PD-MCI [67], and the current clinical practice mostly follows those guidelines, nevertheless utilizing arbitrarily determined stdvs of mean neuropsychological scores for PD-MCI diagnosis. Therefore, there is a dire need for developing surrogates of progressive cognitive impairment in PD, to use them as biomarkers in future studies, such as drug trials aiming to prevent disease progression.

Disease signatures, as obtained from multimodal neuroimaging, are promising candidates for being such surrogates. A number of studies used the ASL MRI technique for studying cerebral perfusion in PD [49–56]. Decreased perfusion in the parietooccipital cortex (POC), cuneus, precuneus, and posterior cingulate cortex (PCC) in PD compared to healthy controls (HC) has been reported [49], which indicates a pattern commonly called "posterior hypoperfusion" (PH). Three other studies also reported PH in PD subjects compared with HC [50, 51, 56]. In terms of intrinsic connectivity networks (ICNs) that parcellate the brain into functionally connected regions based on resting-state functional MRI (rs-fMRI), the stated posterior midline and lateral areas and the dorsolateral prefrontal areas very likely correspond to the default-mode

network (DMN) and visual network (VN), which are not under dopaminergic modulation, and top-down control networks, such as frontoparietal (FPN), cinguloopercular, and dorsal attention (DAN) networks, which are mainly under dopaminergic modulation [68, 69]. Some genetic factors have been implicated as risk factors in cognitive decline [70, 71]. These include polymorphisms in the microtubule-associated protein tau gene (MAPT), which encodes the protein that stabilizes microtubules. There are two MAPT haplotype classes, H1/H1 and H1/H2. It appears that MAPT H1/H1 haplotype (versus H1/H2 haplotype), apart from playing a significant role in tauopathies, not only predisposes to PD [72], but also leads to progressive cognitive decline into PD dementia (PDD) [71, 73].

## 2.7 Aim

ASL MRI techniques acquired at multi-TI including ASL MRI with LL readout and te-pCASL MRI have been proposed to estimate CBF maps while compensating for the delays in blood transit. However, these techniques suffer from some problems. While ASL MRI with LL readout is prone to errors in CBF estimation due to its complex model, te-pCASL MRI displays an artifact called shine-through effect. The specific aims of this thesis are:

1. To write an in-house program for modeling multi-TI ASL MRI signal acquired with LL readout method. The application of low flip-angle excitation pulses during the readout was taken into account in the model. The effect of LL was modelled by combining the general kinetic model and arterial blood volume correction.
2. To investigate voxel-wise differences of calculated CBF values between PD-MCI, cognitively normal PD (PD-CN), and healthy controls (HC).
3. To discern possible brain perfusion-based signatures that correspond to cognitive decline in PD.

4. To apply machine learning algorithms to classify cognitive deficits in PD based on CBF values calculated at different functional brain parcellations obtained from resting state fMRI [74].
5. To assess the perfusion deficits in PD having different MAPT haplotypes.
6. To build a simulation model to compare the longitudinal magnetization of blood in traditional pCASL MRI and te-pCASL MRI.
7. To compare the noise characteristics of traditional pCASL and te-pCASL datasets acquired from one subject at different TIs.
8. To understand whether the Hadamard labeling scheme has any effects on the high signal fluctuations seen in te-pCASL MRI.
9. To assess the appearances of the shine-through effect when the global or selective BGS inversion pulses are applied in te-pCASL.

### 3. MATERIALS and METHODS

#### 3.1 ASL MRI with LL readout data

##### *Subjects*

Twenty-seven PD-MCI, 26 PD-CN, and 15 HC subjects were scanned using ASL MRI technique with LL readout. Istanbul University Clinical Research Ethics Committee approved the study protocol, and all subjects provided written informed consent after the nature of the examination was explained.

##### *Diagnostic Criteria and Assessment*

All patients were examined by expert neurologists at Behavioral Neurology and Movement Disorders Unit, Department of Neurology, Istanbul University, Istanbul, Turkey. Firstly, PD status of the subjects was diagnosed according to UK Brain Bank Criteria [59]. After, some main criteria were employed to include the subjects in this study. The first selection criterion was to graduate at least from the primary school to carry out neurophysiological tests (NPT) successfully. All neuropsychological tests were performed in the on period of the patients with PD. Another criterion is whether subjects use antidepressant or not because it has been reported that regional blood flow in brain changed in people using antidepressants [75]. Also, Geriatric Depression Scale was carried out to understand whether a subject is in depressed, because depressed patients might have changes in CBF with compared to non-depressed people [76].

After the selection of PD subjects, the severity of PD patients was diagnosed in accordance with MDS Task Force Guidelines [67]. Level I evidence, based on the instructions of the aforementioned guidelines, and Addenbrooke's Cognitive Examination-Revised (ACE-R) cut-off score of  $\geq 83$  were used to discriminate PD-CN and PD-MCI [77]. The Hoehn and Yahr Scale was used to determine the stage of PD dis-

ease [78]. The Movement Disorders Society-Unified Parkinson’s Disease Rating Scale (MDS-UPDRS) were performed on all patients to quantify a total symptom severity score and a motor (MDS-UPDRS III) and various non-motor-domain sub-scores [79]. UPDRS is a test to quantify motor manifestations of PD by employing the questions related four subsections. The questions in subsection 1 assessed mental, behavioral, and mood situations of PD. Questions which patients were asked were related to activities of daily living. In subsection 3, clinician rates the motor manifestations of subjects. In Subsection 4, questions cover the complications of therapy. Results obtained from these subsections were evaluated by the interviewer and clinical observation. The total score of UPDRS was calculated by summation of the subsection results to detect a patient’s disease progression [80].

Table 3.1 shows the demographic characteristics of the subjects. Three subject groups were matched for age, sex, and education ( $P > 0.05$ ). Hoehn and Yahr scores, disease durations, and levodopa dosages of the PD-CN and PD-MCI patients were not statistically significantly different ( $P > 0.05$ ). UPDRS-III ( $P = 0.06$ , not significant) and UPDRS-total ( $P = 0.05$ ) scores of PD-MCI patients were higher than those of PD-CN patients.

**Table 3.1**  
Demographics of subjects.

	HC	PD-CN	PD-MCI	P
Sex (M:F)	11:04	16:10	21:06	0.43
Age	$58.67 \pm 6.30$	$60.15 \pm 8.98$	$64.00 \pm 8.14$	0.09
Education Years	$11.00 \pm 3.80$	$10.08 \pm 4.05$	$9.00 \pm 3.67$	0.26
Hoehn Yahr	N/A	$1.77 \pm 0.51$	$1.92 \pm 0.56$	0.32
Disease duration, years	N/A	$5.42 \pm 3.04$	$6.62 \pm 3.54$	0.20
Levodopa dosage, mg/day	N/A	$688.72 \pm 341.75$	$839 \pm 384.34$	0.13
MDS-UPDRS-III	N/A	$26 \pm 10.80$	$32.40 \pm 13.11$	0.06
MDS-UPDRS-Total	N/A	$45.23 \pm 16.79$	$55.11 \pm 20.75$	0.05

N/A: not applicable

### *Neuropsychological Tests*

An extensive neuropsychological test battery was employed for assessing the cognitive status of all subjects. The following tests were performed in this study. *Montreal Cognitive Assessment* Montreal Cognitive Assessment (MOCA) test was developed by Nasreddine et al. in 2005 for detecting MCI [81]. The MOCA test consists of one page administered in 10min. Total score is 30 points. Assessments are related to several cognitive functions including visuospatial/Executive, Naming, Memory, Attention, Language, Abstraction, Delayed Recall and Orientation (to time and place). If the score of 26 or above, participant is considered normal. Otherwise, there is MCI in participant.

#### *The Addenbrooke's Cognitive Examination Revised*

ACE-R [82] are employed for the identification of the general cognitive status. Also, the Mini-Mental State Examination (MMSE) is embedded in this test [83]. This test includes the questions related to five different cognitive domains including attention/orientation, memory, verbal fluency, language and visuospatial abilities. Total score of ACE-R is directly proportional to cognitive functioning.

#### *Stroop Test*

In 1935, John Ridley Stroop proposed the Stroop effect for the measurement of attention [84]. In this test, participants are supposed to say whether the color of the word and the meaning of the word on the card are same or not when a card is showed. This test has two steps from easy to hard. In the first step, the color and mean of the word are these same, while these are not same in the second part. During the test, brain needs to suppress wrong answer, which causes delay in the response. Score of this test is defined as the duration of interference task as a measure of resistance to interference.

#### *The Wisconsin Card Sorting Test*

The Wisconsin Card Sorting Test (WCST) has been used as a clinical neuropsychy-

chological instrument for executive functions [85]. It is a percentage of perseverative responses score as a measure of set-shifting by assessing abstract thinking, cognitive flexibility, and impairment. In this test, shapes on stimulus cards, which have different color, number and the forms, are seen to participant.

#### *The Benton's Judgment of Line Orientation Test*

The Benton Judgment of Line Orientation Test (JLO) has been employed as a measure of visual perception [86]. In this test, a participant is supposed to match line segments of different spatial orientation with a set of longer lines on a response card. Total score is based on the number of correct items with age and gender adjustments and categorizes the participants as normal, mild, moderate, and severely impaired.

#### *The Symbol-Digit Modalities Test*

The Symbol Digit Modalities Test (SDMT) has been developed for the examination of neurocognitive functions including attention, visual scanning, and motor speed [87]. Participant subjected to this test is supposed to insert the numbers, associated with one of the series symbols, into a blank space within a 90-second time limit participant is supposed.

#### ***Data Acquisition***

All subjects were scanned using a 3T clinical MR system (Philips Medical Systems, Best, Holland) with a 32-channel head coil. The brain MR protocol included ASL MRI and a  $T_1$ -weighted ( $T_{1w}$ ) MRI (TR/TE=8.31/3.81 ms, flip angle=8°, field of view (FOV)=240 mm x 240 mm, slice thickness=1 mm, matrix size=256 x 256, total scan duration=143 s). ASL MR images were acquired by using STAR labeling with multi-slice single-shot echo-planar imaging (EPI) readout with LL sequence at multiple inversion time (TIs) (TR/TE=250/16 ms, flip angle=40°, FOV=240 mm x 240 mm, matrix size=80 x 80, slice thickness=6 mm, spacing between slices=6.6 mm, number of dynamics=48, and total scan duration=248 s). Each slice was acquired at eight dif-

ferent TIs with eight distinct TIs (Figure 3.1). For the first slice, the minimum TI was set to 300 ms, and the maximum set to 2050 ms. The minimum TI of each consecutive slice was increased by 32 ms, whereas the minimum TI of the consecutive TI at the same slice was increased by 250 ms. Further, the data acquisition was repeated 30 times at each TI and slice to increase the SNR. The ASL MRI data acquisition was repeated three times to cover the whole brain.

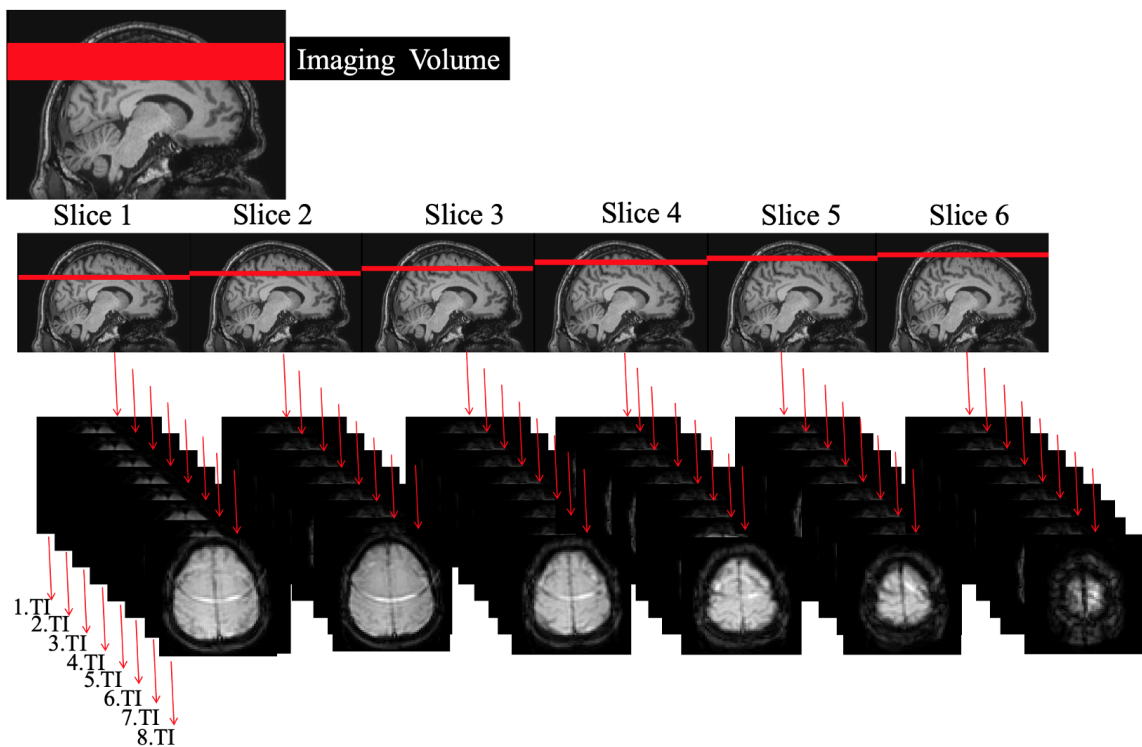


**Figure 3.1** The demonstration of six slices at different eight TIs.

### *Genetic Work-up*

DNA was extracted from venous blood using a genomic DNA purification kit (Jena Bioscience, Germany). Single nucleotide polymorphism genotyping for rs9468 (MAPT H1/H1 versus H1/H2 haplotype) was performed using Stratagene Mx3005p real-time PCR system (Agilent Technologies, USA).

### *CBF maps calculation*

ASL MR dataset acquired from each subject consisted of 1440 control and 1440 label images. An in-house program was developed in MATLAB (The MathWorks Inc., Natick, MA) for estimating the CBF maps. In the first step, control and label images were realigned and averaged after all images were arranged in accordance with their slice locations (Figure 3.2).

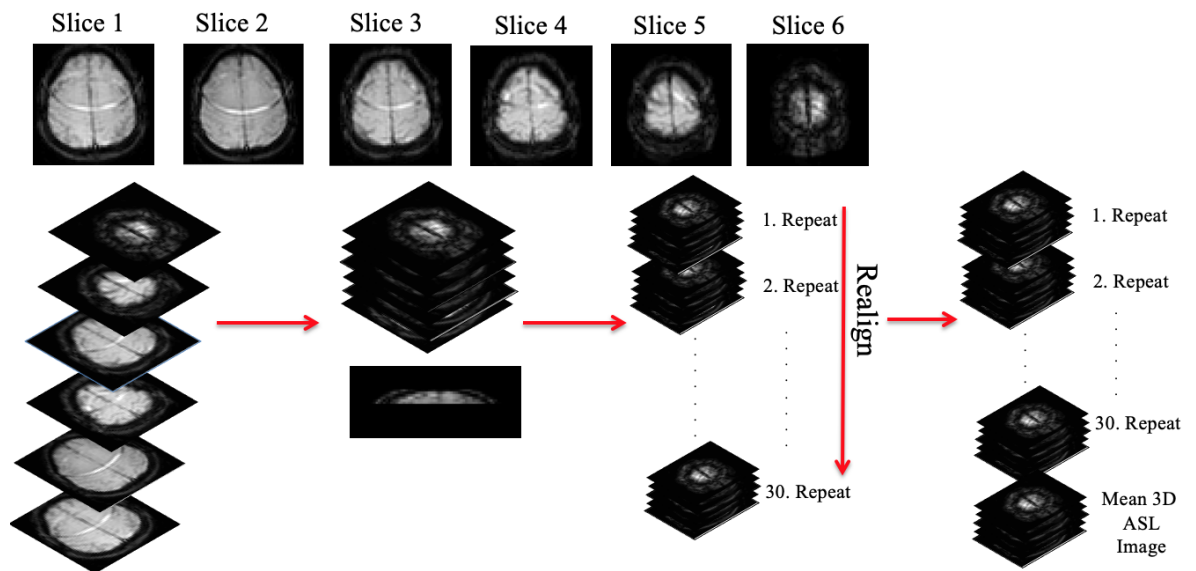


**Figure 3.2** ASL images of different slices were realigned at each TI for each repeat.

Then,  $\Delta M$  were created by subtracting mean realigned control images from mean realigned label images (Figure 3.3).

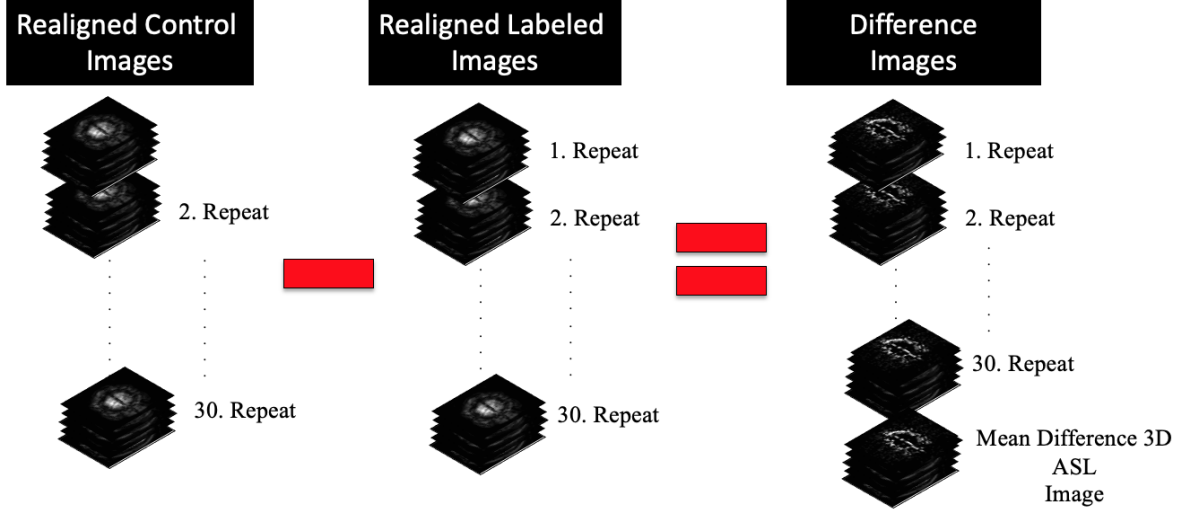


**Figure 3.3** The creation of difference images by subtracting the mean realigned control and label images.

The calculation of the main magnetization ( $M_0$ ) was based on the partial flip angle imaging. (Figure 3.4) shows the changes of longitudinal magnetization of control images by employing  $40^\circ$  flip angle RF pulses at eight TIs.  $\Delta TI$  time between the equally spaced readout flip angle RF pulses was 250 ms. Firstly, longitudinal magnetization of control images was saturated by employing  $90^\circ$  RF pulses. Afterwards, images were acquired by employing  $40^\circ$  flip angle RF pulses at different TIs.  $M_0$  was estimated for each pixel of mean control images with different TIs after accounting for flip angle excitation recovery (Figure 3.4) by employing the following formulas,

$$M_z^{(-)}(t) = M_0 \left( 1 - e^{-\frac{t}{T_{1blood}}} \right) + M_z^+(TI) e^{(-\Delta TI/TI)} \quad (3.1)$$

$$M_z^{(+)}(t) = M_z^-(t) \cos 40 \quad (3.2)$$

where  $T_{1blood}$  is the longitudinal relaxation of blood (1,664s). Non-linear least squares fitting was employed to estimate an unknown pixel of  $M_0$  map by fitting the above formula to the eight mean control pixel intensities [88].

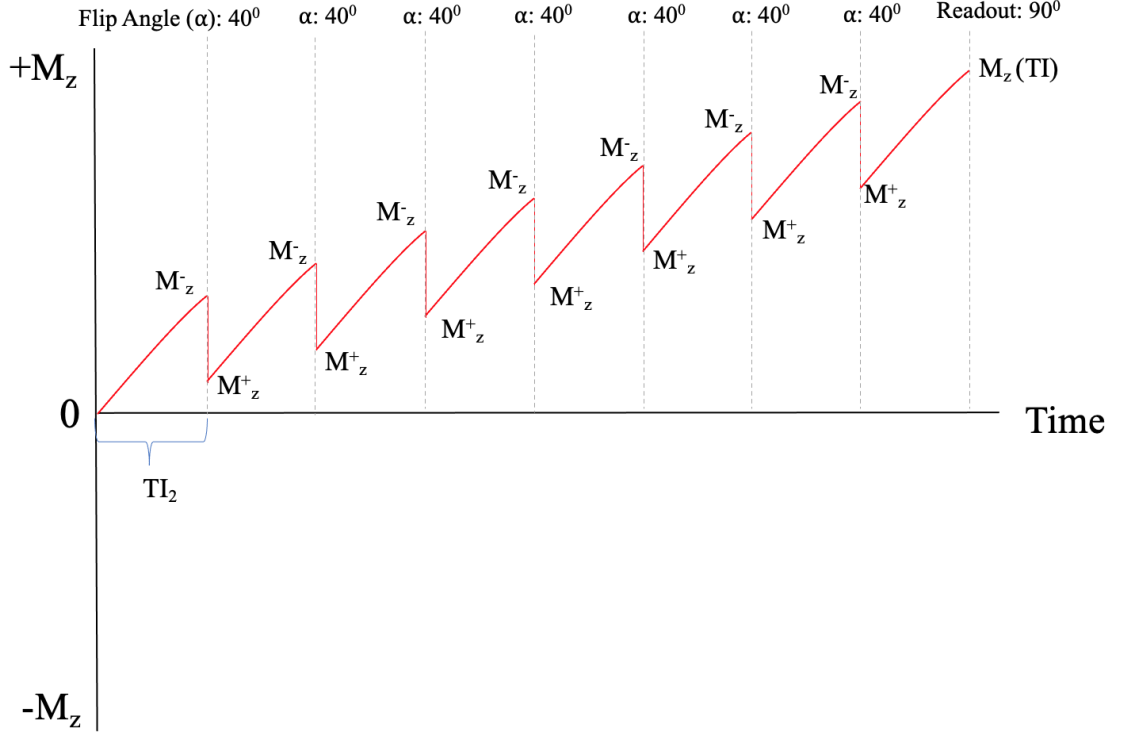


**Figure 3.4** The changes of longitudinal magnetization of control images during LL readout.

Additionally, the CBF calculations took into account the effect of intravascular component to minimize the high signal coming from arterial vessels. It was reported that difference of control and label images included an intravascular ( $\Delta M_{art}$ ) component, which represents that some of the labeled blood remains in vessels, and an extravascular ( $\Delta M_{tiss}$ ) component, which represents that some of the labeled blood remains in tissue [89]. The equation of  $\Delta M_{tiss}(t)$  based on the inflow turbo-sampling EPI-FAIR was described in detail in the 'ASL MRI Models of Quantification' section [7, 8]. On the other hand,  $\Delta M_{art}$  was described using,

$$\Delta M_{art}(t) = \begin{cases} 0, & t < \Delta t_a \\ 2M_{0b}\alpha e^{\frac{-t}{T_{1blood}}} aBV, & \Delta t_a \leq t \leq \Delta t_a + \tau_a \\ 0, & \Delta t_a + \tau_a < t \end{cases} \quad (3.3)$$

where  $\Delta M_{art}$  is the arterial bolus arrival time,  $\tau_a$  is the bolus duration (seconds) of the arterial bolus, and  $\alpha$  is the inversion efficiency (0.95).

The total signal of the perfusion-weighted image was the sum of these two components as,

$$\Delta M = \Delta M_{tissue} + \Delta M_{art}. \quad (3.4)$$

Therefore, eight pixels of  $\Delta M$  with different TIs was fitted to the model based on the sum of ( $\Delta M_{tiss}$ ) and ( $\Delta M_{art}$ ) using non-linear least square fitting in order to estimate all the pixels of the CBF map per slice. R-squared was calculated and checked to statistically measure how well the model fit the observed data points for M0 and CBF maps. Figure 3.5 shows the curve fit of one example pixel of the M0 map at eight TIs. After calculated CBF maps and T<sub>1</sub>w images were converted to ".nii" format in MATLAB, a brain mask was generated from the mean control images for each subject using the brain extraction tool of the FMRIB Software Library (FSL) (<http://fsl.fmrib.ox.ac.uk/fsl/fslwiki/>) software package to remove out-of-the brain tissue. The intensity threshold was selected as 0.3, 0.5 and 0.7 for each subject, respectively. After visually checking the brain masks, the best mask was selected for each patient. Subsequently, this mask was applied to the quantitative CBF maps to remove the out-of-brain voxels. Figure 3.6 shows the mask of a mean control image (a) using 0.3 (b), 0.5 (c) and 0.7 (d) intensity thresholds. As can be seen easily, 0.3 intensity threshold was selected as the optimal one, because 0.5 and 0.7 intensity thresholds caused elimination of brain tissue.

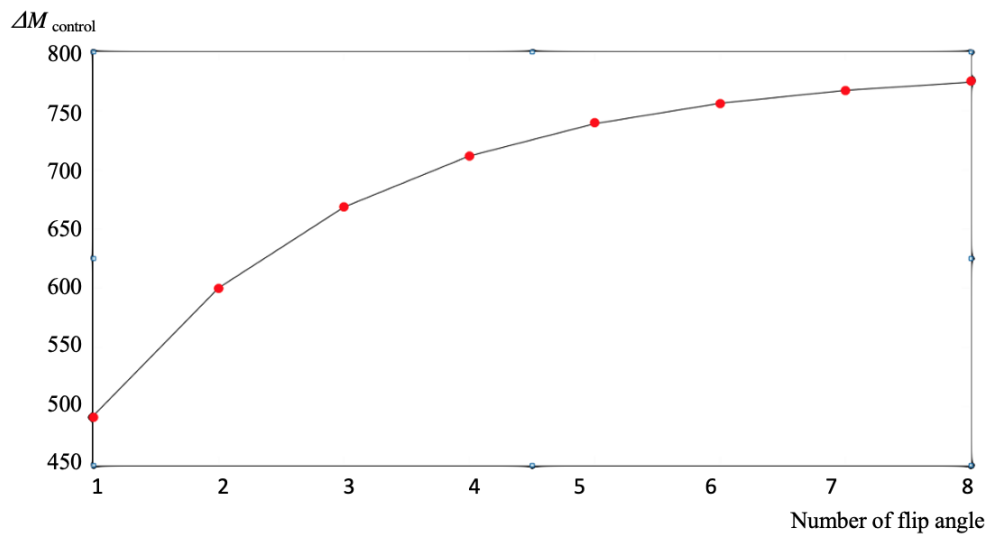


**Figure 3.5** M0 curve fit for one example pixel.

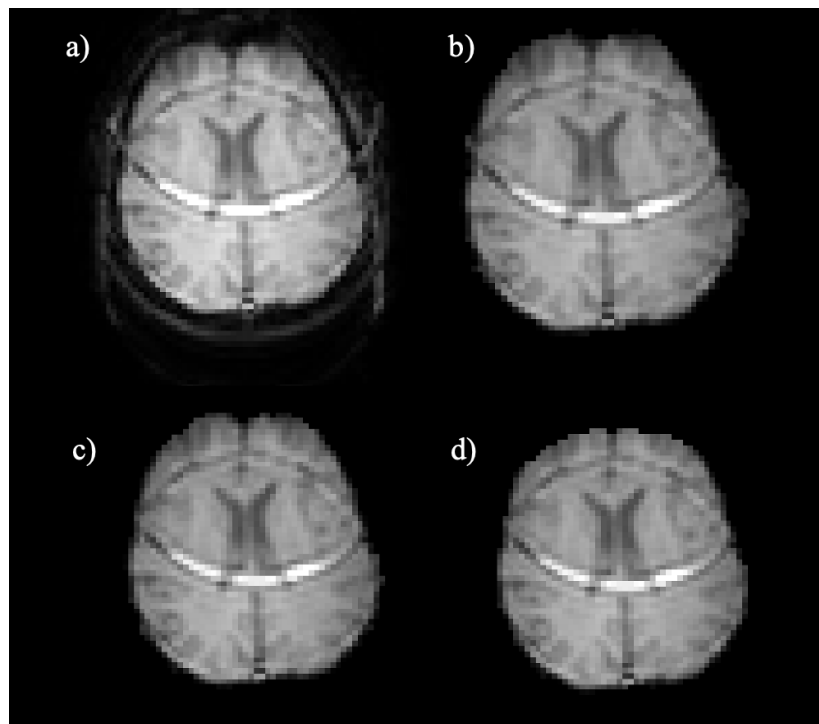


**Figure 3.6** Masking of a mean control image (a) using 0.3 (b), 0.5 (c) and 0.7 (d) intensity thresholds, respectively.

### *Registration*

Estimated CBF map of each subject was converted to a single 3D volume in NIFTI format in MATLAB, which was coregistered to the high-resolution T<sub>1</sub>w MRI (b) of the subject. The T<sub>1</sub>w MRIs were then spatially normalized to the Montreal Neurological Institute brain atlas (MNI152) (a) using FSL, and the transformation matrix for each subject was obtained. The same transformation matrix was applied for coregistration of the CBF map (c). Figure 3.7 shows the MNI152 brain atlas (a), registered T<sub>1</sub>w image (b) and CBF map (c) of one example HC subject.

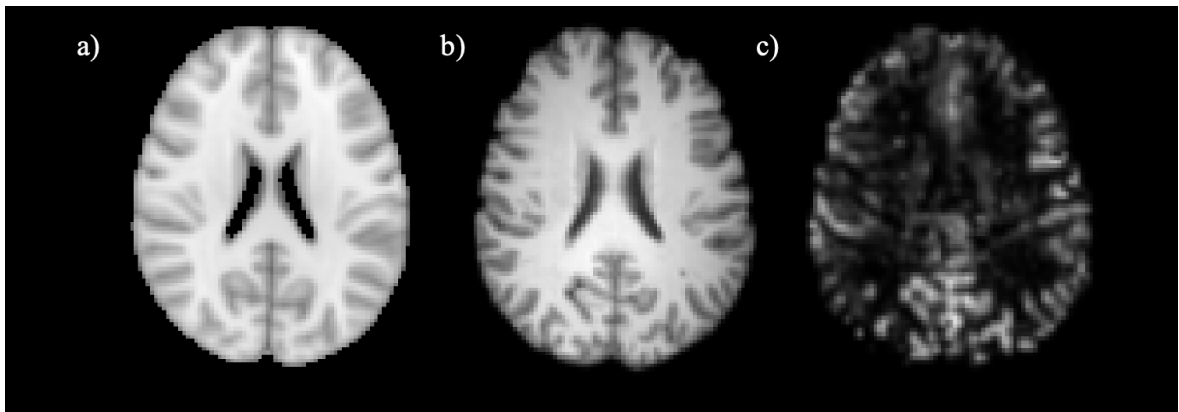


**Figure 3.7** Registered T<sub>1</sub>w image (b) and CBF map (c) of one example HC subject onto MNI152 brain atlas (a).

### *Statistical Analysis*

Neuropsychological scores were compared among the three subject groups using a Kruskal-Wallis test followed by post hoc Dunn-Sidak tests. Moreover, neuropsychological scores were compared between the two genetic groups of PD patients (MAPT H1/H1 haplotype versus H1/H2 haplotype), first in the entire PD (all-PD) group, then in the PD-MCI group alone using a Mann-Whitney U test. Bonferroni multiple comparison correction was applied, and a  $P < 0.006$  was considered statistically significant for the Kruskal-Wallis test and the Mann-Whitney U test. A  $P < 0.05$  was considered statistically significant for post hoc comparisons.

Whole brain voxelwise statistical tests were applied on CBF maps with the SPM12 software package (<http://www.fil.ion.ucl.ac.uk/spm/>). GM masks were generated from the segmented and normalized GM images of the subjects with the probability of being GM larger than 95%. Subject-specific GM masks were then combined and binarized with the group level threshold of 5% to produce a GM group template to exclude non-gray-matter voxels. Figure 3.8 shows the overlay of standard probability map of GM in SPM and the GM mask created for our subject population.

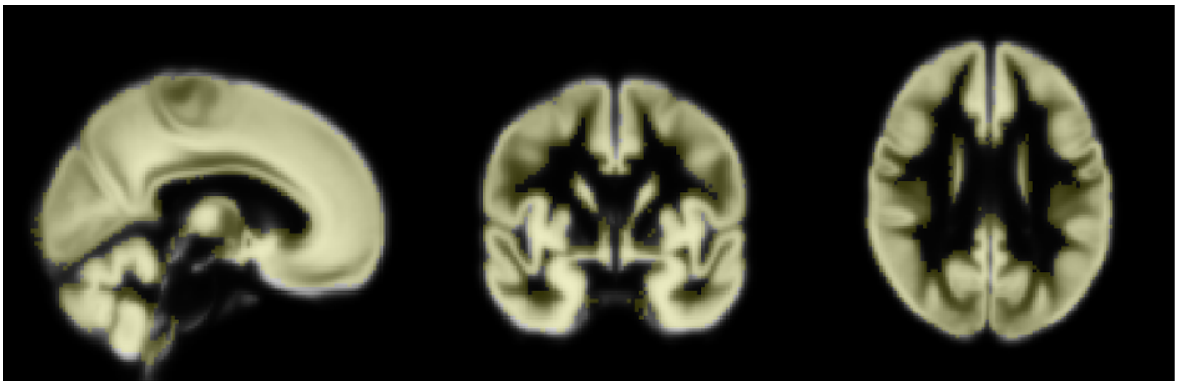


**Figure 3.8** The overlay of standard probability map of GM in SPM (grey) and the GM mask created for subject population (yellow).

First, a one-way analysis of variance was performed to compare CBF maps between HC, PD-CN, and PD-MCI, followed by pairwise post hoc comparisons. Afterward, the two subgroups of the all-PD group, which were divided according to possessing the risky H1/H1 haplotype, were compared. Whole-brain voxelwise differences of CBF values of the all-PD group and only-PD-MCI group were assessed by a two-sample t-test. For all statistical tests, the level of statistical significance was set to uncorrected cluster forming threshold of  $P < 0.005$  and cluster level familywise error correction threshold of  $P < 0.05$ , with a minimum cluster size of 50 voxels.

Two PD groups (PD-CN and PD-MCI) were first collapsed as a single group of 53 individuals and then divided into two groups of low performers (LP) and high performers (HP) in general cognitive, executive and visual domains. For the general cognitive domain, composite z-scores of ACE-R, MMSE and MOCA were calculated

as the average of their respective z-scores for each patient, and the lowest and highest tertile z-scores were taken as LP and HP, respectively. Similarly, for the visual domain, lowest and highest tertile z-scores of JLO were used to determine LP and HP, respectively. For the executive domain, composite z scores of WCST percentage of perseverative response and Stroop interference duration measures were used, and highest and lowest tertile z-scores were taken as LP and HP, respectively. Furthermore, the same procedure was applied to the scores of all of the participants including the HC group. Then, CBF maps of LP and HP in these cognitive domains were compared using two-sample t-tests for both PD group and all participants group in SPM12 software package (<http://www.fil.ion.ucl.ac.uk/spm/>). For all of the performed two sample t-tests, the level of statistical significance was set to uncorrected cluster forming threshold of  $P < 0.005$  and cluster level FWE threshold of  $P < 0.05$ , with a minimum cluster size of 50 voxels.

The MNI coordinates produced by the whole brain voxelwise statistical analyses were visually matched to 100 parcellations of the cerebral cortex defined by Schaefer et al. [74] corresponding to Yeo et al.'s [68] seven rs-fMRI networks. For the cerebellar components, the MNI coordinates were matched to functional connectivity maps proposed by Buckner et al. [90].

### *Machine Learning*

Finally, machine learning algorithms, including logistic regression, support vector machine (SVM), and k-nearest neighbor (kNN) were employed for classification of HC vs PD-MCI, HC vs PD-CN, and HC vs all-PD using the voxel intensities of the posterior hypoperfusion regions. Principal component analysis (PCA) was used as a dimensionality reduction technique. The principal components explaining 95% of the total variance were employed as features for each classification. Synthetic minority class over-sampling (SMOTE) method was used to overcome the class imbalance problem, and the minority class was oversampled to match its sample size to the majority class [91]. After oversampling, 50-fold cross-validation was employed to assess the performance of the classification algorithms in terms of accuracy, sensitivity and

specificity.

## 3.2 te-pCASL MRI data

### *Simulation*

A simulation model was built in MATLAB to create traditional pCASL and te-pCASL datasets. Firstly, ASL MRI was modelled schematically with a two compartment model (Figure 3.9). According to this model, the magnetically labeled protons first arrive at the arterial vessels in the imaging volume. The arrival time to arterials is termed as the arterial transit time (ATT). Afterwards, they keep traveling within the imaging volume and arrive at the tissue compartment. The time from labeling to arriving to tissue compartment defines the tissue transit time (TTT). The signal acquired at TI (imaging time) depends on the exact location of the labeled protons in the brain.

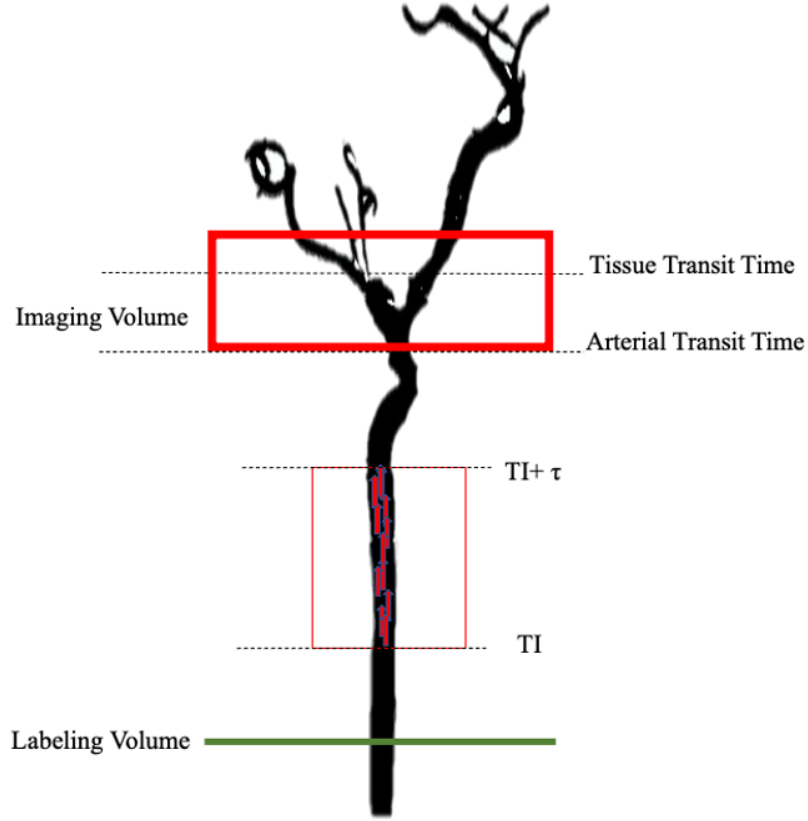


**Figure 3.9** The schematic model of the ASL MRI technique.

There are six different situations possible for where the labeled protons could be found in the brain when readout RF pulse is applied. All these situations were formulated by assessing the longitudinal magnetization changes of labeled protons in arterial vessel and tissue compartment over time, separately. The general formula of the longitudinal magnetization ( $M_z$ ) is,

$$M_z(t) = M_z(t_0)e^{-(t-t_0)/T_1} + M_0(1 - e^{-(t-t_0)/T_1}), \quad (3.5)$$

where  $T_1$  is relaxation time. In arterial vessels, the longitudinal magnetization of labeled spins is calculated by employing the following formula,

$$M_z(t) = M_0e^{-(t-t_0)/T_{1blood}} + M_0(1 - e^{-(t-t_0)/T_{1blood}}) = M_0(1 - \alpha * e^{-(t)/T_{1blood}}) \quad (3.6)$$

where  $T_{1blood}$  is relaxation time of the blood, and  $\alpha$  is labeling efficiency. In tissue

vessels, the longitudinal magnetization of labeled spins is calculated as,

$$M_z(t) = M_0(1 - \alpha e^{-TTT/T_{1blood}})e^{-(t-TTT)/T_{1tissue}} + M_0(1 - e^{-(t-TTT)/T_{1tissue}}) \quad (3.7)$$

where  $T_{1tissue}$  is the relaxation time of the tissue. In the first situation, the signal acquired from the imaging slice is equal to zero, because no labeled spins have arrived at the arterial vessels within the imaging volume,

$$Signal_{Label} = Signal_{arterial} = 0, \quad t < ATT \quad (3.8)$$

In the second situation, first labeled spins arrive at the arterial vessels within the imaging volume,

$$Signal_{Label} = \int_0^{TI+\tau-ATT} M_0 \alpha e^{-(TI+\tau-t)/T_{1blood}}, \quad t - \tau < ATT < t < TTT \quad (3.9)$$

In the third situation, all labeled spins are residing in arterial vessels and the signal comes from only the arterial vessels,

$$Signal_{arterial} = \int_0^\tau M_0 \alpha e^{-(TI+\tau-t)/T_{1blood}}, \quad ATT < t - \tau < t < TTT \quad (3.10)$$

After that, the first labeled spins arrive within the tissue compartment, but other labeled spins still stay in the arterial vessels. So, in the fourth situation, the total signal is the sum of signal coming from not only arterial vessels, but also tissue compartment,

$$Signal_{label} = Signal_{arterial} + Signal_{tissue}, \quad ATT < t - \tau < TTT < t \quad (3.11)$$

$$Signal_{arterial} = \int_{TI+\tau-TTT}^\tau M_0 \alpha e^{-(TI+\tau-t)/T_{1blood}} \quad (3.12)$$

$$Signal_{tissue} = e^{-TTT/T_{1blood}} \int_0^{TI+\tau-TTT} M_0 \alpha e^{-(TI+\tau-t)/T_{1tissue}} \quad (3.13)$$

In the fifth situation, all labeled spins have arrived at the tissue compartment and will stay within the tissue compartment. So, the signal comes only from the tissue compartment,

$$Signal_{tissue} = e^{-TTT/T_{1blood}} \int_0^\tau M_0 \alpha e^{-(TI+\tau-t)/T_{1tissue}}, \quad TTT < t - \tau \quad (3.14)$$

On the other hand, when labeling duration is long, the first labeled spins will already arrive in the tissue compartment through the arterial vessels, whereas the last labeled spins didn't reach the arterial vessels within the imaging volume yet. As a result, in the sixth situation, the total signal can be modelled as the sum of the signals coming from arterial vessels and the tissue compartment,

$$Signal_{Label} = Signal_{arterial} + Signal_{tissue}, \quad t - \tau < ATT < TTT < t \quad (3.15)$$

$$Signal_{arterial} = \int_{TI+\tau-TTT}^{TI+\tau-ATT} M_0 \alpha e^{-(TI+\tau-t)/T_{1blood}} \quad (3.16)$$

$$Signal_{tissue} = e^{-TTT/T_{1blood}} \int_0^{TI+\tau-TTT} M_0 \alpha e^{-(TI+\tau-t)/T_{1tissue}} \quad (3.17)$$

This signal model was based on one labeling duration and TI and is suitable for pCASL MRI. In te-pCASL, the number of acquired encoded images is the same as the Hadamard matrix of order, N. One encoded image is the total signal coming from a combination of control and label blocks. The signal of one encoded image is therefore,

$$Signal_{total} = \sum_{i=1}^{N-1} (j Signal_{control,block} + (1-j) Signal_{label,block}) \quad (3.18)$$

where j=0 for label, j=1 for control. Because signal coming from a control block is zero, the signal of each encoded image is described as,

$$Signal_{total} = M_0 \alpha \sum_{i=1}^{N-1} \int_0^{\tau_i} e^{-(\Delta_i + \tau_i - t)/T_1} \quad (3.19)$$

After defining these formulas based on a two compartment model for pCASL MRI and te-pCASL MRI, the next step was to build a simulation model in MATLAB to assess the longitudinal magnetization of the label spins in time. First of all, GM, WM and arterial vessels maps were created by segmenting the MNI152 brain atlas using SPM12 software package (<http://www.fil.ion.ucl.ac.uk/spm/>) (Figure 3.10). Then, ATT and TTT maps were created. For these maps, the transit time ranges of the arterial vessels and the tissue were taken from the literature (Figure 3.11) [26,92].

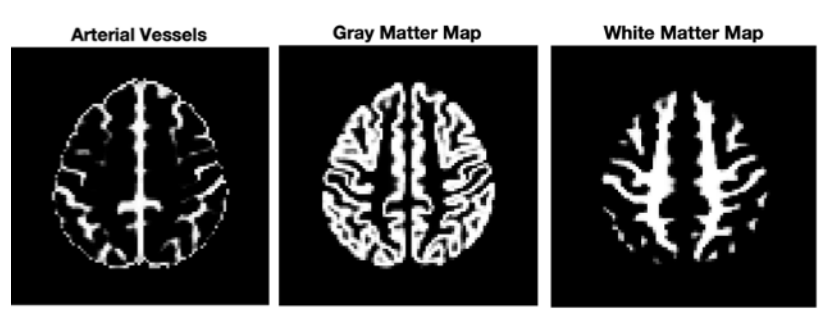


**Figure 3.10** Generated arterial vessels, GM and WM maps.

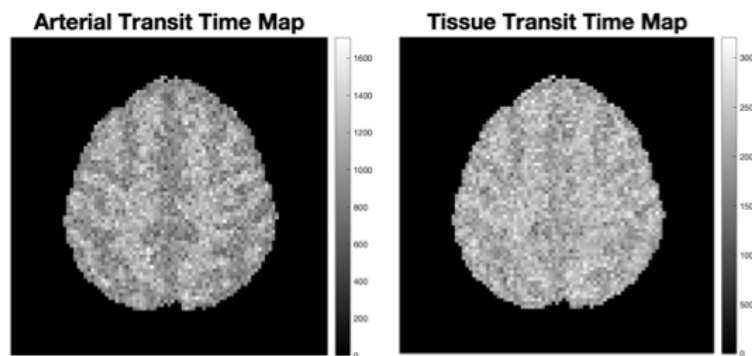


**Figure 3.11** Generated ATT and TTT maps.

The labeling durations were set as 1175 ms, 683 ms, 482 ms, 374 ms, 305 ms, 257 ms, 224 ms and TIs were 2825 ms, 2142 ms, 1660 ms, 1286 ms, 981 ms, 724 ms and 500 ms for pCASL MRI. Labeling durations were chosen to provide sufficient SNR for each TI. The control and label images of pCASL MRI were created with 32 repetitions with different sampled noise levels. Perfusion-weighted images were generated by subtracting control and label images. For te-pCASL MRI, a Hadamard-8 matrix was

applied. Therefore, the total labeling time was divided into seven consecutive sub-boli. Labeling durations of sub-boli were 1175 ms, 683 ms, 482 ms, 374 ms, 305 ms, 257 ms, 224 ms and TI was 500ms, respectively for the simulated te-pCASL MRI. These sub-boli were tagged either "control" or "label" considering the sign of entries of the Hadamard matrix (Figure 3.12). For a "label" sub-boli, labeling was performed during the duration of the block. For a "control" sub-boli, there was no effective inversion. Each encoded image in te-pCASL was repeated eight times with different noise levels. For all te-pCASL MRI, the decoding process was done in order to create perfusion signal intensity ( $\Delta M$ ) for each unique combination of labeling duration and TI.

-1(L)	-1(L)	-1(L)	-1(L)	-1(L)	-1(L)	-1(L)	Delay	Encoded Image
+1(C)	-1(L)	+1(C)	-1(L)	+1(C)	-1(L)	+1(C)	Delay	Encoded Image
-1(L)	+1(C)	+1(C)	-1(L)	-1(L)	+1(C)	+1(C)	Delay	Encoded Image
+1(C)	+1(C)	-1(L)	-1(L)	+1(C)	+1(C)	-1(L)	Delay	Encoded Image
-1(L)	-1(L)	-1(L)	+1(C)	+1(C)	+1(C)	+1(C)	Delay	Encoded Image
+1(C)	-1(L)	+1(C)	+1(C)	-1(L)	+1(C)	-1(L)	Delay	Encoded Image
-1(L)	+1(C)	+1(C)	+1(C)	+1(C)	-1(L)	-1(L)	Delay	Encoded Image
+1(C)	+1(C)	-1(L)	+1(C)	-1(L)	-1(L)	+1(C)	Delay	Encoded Image

**Figure 3.12** The scheme of Hadamard-8 matrix that was applied in this study.

The simulated images of pCASL and te-pCASL MRI for the same TI and labeling duration were compared with each other. The SNR of te-pCASL MRI was defined as the ratio of average decoded images to the temporal stdv (tStdv) of decoded images. In the SNR calculation of pCASL MRI, subtraction images were divided into eight groups, and then four subtraction images in each group were averaged. Afterwards, the tStdv of eight average subtraction images was calculated, and the SNR was estimated.

### *Graphical User Interface*

A graphical user interface (GUI) was designed in MATLAB for showing the longitudinal magnetization changes of each sub-boli in te-pCASL in time. Hadamard size, the sub-boli labeling duration times, TI, ATT, TTT and CBF were defined by the user. Also, the estimated values of sub-boli, encoded and decoded images were shown in the "Table" part of the GUI. Additionally, the longitudinal changes of each defined sub-boli were shown over time as a graph at the lower section of the GUI. In one example, the parameters were set as, the sub-boli 1 labeling duration= 30 ms, sub-boli 2 labeling duration= 40 ms, sub-boli 3 labeling duration= 50 ms, TI=100 ms, ATT= 100 ms, TTT = 150 ms,  $f=0.01$  ms,  $\alpha= 0.85$ . Figure 3.13 shows the scheme of te-pCASL for these parameters

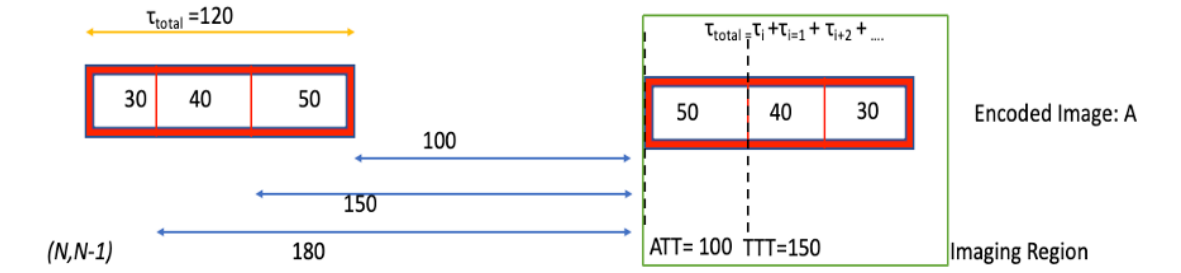


**Figure 3.13** The scheme of te-pCASL for Hadamard size 4.

The design of the GUI is shown in Figure 3.14. This GUI enabled a more convenient visualization of the longitudinal magnetization calculation of sub-boli in MATLAB.

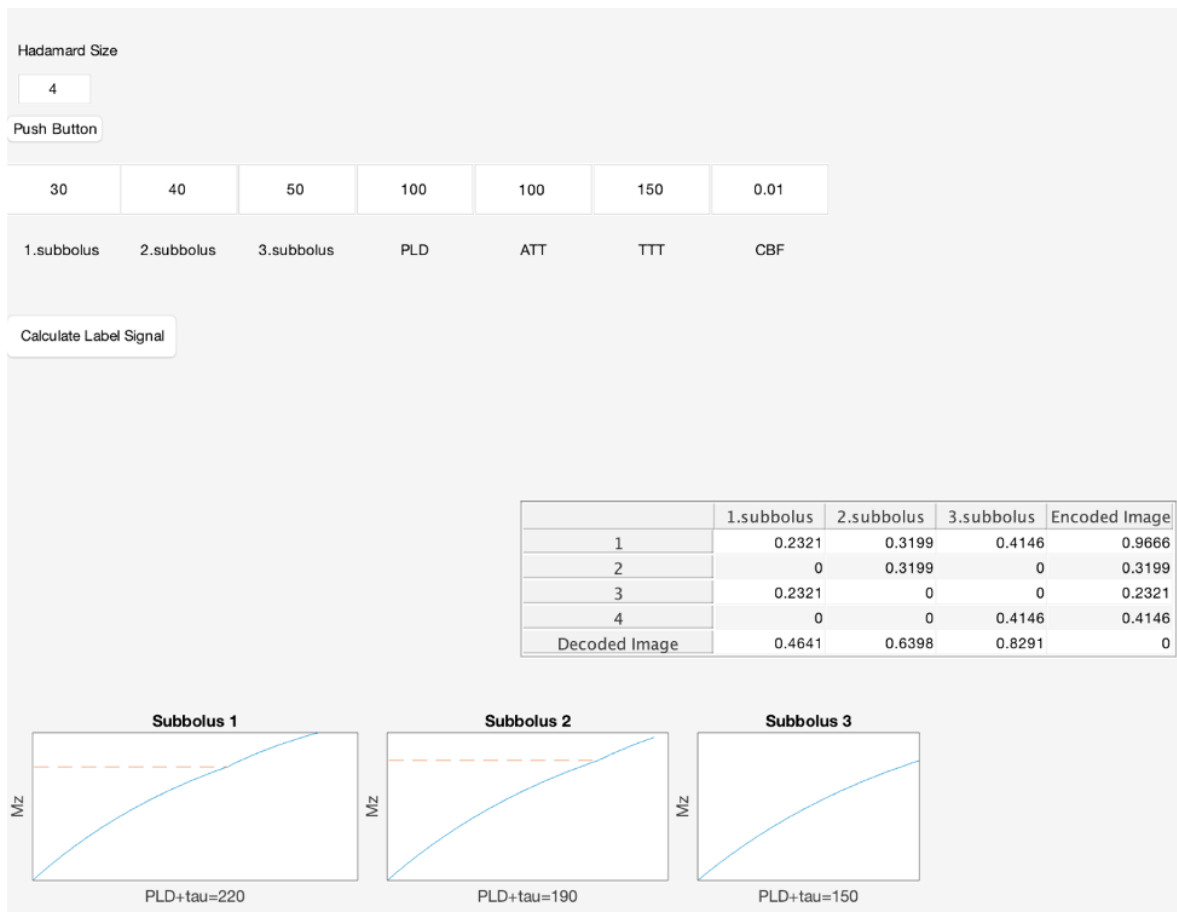


**Figure 3.14** The GUI of te-pCASL.

### *Data acquisition of traditional pCASL MRI and te-pCASL MRI*

One healthy subject was scanned on a Philips 3T Achieva-TX scanner with a 32-channel head coil at the Leiden University Medical Center (LUMC), The Netherlands. The volunteer underwent two scanning sessions on the same scanner.  $T_1w$  images,  $M_0$  images, te-pCASL MR with Hadamard matrix of order 8 and multi-TI traditional pCASL MR images were acquired. In the first scan, the labeling durations of the individual sub-boli were 1175 ms, 683 ms, 482 ms, 374 ms, 305 ms, 257 ms, 224 ms, and TI was 500ms. Eight separate pCASL MR images were acquired at multi-TIs corresponding to the labeling duration and TI of each individual block in te-pCASL technique. Nineteen slices were acquired. BGS inversion pulses were applied at 2330

ms and 3580 ms in the acquisition of te-pCASL MRI. On the other hand, BGS in the pCASL MR was applied at 2330 ms and 3580 ms for only one experiment having 2325 ms TI and 1175 ms labeling duration, whereas 2 auto BGS were applied at the rest of TIs. In the second scan, the labeling durations of the individual sub-boli were 1800 ms, 600 ms, 400 ms, 300 ms, 200 ms, 175 ms and TI was 125 ms. For this experiment, 17 slices were acquired. BGS was applied at 1900 and 3400 ms in the Hadamard scheme and in the pCASL MRI which were acquired at 1800 ms TI with 1800 ms labeling duration. In the rest of pCASL MRI experiments, BGS was not applied. The imaging parameters were single-shot EPI, EPI factor: 31, SENSE: R=2.5, no vascular crushing, excitation flip angle:  $90^\circ$ , and FOV:  $240 \times 240 \times 133 \text{ mm}^3$ . In both scanning sessions, encoded images were repeated eight times whereas control and label images were repeated 32 times.

In addition to these datasets, 12 separate te-pCASL experiments were carried out using a Philips 3T scanner with a 32-channel head coil at LUMC. The imaging parameters were set as, single-shot EPI, EPI factor: 31, SENSE: R=2.3, no vascular crushing, excitation flip angle:  $90^\circ$ , FOV:  $240 \times 240 \times 95 \text{ mm}^3$ , and TR/TE: 4500/14 ms and Hadamard-8 matrix. The labeling durations of the individual te-pCASL sub-boli were 1800/600/400/300/200/150/150ms, and TI was 200ms. For BGS, global (non-selective) hyperbolic secant inversion pulses were used, and selective FOCI inversion pulses were used during labeling. BGS inversion pulses were applied at 1014 ms and 2923.6 ms. Optimal time points of BGS inversion pulses were determined automatically by the scanner console. In the first experiment, the full Hadamard scheme was acquired as normal. In experiments from 2<sup>th</sup> to 8<sup>th</sup>, the labeling RF pulses were only enabled for each single sub-boli with selective BGS at a time. In the 9<sup>th</sup> experiment, labeling RF pulse was applied for a single sub-boli 3 with global BGS. In the 10<sup>th</sup> and 11<sup>th</sup> experiments, selective and global BGS were applied separately without applying any labeling RF pulse at any block. In the 12<sup>th</sup> experiment, RF pulses were applied for a single sub-boli 3 of interleaved Hadamard-8 matrix with selective BGS. Figure 3.15 shows the schematic of the MR experiments performed at LUMC.

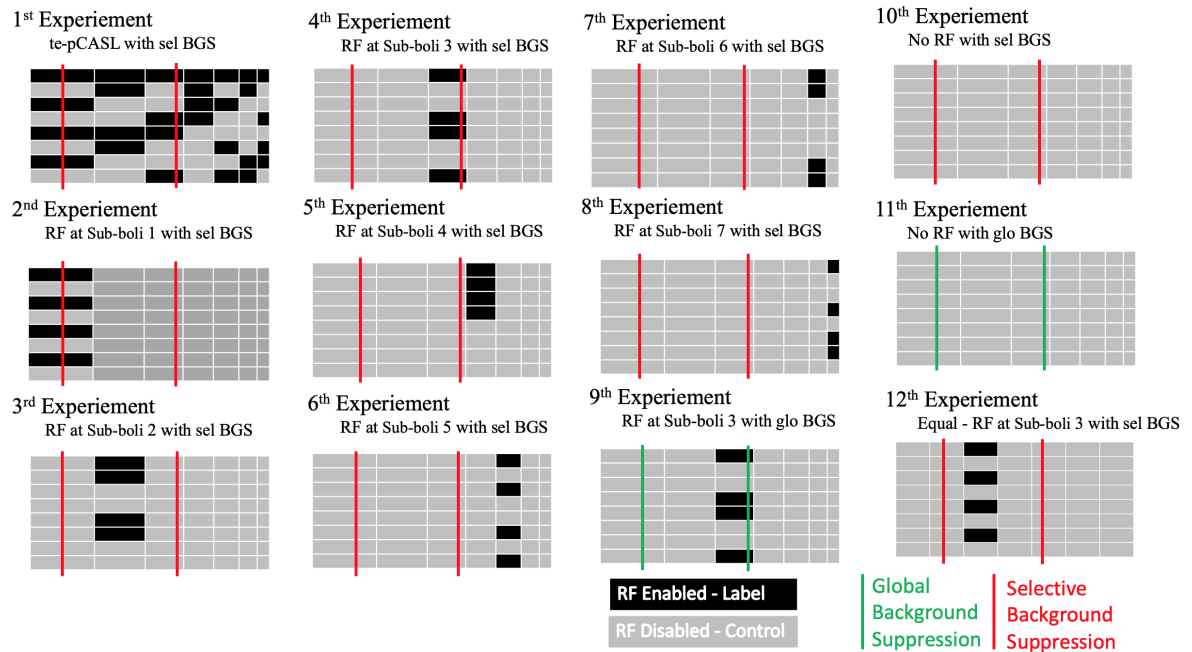


Figure 3.15 The schematic of the MRI experiments performed at LUMC.

### *Analysis*

Data analysis was performed in MATLAB. All traditional pCASL MRI and te-pCASL MRI were masked using M0 images to exclude out-of-brain tissues. Perfusion-weighted and tStdv images were calculated for all acquired data. In te-pCASL MRI, tStdv of eight repeated decoded images were calculated. On the other hand, 32 repeated subtraction pCASL images were divided into eight groups, and then subtraction images in each group were averaged. Afterwards, tStdv of four average subtraction images was calculated. Since signal fluctuations can be seen as positive or negative, the tStdv images are more helpful than perfusion-weighted images to detect and quantify signal fluctuations.

te-pCASL MRI and pCASL MRI datasets from the first two scanning sessions were statistically compared. Firstly, the  $T_{1w}$  image of the volunteer was segmented using SPM to generate a GM mask. Also, a vessels mask was generated by averaging

the perfusion-weighted images at early TIs. Figure 3.16 shows the generated GM and vessels masks of the volunteer.

These generated masks and tStdv images were converted into a single 3D volume in NIFTI format in MATLAB and coregistered onto T<sub>1</sub>w MRI. After transformation matrix was obtained by normalizing T<sub>1</sub>w image into MNI152 brain atlas using FSL, it was applied to register coregistered masks and tStdv images onto the MNI152 brain atlas. Afterwards, GM and vessels masks were converted to binary masks, and the tStdv images were multiplied with the masks to get tStdv values in GM and vessels regions. Then, tStdv values in GM and arterial vessels of pCASL and te-pCASL images were compared by applying a paired t-test ( $P < 0.05$ ). A Bland-Altman test were applied to compare pCASL and te-pCASL MRI values.

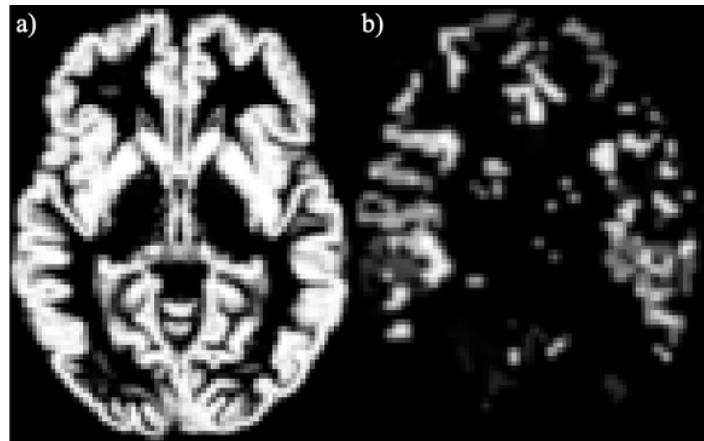


**Figure 3.16** The GM and vessels masks of the volunteer.

## 4. RESULTS

### 4.1 ASL MRI with LL readout data

#### 4.1.1 Comparison of Subjects' NPT scores

PD-MCI patients had significantly lower ACE-R ( $P < 0.001$ ), MMSE ( $P < 0.001$ ), MOCA ( $P < 0.001$ ), and SDMT ( $P < 0.001$ ) test scores as compared with the other two groups, while HC and PD-CN groups were similar in all neuropsychological measures. However, PD-MCI patients had higher WCST ( $P = 0.009$ ) and Stroop ( $P = 0.02$ ) test scores than the other two groups. There were not any statistically significant differences between JLO scores ( $P = 0.07$ ) among the three groups (Table 4.1).

**Table 4.1**

Comparison of neuropsychological test scores and the *P* values calculated by a Kruskal-Wallis test followed by post-hoc Dunn-Sidak tests.

Test	Subjects	Mean $\pm$ stdv	<i>P</i>	PD-CN, <i>P</i>	PD-MCI, <i>P</i>
<b>ACE-R</b>	HC	94.13 $\pm$ 3.40		0.13	0.001
	PD-CN	89.81 $\pm$ 3.75	0.001		0.001
	PD-MCI	77.07 $\pm$ 5.68			
<b>MMSE</b>	HC	30.00 $\pm$ 0.00		0.07	0.001
	PD-CN	29.38 $\pm$ 0.80	0.001		0.002
	PD-MCI	28.15 $\pm$ 1.41			
<b>MOCA</b>	HC	26.69 $\pm$ 1.93		0.34	0.001
	PD-CN	25.20 $\pm$ 2.33	0.001		0.003
	PD-MCI	22.37 $\pm$ 2.52			
<b>WCST PR (%)</b>	HC	16.40 $\pm$ 7.10		0.65	0.013
	PD-CN	19.16 $\pm$ 9.14	0.009		0.068
	PD-MCI	25.73 $\pm$ 10.84			
<b>STROOP IT (sec)</b>	HC	46.33 $\pm$ 17.07		0.40	0.02
	PD-CN	54.69 $\pm$ 17.25	0.02		0.22
	PD-MCI	73.63 $\pm$ 41.19			
<b>JLO</b>	HC	25.13 $\pm$ 2.61		0.83	0.10
	PD-CN	24.04 $\pm$ 3.86	0.07		0.19
	PD-MCI	21.22 $\pm$ 5.77			
<b>SDMT</b>	HC	37.14 $\pm$ 14.80		0.61	0.002
	PD-CN	31.27 $\pm$ 10.19	0.001		0.01
	PD-MCI	22.07 $\pm$ 9.91			

\* $P < 0.006$  and  $P < 0.05$  were considered as statistically significant for Kruskal-Wallis test and Dunn-Sidak test, respectively. PR: perseverative responses; IT: interference time

Comparison between the neuropsychological scores of two genetic groups (MAPT H1/H1 haplotype versus H1/H2 haplotype) did not reveal any statistically significant differences in the all-PD or in the PD-MCI groups (Table 4.2).

**Table 4.2**

Comparisons of neuropsychological test scores between two genetic groups according to MAPT haplotypes within the all-PD group and the PD-MCI group, and the P values calculated by a Mann-Whitney U test.

Subjects	Tests	Genotype		P
		<i>MAPT</i> H1/H1 (mean $\pm$ stdv)	<i>MAPT</i> H1/H2 (mean $\pm$ stdv)	
All-PD (n=33 vs. n=19)	ACE-R	84.42 $\pm$ 7.83	81.58 $\pm$ 8.39	0.20
	MMSE	28.94 $\pm$ 1.32	28.37 $\pm$ 1.21	0.054
	MOCA	24.37 $\pm$ 2.56	22.58 $\pm$ 3.00	0.07
	WCST	20.50 $\pm$ 10.70	24.68 $\pm$ 10.22	0.11
	PR(%)			
	STROOP	69.33 $\pm$ 35.24	57.68 $\pm$ 27.32	0.30
	IT (sec)			
	JLO	23.12 $\pm$ 5.09	21.63 $\pm$ 5.21	0.25
	SDMT	27.82 $\pm$ 11.88	23.84 $\pm$ 8.91	0.29
	PD-MCI (n=15 vs. n=11)	ACE-R	77.93 $\pm$ 6.12	75.64 $\pm$ 5.22
MMSE		28.20 $\pm$ 1.52	27.91 $\pm$ 1.22	0.61
MOCA		23.17 $\pm$ 2.37	21.00 $\pm$ 2.31	0.07
WCST		23.79 $\pm$ 11.61	27.85 $\pm$ 10.45	0.28
PR(%)				
STROOP		87.07 $\pm$ 43.03	59.64 $\pm$ 33.26	0.08
IT (sec)				
JLO		21.13 $\pm$ 6.21	21.09 $\pm$ 5.65	0.96
SDMT	21.27 $\pm$ 10.67	21.73 $\pm$ 8.32	0.60	

\*P<0.006 and P<0.05 were considered as statistically significant for Kruskal-Wallis test and Dunn-Sidak test, respectively. PR: perseverative responses; IT: interference time

#### 4.1.2 Voxel-Based Comparison of Subject Groups

Figure 4.1 shows M0 (a), CBF (b), arterial blood volume (aBV) (c) and ATT (d) maps estimated for an example HC. The ranges of M0, CBF, aBV, and ATT values were [0, 40000], [0, 80], [0, 2.5] and [0, 1.5], respectively. The aliasing artifact that is visible in the M0 map was alleviated in CBF, aBV, and ATT maps as a result of fitting the data into the general kinetic model. In aBV maps, the blood vessels had higher signal intensity than the surrounding tissue.

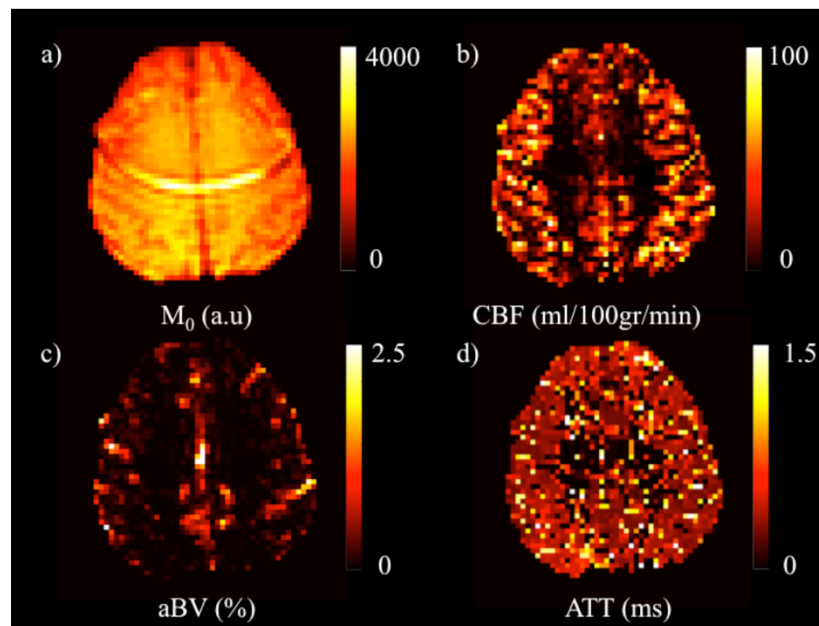


**Figure 4.1**  $M_0$  (a), CBF (b), aBV (c), and ATT (d) maps for a healthy control subject.

There were statistically significant voxel-wise differences between CBF maps of HC, PD-CN, and PD-MCI groups in the left superior parietal lobule (SPL) of the FPN, two separate areas in the right SPL of DAN, and right postcentral gyrus (postCG) of the sensorimotor network (SMN) (Table 4.3). Post hoc comparisons revealed that CBF values of PD-CN patients were significantly lower than those of HC participants only in an area centered in crus I of the left cerebellum posterior lobe extending into crus II ( $P < 0.001$ ), which are both the components of FPN according to the cerebellar parcellation described by Buckner et al. [90].

PD-MCI versus HC revealed some areas of decreased perfusion, including the same cerebellar region observed in the PD-CN versus HC comparison ( $P = 0.002$ ). The largest area of hypoperfusion in PD-MCI was centered in the Brodmann area (BA) 7 of the right SPL, which was a part of DAN, extending downward into the angular gyrus of the inferior parietal lobule (IPL), posteriorly into the superior occipital gyrus, and anteriorly into the postCG and precentral gyrus ( $P < 0.001$ ). Another smaller BA7 region in the opposite hemisphere, corresponding to FPN, extending into the precuneus and IPL, also had hypoperfusion ( $P < 0.001$ ). Additionally, hypoperfusion

at the SMN in the left anterior-Rolandic area centered in BA6 extending backward into the primary motor cortex (M1) ( $P = 0.033$ ), the VN in the right inferior occipital gyrus centered in BA19 extending into the fusiform gyrus (FG) ( $P = 0.009$ ), the right PCC area centered in BA31 of the precuneus corresponding to DMN ( $P = 0.003$ ), and the bilateral primary VN centered in the right cuneus ( $P = 0.012$ ) were observed in PD-MCI. Finally, the comparison of PD-CN versus PD-MCI revealed a single area of significant hypoperfusion in PD-MCI group in the right posterior-Rolandic area, centered in S1 of the postCG, which was a part of the SMN ( $P = 0.018$ ). These statistically significantly different brain regions are depicted in Figure 4.2.

The classification algorithms revealed an overall accuracy of 92.60% (sensitivity = 93% and specificity = 93%) for classifying PD-MCI and HC using a fine kNN algorithm. Additionally, the classification accuracy of all-PD versus HC was 91.50% (sensitivity = 98%, specificity = 85%) using a quadratic SVM algorithm. On the other hand, PD-CN and HC groups were classified with a lower accuracy of 80.80% (sensitivity = 88%, specificity = 73%) using a logistic regression algorithm.

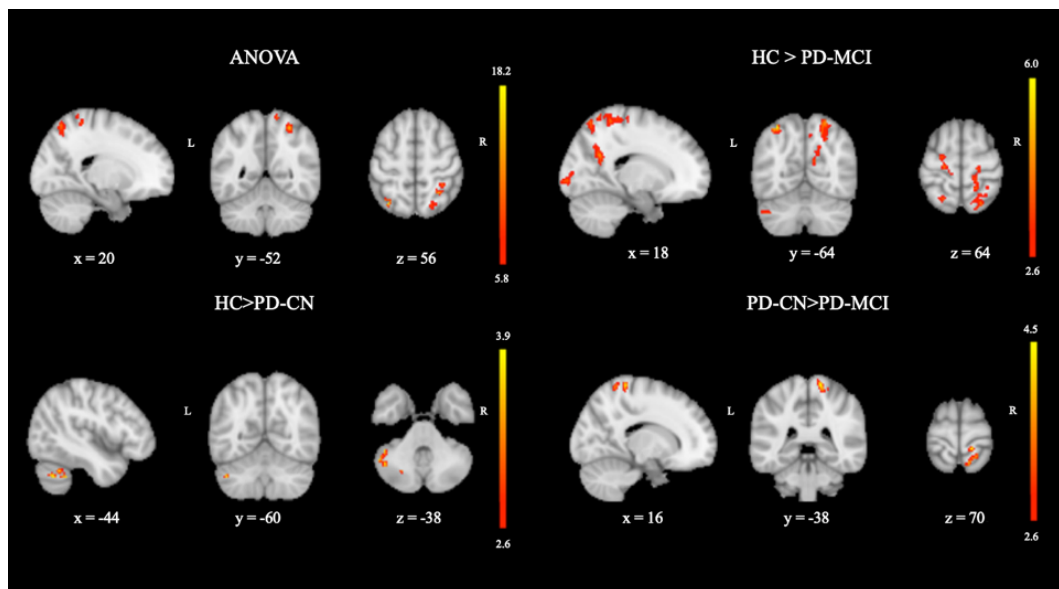


**Figure 4.2** The areas showing statistically significant differences of CBF between HC, PD-CN, and PD-MCI observed with ANOVA and post hoc comparisons. The color bars represent peak F value in the ANOVA and t values in the pair-wise comparisons. R: Right, L: Left.

**Table 4.3**

The regions of CBF differences between groups detected by one-way ANOVA, with cluster forming  $P < 0.005$ , cluster level FWE corrected threshold at  $P < 0.05$ , and cluster size of 50 voxels.

Test Type	Comparison	Core Region	Cluster Size(1x1x1 mm <sup>3</sup> )	Cluster P(FWE corr.)	Peak MNI coordinate(x y z)	Networks
ANOVA	Main group effect	*Left superior parietal lobule (L BA7)	94	0.043	-32 -64 56	FPN
		*Right superior parietal lobule (R BA7)	119	0.011	30 -52 56	DAN
		*Right superior parietal lobule (R BA7)	117	0.012	20 -66 60	DAN
		*Right postcentral gyrus (R S1)	105	0.023	16 -38 68	SMN
Post hoc tests	HC>PD-CN	Left cerebellum posterior lobe (L Crus I)	269	0.001	-44 -60 -38	FPN
	HC>PD-MCI	Left cerebellum posterior lobe (L Crus I)	232	0.002	-44 -62 -36	FPN
		*Left superior parietal lobule (L BA7)	346	0.001	-32 -64 56	FPN
		Left precentral gyrus (L BA6)	144	0.033	-20 -22 64	SMN
		*Right superior parietal lobule (L BA7)	907	0.001	30 -52 56	DAN
		*Right inferior occipital gyrus (R BA19)	179	0.009	32 -82 -8	VN
		*Right precuneus (R BA23)	211	0.003	18 -56 26	DMN
		*Right cuneus (R BA17)	171	0.012	14 -102 -2	VN
		PD-CN>PD-MCI	*Right postcentral gyrus (R S1)	161	0.018	16 -38 70

\*: Regions that constituted posterior hypoperfusion.

### 4.1.3 Comparison of Subjects Groups with Different genotypes

When two MAPT haplotypes (H1/H1 versus H1/H2) of all-PD patients were compared, the former group had significantly decreased CBF values compared with the latter in a large area in the bilateral cerebellum, centered in the right crus I, but also in the left crus I and Lobule IV ( $P < 0.001$ ), which corresponded to FPN; a left middle temporal gyrus (MTG) of VN and the anterior hub of FPN ( $P = 0.001$ ); and three smaller clusters in the right visual network areas, including the inferior occipital gyrus ( $P = 0.025$ ), lingual gyrus ( $P = 0.018$ ), and calcarine ( $P = 0.030$ ) (Table 4.4). When only the PD-MCI group was considered, the same comparison revealed decreased perfusion in the MAPT H1/H1 subgroup in nine areas. Six of these nine were in bilateral visual areas, including the primary visual cortex (V1), the extrastriate visual areas, and downstream visual areas, such as FG. There were two cerebellar areas in the right hemisphere, at the anterior lobe (lobule IX), and the posterior lobe (crus I), which were the cerebellar components of DMN or FPN, respectively. Finally, a posterior medial region comprising the precuneus, centered in the BA31 of PCC, was detected ( $P = 0.007$ ), which corresponded to DMN. The regions of lower CBF in all-PD and PD-MCI patients with the MAPT H1/H1 haplotype are shown in Figure 4.3.

**Table 4.4**

The regions of CBF differences between two groups within all-PD and PD-MCI groups according to MAPT haplotypes at cluster-forming  $P < 0.005$ , cluster-level FWE-corrected threshold of  $P < 0.05$ , and cluster size of 50 voxels.

Comparison	Region	Cluster Size (1x1x1 mm3)	Cluster P (FWE corr.)	Peak MNI coordinate (x y x)	Network
<b>All-PD</b> <b>MAPT H1/H2 (n=19)</b> > <b>H1/H1 (n=33)</b>	Bilateral cerebellum posterior lobe (R CrusI)	1144	0.001	36 -50 -34	FPN
	*Left middle occipital gyrus (L BA19)	250	0.001	-48 -63 8	VN
	*Right inferior occipital gyrus (R BA19)	145	0.025	40 -82 -8	VN
	*Right lingual gyrus (R BA17)	154	0.018	4 -96 -4	VN
	*Right calcarine (R BA18)	140	0.030	6 -82 12	VN
<b>PD-MCI</b> <b>MAPT H1/H2 (n=11)</b> > <b>H1/H1 (n=15)</b>	*Left precuneus (L BA31)	161	0.007	-8 -62 30	DMN
	*Left middle temporal gyrus (L BA37)	224	0.001	-50 -60 0	DAN
	*Left lingual gyrus (L BA18)	174	0.004	-90	VN
	*Left inferior occipital gyrus (L BA18)	473	0.001	-128	VN
	*Right fusiform gyrus (L BA37)	236	0.001	50 -56 -20	VN
	*Right lingual gyrus (R BA18)	201	0.001	22 -86 -6	VN
	*Right cuneus (R BA17)	218	0.001	6 -72 20	VN
	Right cerebellum anterior lobe (R lobule IX)	170	0.005	16 -38 -42	DMN
	Right cerebellum posterior lobe (R Crus I)	134	0.021	36 -50 -36	FPN

\*: Regions that constituted posterior hypoperfusion.

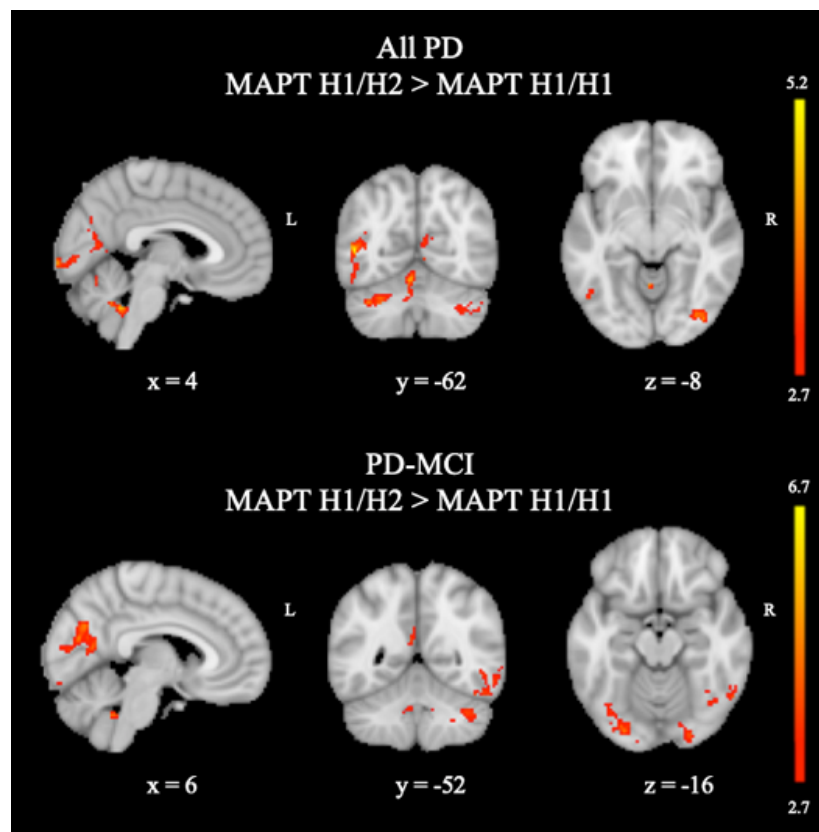


**Figure 4.3** The areas showing significantly lower CBF in MAPT H1/H1 haplotype compared to H1/H2 haplotype, including the all-PD or the PD-MCI patients, respectively. The color bars represent t values. R: Right, L: Left.

#### 4.1.4 Comparison of Subjects Groups in General cognitive, executive, and visual domains

When all three groups of participants were collapsed together, and divided into tertiles according to z scores in the general cognitive domain, the comparison of the lowest tertile group with the highest tertile group revealed significantly lower CBF changes in LP in two areas, which were a right superior parietal area, centered in angular gyrus and extending into superior parietal lobe (SPL) ( $P < 0.001$ ); and a left superior parietal area, covering SPL, centered in Broadman area (BA)7 ( $P = 0.037$ ) (Table 4.5). These regions had symmetric hypoperfusion in posterior parietal cortex (PPC) corresponding to the on the border zone of posterior hubs of the bilateral FPN and DAN. When only two PD groups were combined, the same analysis did not show any significant differ-

ences between HP and LP. The same analysis was also repeated with the executive domain z scores. The differences observed were again in the combined three groups, but not in combined two patient groups. Executive domain LP showed significantly lower CBF values as compared to HP in three areas, which were right middle frontal gyrus (MFG), centered in BA9 ( $P=0.042$ ); left inferior parietal lobule (IPL), centered in BA39-angular gyrus (AG) and extending into supramarginal gyrus (BA40-SMG) ( $P=0.008$ ); and left SPL, centered in BA7 ( $P=0.049$ ).

Figure 4.4 shows the statistically significantly different brain regions between HP and LP groups in general cognitive and executive domains. The comparison in the executive domain revealed two posterior areas in the left hemisphere. The first one was with the peak coordinates in the border zone of DAN and FPN and the second one was with peak coordinates in the border zone of FPN, and default mode network (DMN). There were not any statistically significant CBF differences between HP (4 HC, 7 PD-CN, 12 PD-MCI) and LP (6 HC, 10 PD-CN, 7 PD-MCI) z score subgroups of the visual domain either in all subjects or in PD patients.

**Table 4.5**

Regions of CBF differences between two groups defined based on composite z-scores in general cognitive domain and executive domain within the entire subject group, separately.

Domain	Comparison	Region	Cluster Size (1x1x1 mm <sup>3</sup> )	Cluster P (FWE corr.)	Peak MNI Coordinate (x y z)	Network
<b>General Cognitive Domain</b>	HP > LP*	Right superior parietal lobule	331	0.001	38 -56 50	DAN-FPN
		Left superior parietal lobule	135	0.037	-20 -54 66	FPN-DAN
<b>Executive Domain</b>	HP>LP**	Right middle frontal gyrus	132	0.042	30 40 26	FPN
		Left inferior parietal lobule	176	0.008	-60 -52 36	DMN-FPN
		Left superior parietal lobule	128	0.049	-18 -68 44	DAN-FPN

\*The composite z-scores are the average of the z-converted raw scores of ACE-R, MMSE and MOCA. Median of the composite z-scores: - 1.22. LP: lowest tertile, HP: highest tertile. \*\*The composite z-scores are the average of the z-converted raw scores of WCST percentage of perseverative responses score and Stroop interference duration score. Median of the composite z-scores: 0.56. LP: highest tertile, HP: lowest tertile.

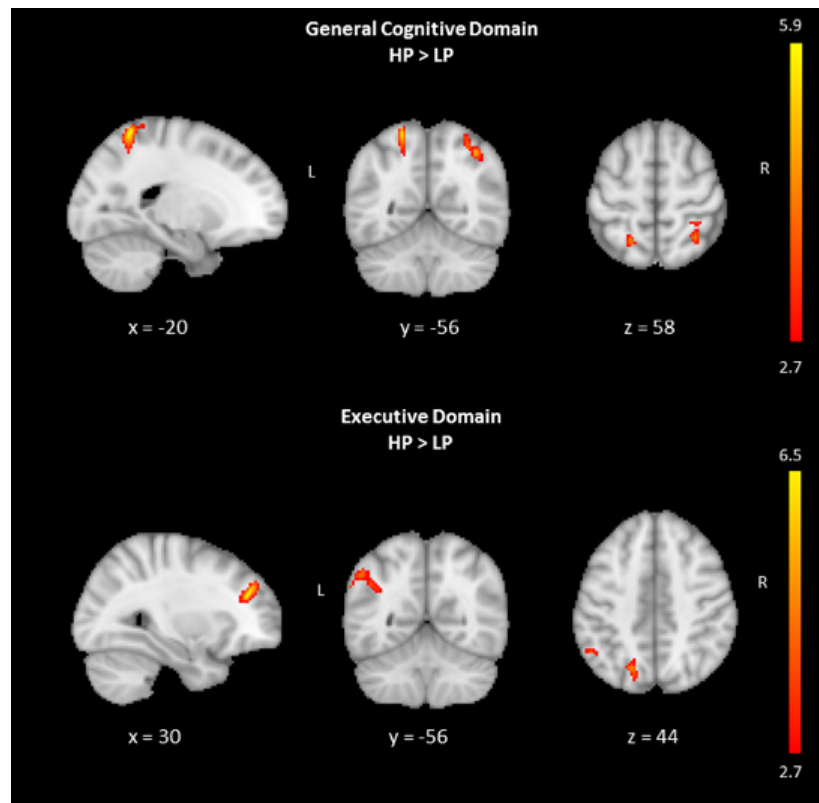
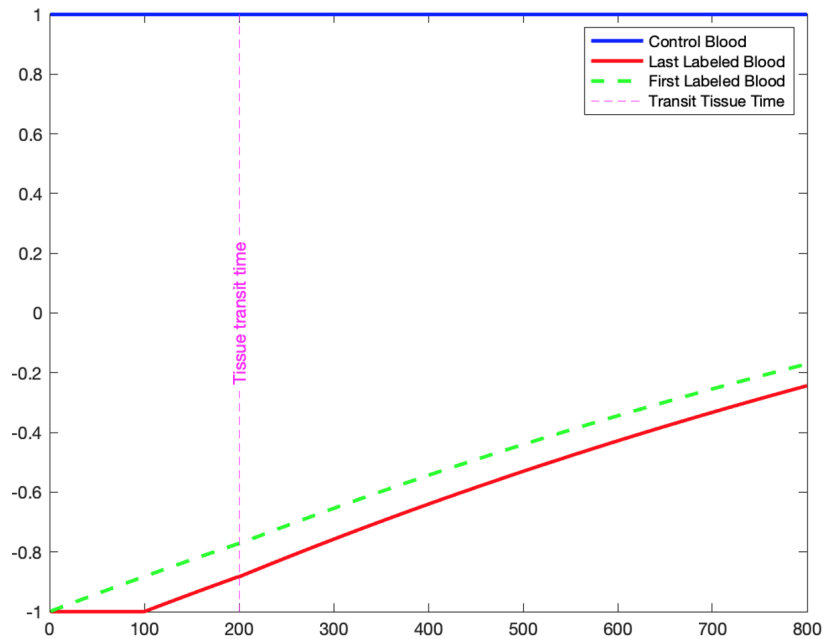


**Figure 4.4** Regions of significant CBF decreases of LP compared to HP in all of the participants according to general cognitive and executive domain scores. The color bars represent t values. R: Right, L: Left.

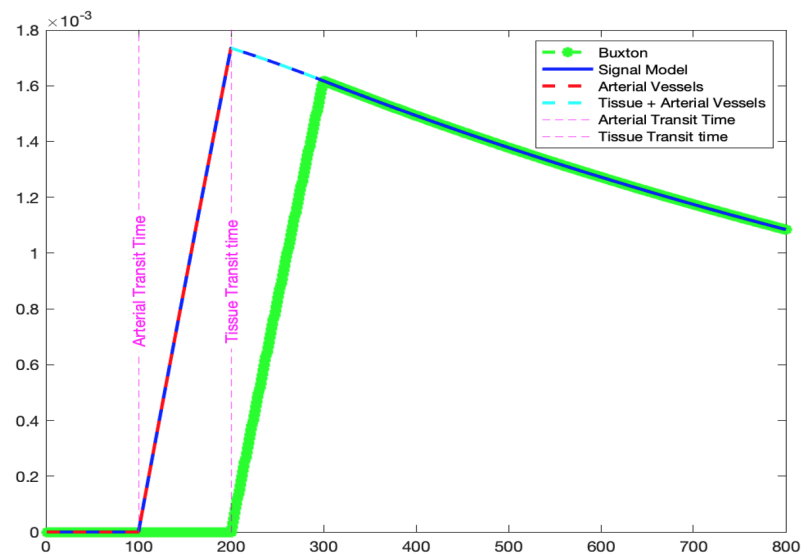
## 4.2 te-pCASL MRI data

### 4.2.1 Simulation

Figure 4.5 shows the changes of longitudinal magnetization of unlabeled (blue), first (green) and last (red) labeled protons within the blood during labeling duration for control experiment. Longitudinal magnetization didn't change during the control experiment, whereas inverted protons were returning back to the equilibrium by decaying with  $T_1$  of the blood and tissue, respectively. Additionally, Figure 4.6 shows the ASL signal based on the general kinetic model [7] and two compartment model in time.



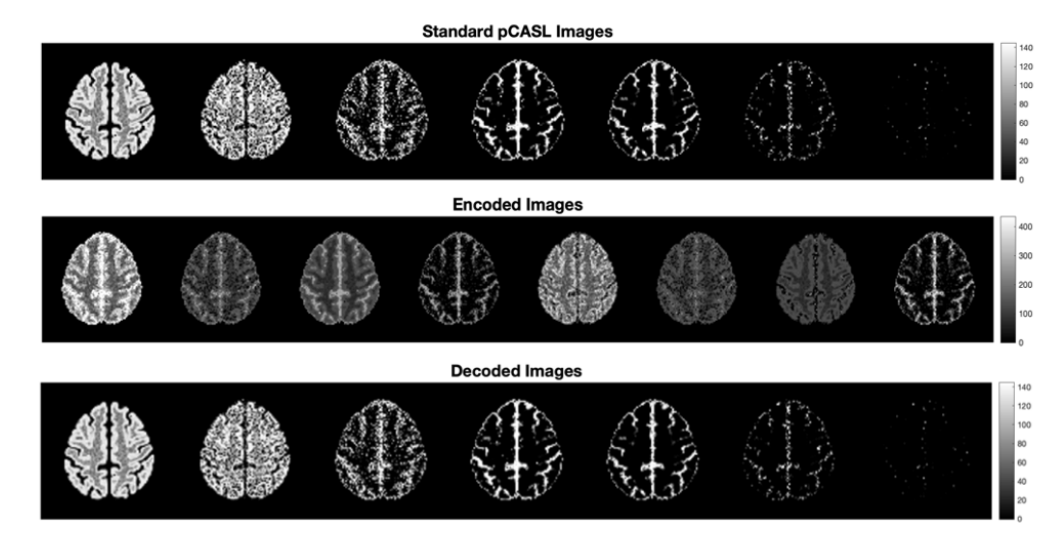
**Figure 4.5** The changes of longitudinal magnetization of control protons, first and last labeled protons versus time.



**Figure 4.6** The curves of ASL signal of general kinetic model and two compartment model versus time.

Figure 4.7 shows the simulated perfusion-weighted images of pCASL MRI, and encoded and perfusion-weighted images of te-pCASL MRI. Perfusion-weighted images of pCASL MRI were subtracted from that of te-pCASL at same TIs. Subtracted

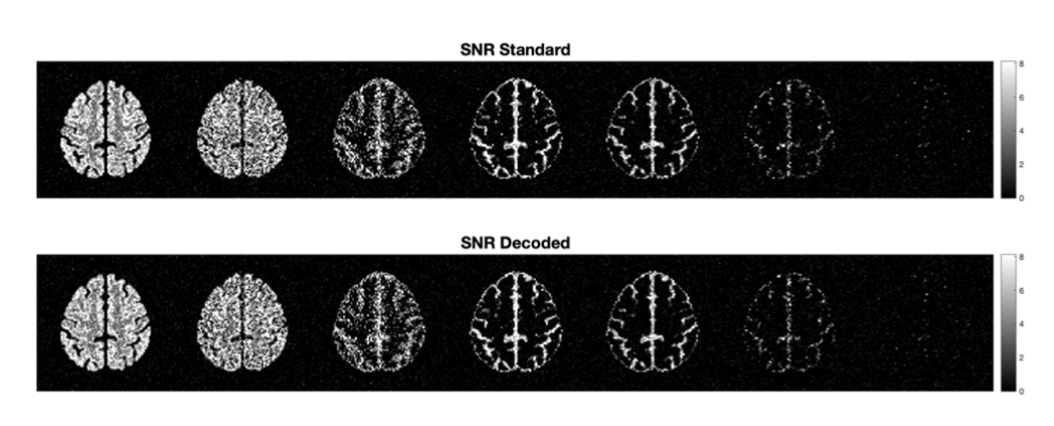
perfusion-weighted images were just noisy differences (Figure 4.8). Figure 4.9 shows that the SNR images of simulated standard and decoded images were the same.



**Figure 4.7** The perfusion-weighted images of pCASL (a), encoded (b) and perfusion-weighted (c) images of te-pCASL.



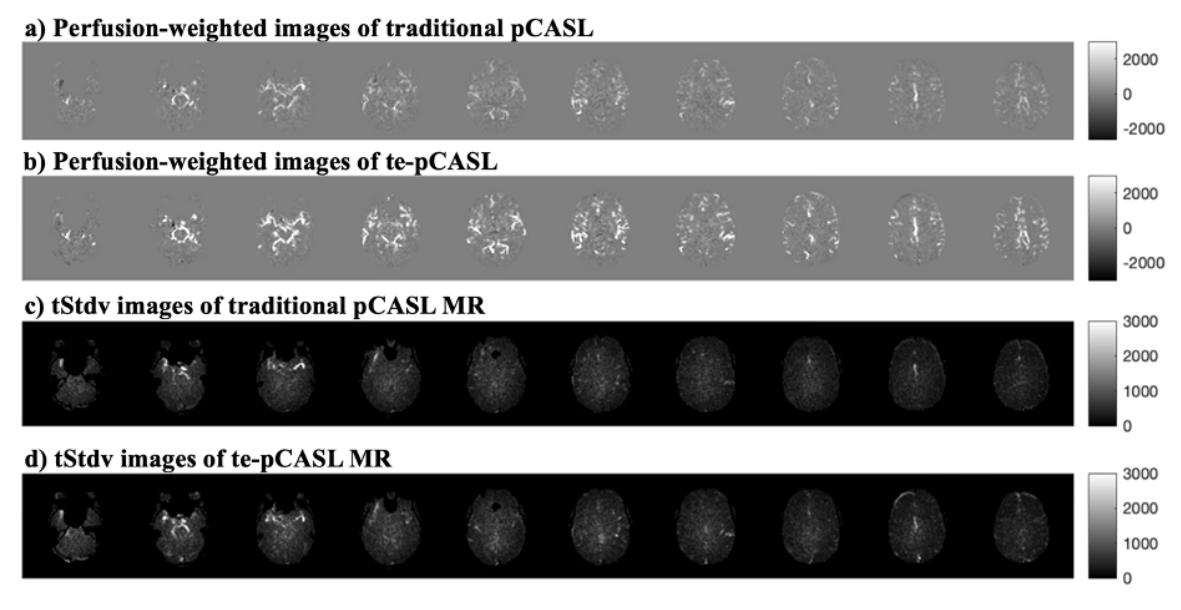
**Figure 4.8** Subtraction of perfusion-weighted images of simulated pCASL and te-pCASL MRI.



**Figure 4.9** The SNR images of simulated pCASL and te-pCASL MRI.

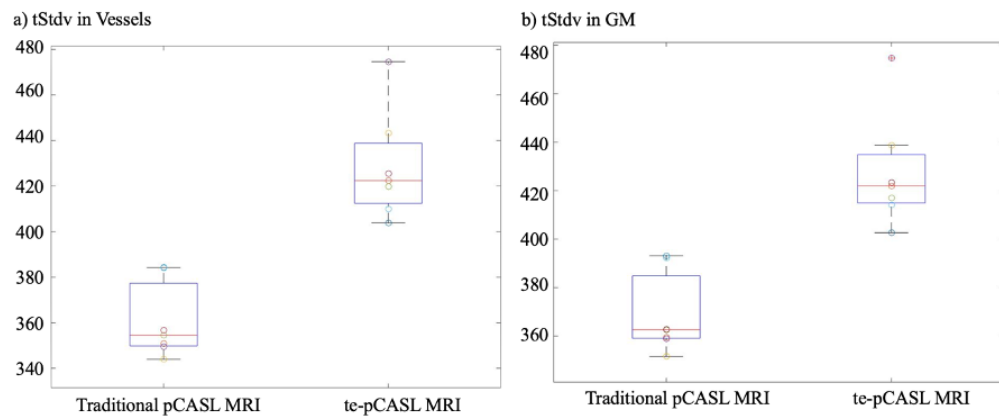
#### 4.2.2 Comparison of te-pCASL and traditional pCASL datasets

Figure 4.10 shows perfusion-weighted (a, b) and tStdv (c, d) images of te-pCASL with BGS and pCASL with BGS for 10 slices at 724 ms TI with 257 ms labeling duration.



**Figure 4.10** Perfusion-weighted images of te-pCASL (a) and pCASL (b) and tStdv images of te-pCASL (c) and pCASL (d) from first single scan session.

There were statistically significant differences between the tStdv values in GM ( $P=0.005$ ) and vessels ( $P=0.003$ ) regions of pCASL and te-pCASL images for the same one slice at different TIs (Figure 4.11).



**Figure 4.11** Box-plot showing mean tStdv of vessels (a) and GM (b) values of pCASL and te-pCASL images.

Figure 4.12 demonstrates perfusion-weighted (a, b) and tStdv (c, d) images of te-pCASL with BGS and pCASL without BGS for 10 slices at 1220 ms TI with 600 ms labeling duration. Unlike te-pCASL, perfusion-weighted images of pCASL had more negative intensities. Additionally, tStdv images of pCASL had high intensities.

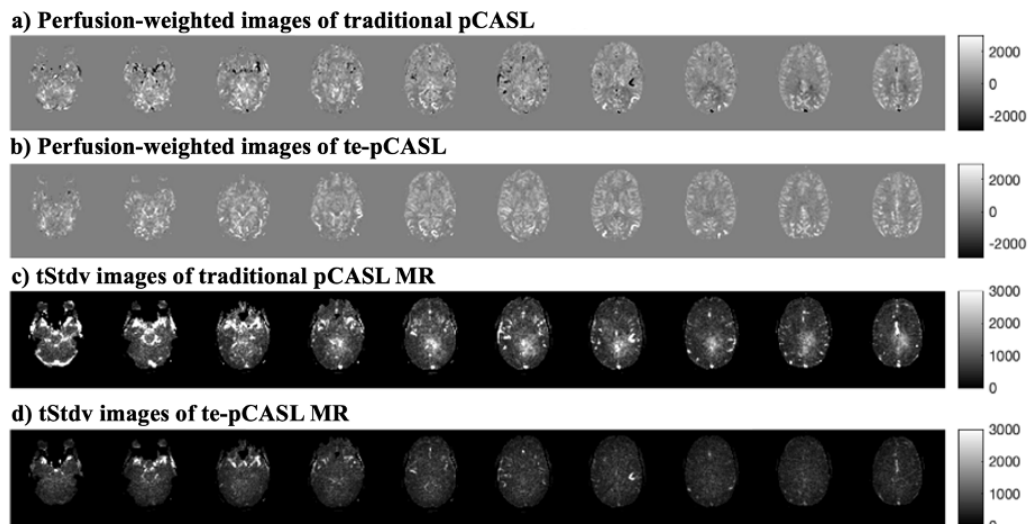


**Figure 4.12** Perfusion-weighted images of te-pCASL (a) and pCASL (b) and tStdv images of te-pCASL (c) and pCASL (d) from second single scan session.

Despite the high signal difference, there were no statistically significant differ-

ences between the tStdv values in GM and vessels regions of pCASL ( $P= 0.008$ ) and te-pCASL ( $P=0.009$ ) for the same slice at different TIs (Figure 4.13).

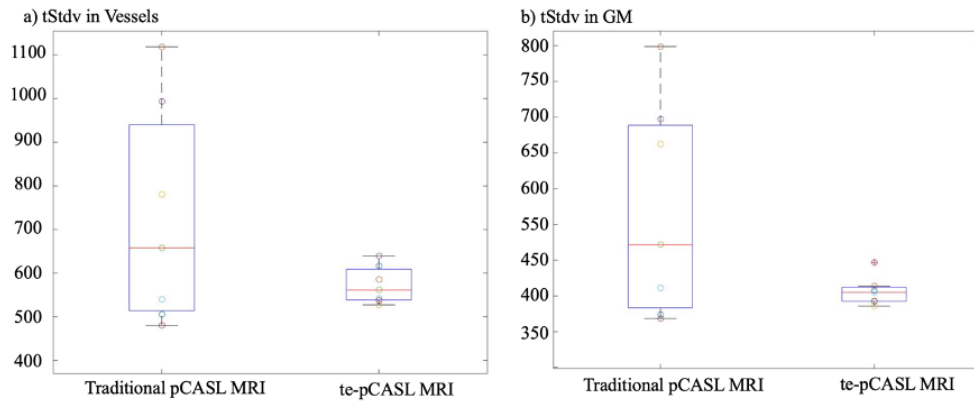


**Figure 4.13** Box-plot showing mean tStdv of vessels (a) and GM (b) values of pCASL and te-pCASL images.

Figure 4.14 shows the mean differences of tStdv values of pCASL and te-pCASL in GM and vessels regions acquired from first (Figure 36-a, b) and second (Figure 36-c, d) scan sessions. The mean differences were close to zero, and there were no outliers.

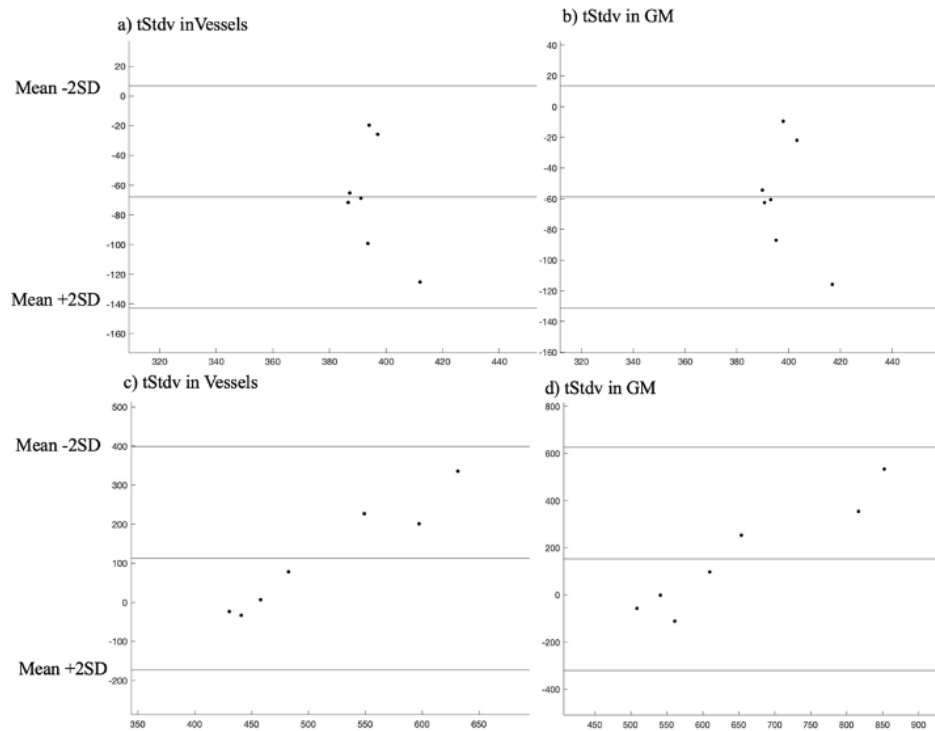


**Figure 4.14** The Bland-Altman test results for the differences of the mean tStdv values of pCASL and te-pCASL in GM and vessels regions acquired from first (a, b) and second (c, d) scan sessions.

### 4.2.3 Shine-through effect

Figure 4.15 shows the perfusion-weighted images of fully acquired te-pCASL at different TIs for 11 slices. The shine-through effect was seen as negative or positive intensities in perfusion-weighted images at different TIs and slices. Also, tStdv images of fully acquired te-pCASL had high intensities in the pixels where the shine-through artifact was seen (Figure 4.16).

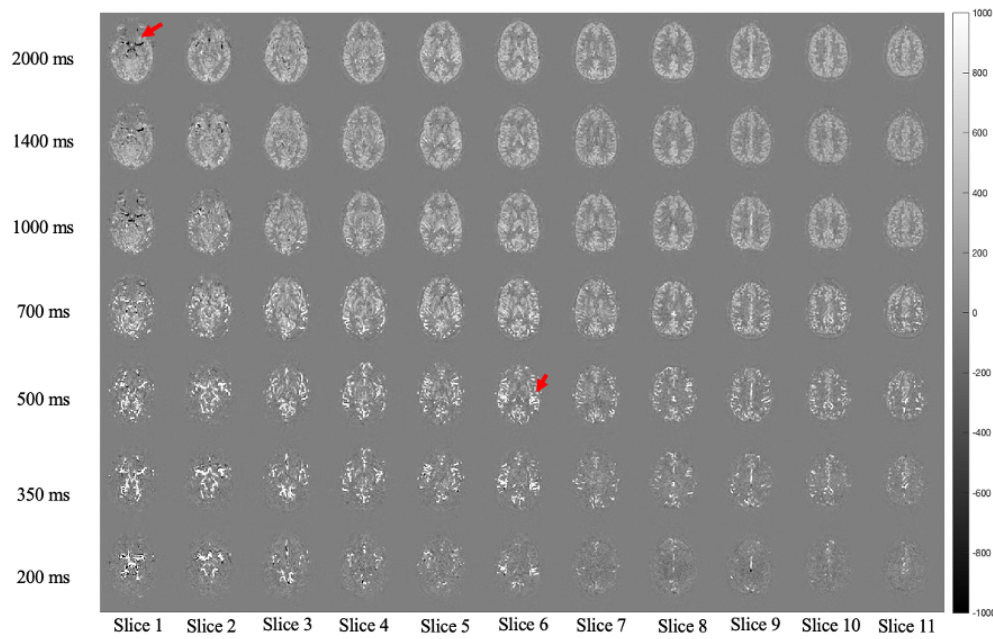


**Figure 4.15** Perfusion-weighted images of fully acquired te-pCASL images.

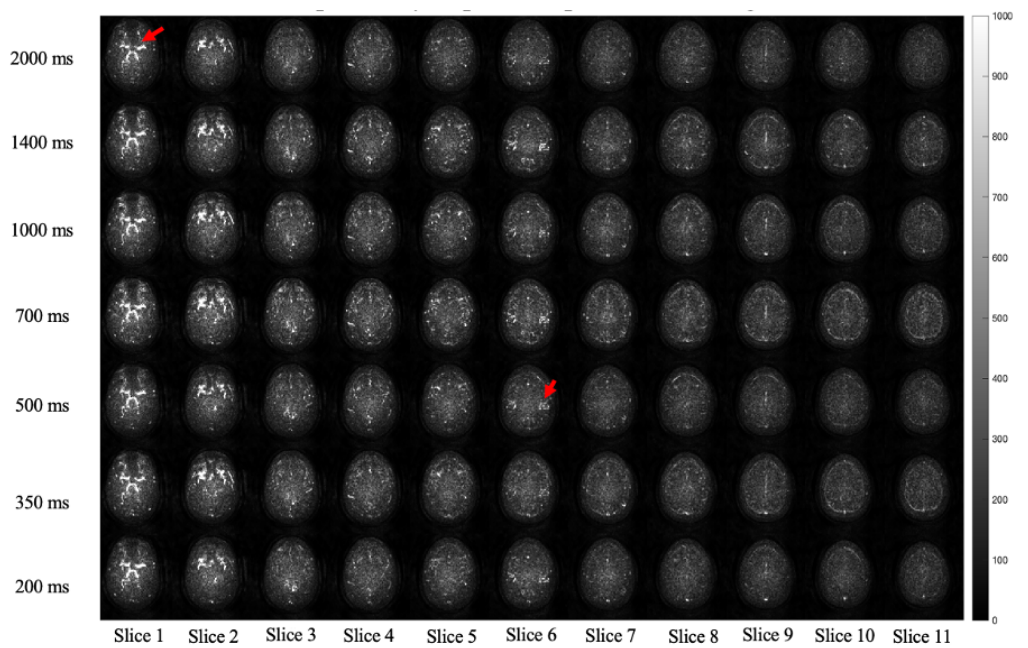


**Figure 4.16** tStdv images of fully acquired te-pCASL dataset.

Figure 4.17 shows the perfusion-weighted images of fully acquired data from te-pCASL (first column) and seven separate te-pCASL experiments where labeling RF

pulse was on for only one individual sub-boli at a time. When labeling RF pulse was applied in individual sub-boli in time, the shine-through artifact was also seen in the disabled sub-boli.

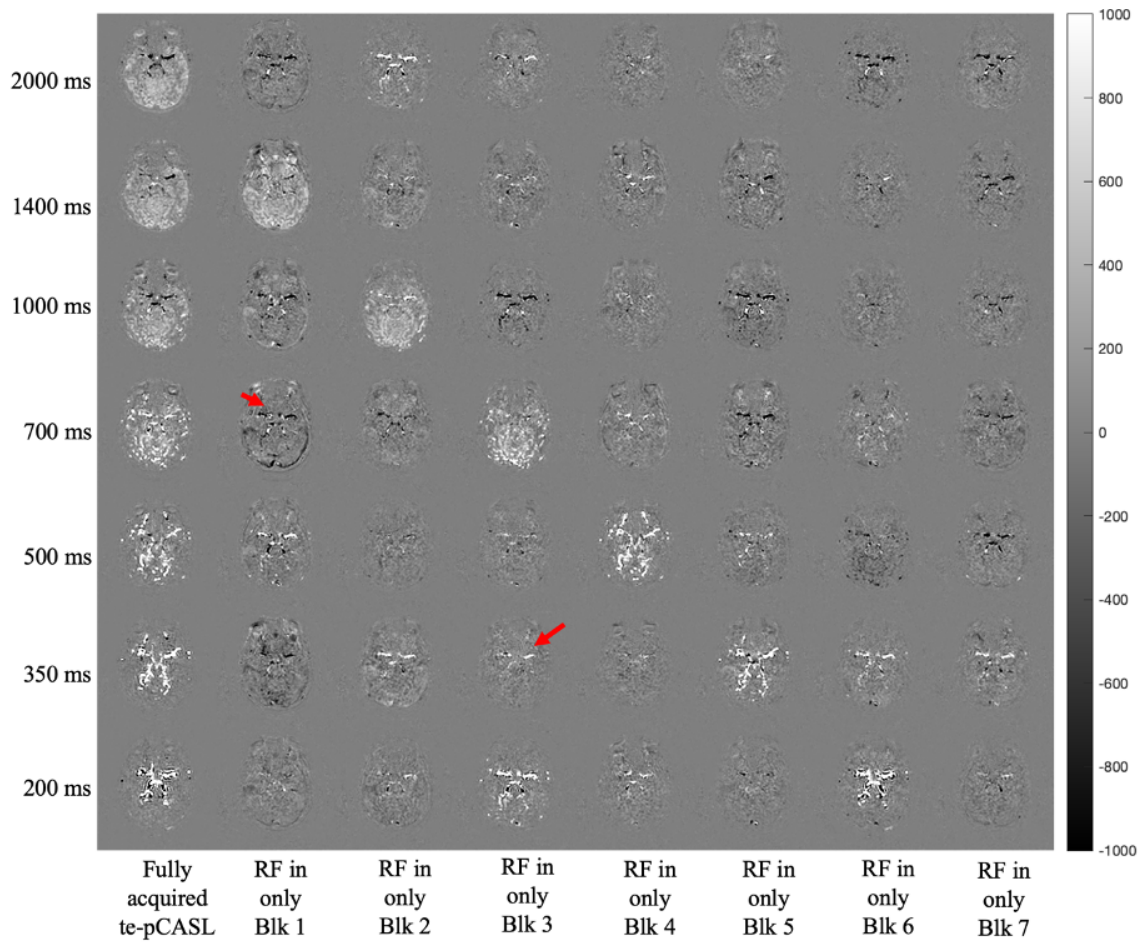


**Figure 4.17** Perfusion-weighted images of fully acquired te-pCASL and seven separate te-pCASL experiments for one slice.

In perfusion-weighted images of te-pCASL when labeling RF pulse was on at only sub-boli 3 with selective BGS (Figure 4.18 - a), some pixels had high ASL signal. Interestingly, these same pixels were negative with global BGS (Figure 4.18 - a - II). In te-pCASL with interleaved Hadamard-8, high ASL signal was seen at longest TI when labeling RF pulse was applied at only sub-boli 3 with selective BGS (Figure 4.18 - a - III). tStdv images with global BGS were seen unsimilar to the te-pCASL with selective with and without interleaved Hadamard (Figure 4.18 - b).

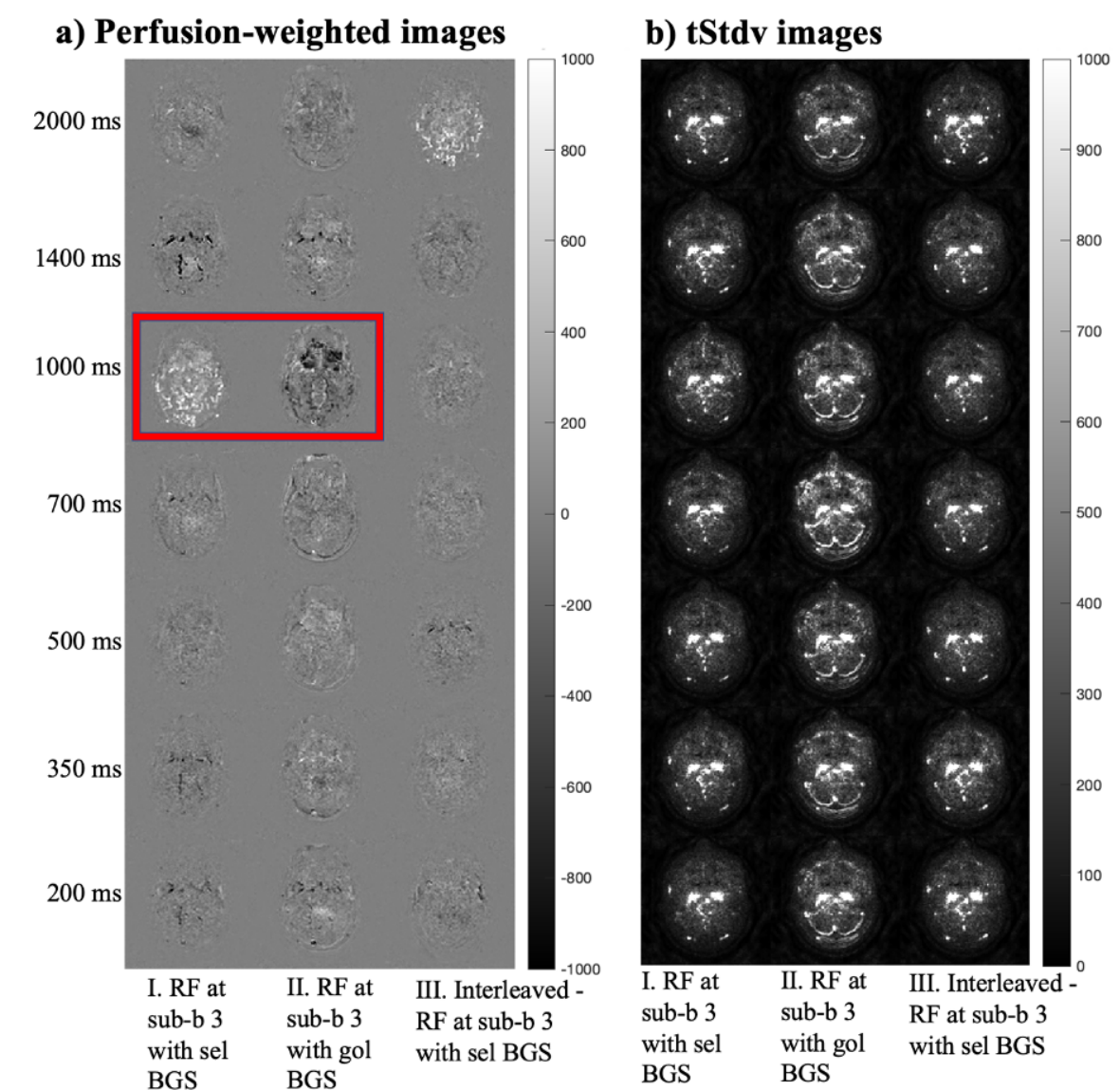


**Figure 4.18** Perfusion-weighted images of te-pCASL with RF at only sub-boli 3 with either selective BGS (a) or global BGS (b) and of interleaved te-pCASL with RF at only sub-boli 3 with selective BGS (c).

Figure 4.19 shows the perfusion-weighted (a) and tStdv (b) images of te-pCASL when labeling RF pulse was off at any sub-boli with either selective or global BGS. ASL signal was also seen in both techniques without any RF labeling. Additionally, tStdv images had more high values in te-pCASL with global BGS than with selective BGS.

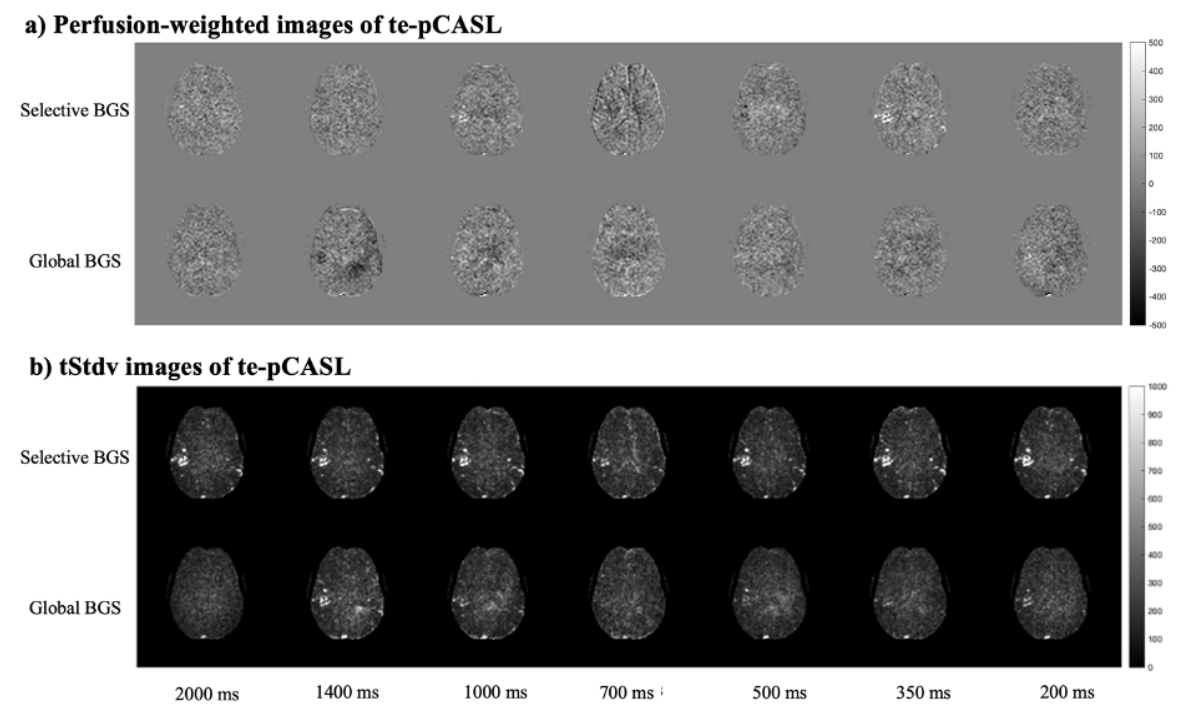


**Figure 4.19** Perfusion-weighted (a) and tStdv images (b) of te-pCASL without any labeling RF pulses with either selective or global BGS for one slice.

## 5. DISCUSSION

Multi-TI ASL MRI is an advantageous approach that provides accurate CBF estimations by taking into account the blood arrival time. Two multi-TI ASL MRI techniques are ASL MRI with LL readout and te-pCASL MRI. ASL-MRI with LL readout requires a complex model to accurately estimate CBF. On the other hand, te-pCASL MRI has a shine-through effect, which might cause errors in CBF estimation. This thesis study aimed to accurately estimate CBF based on ASL-MRI with LL readout and apply it to underpin perfusion deficits in PD, in addition to explore the potential reason of the shine through effect in the te-pCASL MRI. In the first part of the thesis, a software program was developed to calculate CBF maps from ASL MRI with LL readout. Afterwards, the brain perfusion deficits reflecting both mild cognitive impairment state and possessing a risky genetic state in PD were investigated using ASL-MRI with LL readout. The major finding of the first part of the thesis is the PH both in PD-MCI as compared with HC and genetically risky PD with MAPT H1/H1 haplotype as compared with non-risky PD with MAPT H1/H2 haplotype. In the second part of the thesis, the possible reasons of shine-through effect in te-pCASL MRI were assessed using simulations and in-vivo data. Based on the theoretical model, pCASL and te-pCASL MRI resulted in similar ASL signals. On the other hand, our experimental results indicated that the shine-through effect could be caused by the application of selective BGS inversion pulses.

PH, which is decreased blood flow at the posterior part of the brain, was first reported in a SPECT study, which found significant bilateral occipital and posterior parietal regional CBF reductions in nondemented PD patients compared with HCs [93]. Subsequently, several ASL-MRI studies reported PH as a correlate of cognitive impairment in PD [50, 51, 56]. The Kamagata study was the first to use the PH term in an ASL-MRI study, and they reported significantly different perfusion at a posterior area, more or less corresponding to VN, between healthy control subjects, PD-CN, and PDD, the lowest being in the PDD group and highest in the PD-CN

group [51]. Later, posterior cortical hypoperfusion related to cognitive decline in PD has been reported at the posterior POC, precuneus, cuneus, and posterior cingulate [50,56]. Moreover, LeHeron et al. compared the ASL-perfusion pattern in PDD with AD and the HC groups, and analysis of absolute blood flow showed no significant differences between AD and PDD, but each group, compared with the HC group, revealed an overlapping, posterior pattern of hypoperfusion, including PCC, precuneus, and occipital regions [55]. Similarly, comparison among PD-MCI, PD-CN, and HC in our study revealed that PH was composed of spots of areas located mostly in the lateral and medial parietooccipital cortices, corresponding to posterior components of DAN, FPN, DMN, and VN. In addition to the previous findings, an area in the right postCG, with peak coordinates in primary somatosensory cortex belonging to SMN, was the only discriminating area in the PD-MCI and PD-CN comparison of the present study. Moreover, cerebellar crus I hypoperfusion, which is at a component of FPN [90], was the only discriminating area in the PD-CN and HC comparison of this study. However, Fernandez-Seara et al. reported somewhat more widespread hypoperfusion in nondemented PD patients as compared with HC in areas including PFC (BA 8 and 9), PMd, pre-SMA, PPC, and POC [52].

This study revealed decreased perfusion in H1 homozygous PD patients. Interestingly, although comparison of the neuropsychological test scores did not reveal any differences between the two genetic PD groups, the CBF comparisons between the H1/H1 and H1/H2 subgroups of both all-PD and PD-MCI revealed cortical areas that were almost entirely parts of the VN, while the only exceptions were the PCC of DMN and posterior MTG of DAN in the PD-MCI group. One cerebellar (crus I) area in the all-PD and two cerebellar areas (crus I and lobule IX) in the PD-MCI groups were components of FPN and DMN, respectively [90]. The lack of performance difference in the JLO test may stem from the relative easiness of this task. Nombela et al. reported that the H1/H1 carrier of newly diagnosed PD patients had much worse performance compared with noncarriers in the difficult items of a visuospatial task, and that their parietal cortices and caudate nuclei were hypoactive [71].

PD-MCI and all-PD groups were successfully differentiated from HC based on

the voxel intensity differences within the PH regions using machine learning algorithms. However, the accuracy was lower for the differentiation of PD-CN and HC, because PD-CN patients did not exhibit posterior hypoperfusion. Several machine learning algorithms were used for classifications, because no single classifier works best across all possible problems [94]. Additionally, class imbalance problem was solved using the SMOTE technique, which has been reported to perform better than simple oversampling [95].

In addition to PH, other biomarkers of cognitive decline in PD have been reported in the literature. rs-fMRI studies in PD patients with cognitive deficits have consistently reported altered functional connectivity patterns in DMN, FPN, and SN [96–100]. The Jia et al. study that was previously referred to also found decreased functional connectivity at the precuneus in addition to reduced perfusion in PD-MCI patients in comparison with PD-CN and HC groups [56]. Moreover, structural brain MRI analysis revealed significant GM atrophy in the left caudate in PD-CN and PD-MCI subjects in comparison to HC [56] and white matter impairment at the prefrontal and fronto-parieto-temporal areas in cognitively impaired PD patients [101–103]. Although, GM atrophy has been reported along with occipital and posterior parietal hypoperfusion in PDD [103], other studies revealed presence of regional hypoperfusion patterns without detectable GM atrophy in MCI [104]. Moreover, hypoperfusion has been reported to precede structural alterations in MCI [103, 104]. On the other hand, when present, GM atrophy might confound regional perfusion measurements, and it might be necessary to correct for the partial volume effects [105].

The simulation model built in the second part of the thesis study assumed a two compartment model, including arterial vessels and the tissue compartment. The general kinetic model that is commonly employed has three major assumptions, which are, a) before TTT, there are no labeled protons within the imaging volume. After TTT, labeled spins arrive uniformly at the tissue, b) TTT and ATT can be considered as equal, because labelled spins are retained within the microvasculature and exchanges rapidly between vessels and brain tissues and c) the longitudinal magnetization of the labeled spins decays with the  $T_1$  of blood. Our simulation model wasn't dependent on

these three assumptions and provided a detailed assessment of longitudinal magnetization over time. Additionally, the simulation results showed that ASL signal of pCASL and te-pCASL MRI were the same, except for the noise levels, which means that these two techniques are theoretically identical.

The noise characteristics of pCASL and te-pCASL were statistically compared to show the presence of shine-through effect. te-pCASL had higher noise in GM and arterial regions than pCASL upon BGS application in both techniques. In another data set, BGS was applied in te-pCASL whereas it was not applied in pCASL acquisitions except for one. It was observed that noise levels of pCASL and te-pCASL were not statistically significantly different even in GM and vessels regions even if the patterns of both images looked different. Also, the Bland Altman test results indicated that there were no significant differences between pCASL and te-pCASL MRI. Unsuppressed pCASL MRI had residual signals, which might help with decreasing noise difference between these two techniques. Without the residual signals, te-pCASL MRI could have high signal fluctuations not seen in pCASL MRI even if these techniques are supposed to be same.

After it was found that there could be signal differences between pCASL and te-pCASL, some mechanisms have been devised to understand the origin of the shine-through effect. Firstly, the effect of Hadamard labeling scheme has been assessed by switching the label and control situations and imperfect interleaved labeling. The shine-through artifact was seen in the disabled sub-boli when labeling RF pulses were applied in individual sub-boli in time, but also, surprisingly, in the images without any labeling at any sub-boli. Also, the noise patterns were seen as similar in te-pCASL images with and without equally interleaved labeling durations. As a result, we concluded that the Hadamard labeling scheme did not have an effect on the appearance of the shine-through artifact.

Another mechanism assessed in the second part of this thesis was the BGS scheme in te-pCASL MRI. Several studies have been conducted to suppress the background signal by applying extra inversion pulses during the labeling of spins within

the blood to reduce physiological noise while improving the ASL image quality [11, 29,30,32]. In one study, PCASL with BGS had higher sensitivity than PASL without BGS for detecting CBF differences between MCI and elderly HCs [106]. On the other hand, Garcia et al. [31] measured the efficiency of the inversion pulses in-vivo or on an appropriate phantom and found out that BGS reduced the ASL signal, while also decreasing the standard deviation of the signal. Therefore, it was reported that the loss of signal due to BGS inversion pulses should be taken into account for the CBF calculations. As a result, no more than two inversion BGS pulses were used in the experiments performed at Leiden University Medical Center that were utilized in this study.

Additionally, the noise levels were lower in te-pCASL with global BGS than that with selective BGS when labeling RF pulses were off at all sub-boli. The global BGS pulses invert all of the spins regardless of location. Inverted inflowing spins below the labeling region could lead to lower signal fluctuations in the arteries if these are not labeled and then arrive at imaging volume before the readout. On the other hand, the selective BGS pulses are applied above the labeling region and the spins of the protons flowing to the labeling region will remain untouched until the application of the labeling RF pulse. When labeling is stopped at the end of the labeling duration, the untouched inflowing spins could lead to high signal in the arteries if these arrive to imaging volume before readout. Even though te-pCASL needs the use of BGS with slice-selective pulses to prevent mixing of inverted and un-inverted spins [34], it can be said that shine-through effect could be caused by the application of these selective BGS inversion pulses.

In literature, global BGS inversion pulses have been employed in pCASL MRI because they also attenuate the inflow spins of the protons below the labeling region due to multiple inversions [29,107]. Also, our results showed that the signal fluctuations in arterial vessels was lower in pCASL with global BGS. However, beside the low signal fluctuations, the ASL signal was also low because all the signals were attenuated. These results were in good agreement with the literature. This finding supported that global BGS is not compatible with long labeling durations because of interleaving with the

labeling pulses [34].

This thesis had some limitations. Some artifacts were observable in multi ASL MRI techniques. One was the susceptibility artifact resulting from the EPI readout, which caused a signal loss in some regions of the CBF maps in ASL MRI with LL readout [108]. Also, an aliasing artifact resulting from imperfect SENSE reconstruction was visible in raw ASL MR with LL readout images although the patients were scanned after they took medication in order to prevent motion artifacts resulting from involuntary movements, which might have resulted in higher CBF estimations [109]. Better coil sensitivity map estimation might be useful to alleviate this artifact. These artifacts were more pronounced in ASL-MRI with LL readout even if EPI readout and SENSE reconstruction were also applied in te-pCASL. Although binary GM masks were used in this study, a better approach could be to use partial volume effects correction to more accurately estimate and compare pure GM perfusion [105]. In the first part of this thesis, due to the limited coverage of LL readout, acquisitions were repeated three times, which caused a long scan time and high SAR. Additionally, the registration of CBF maps onto the MNI152 template might have resulted in slight regional shifts, because the MNI template includes a normalized brain atlas based on healthy, young subjects. Future studies will explore the effect of using age-matched brain atlases for registration [110]. Moreover, this study employed a standard univariate analysis of ASL-MRI data, and a multivariate analysis resulting in disease specific spatial covariance patterns might provide a better assessment of perfusion deficits in PD-MCI [49,111–113]. Additionally, the hypoperfusion pattern differences between genetic subgroups of this study might be partially influenced by apparent differences in gender distribution and motor symptoms. Another limitation was the limited number of subjects in the study population, and ASL-MRI data were only acquired at baseline. Moreover, the consecutive recruitment method used did not result in a clinically overt visual subtype of PD-MCI, and a single measure of visuospatial dysfunction turned out to be a limitation of the study. The chosen measure to define the visuospatial dysfunction (JLO score) was not different among the three groups. However, both the executive measures (WCST percentage of perseverative responses and Stroop interference time) were significantly worse in the PD-MCI group than in the HC. Future

studies need to be designed where the CBF will be measured longitudinally in a larger patient cohort to see whether indeed a "dual syndrome" could be parsed out of the PH pattern: the involvement of dopaminergic-dependent, top-down executive control networks, such as FPN and DAN, which is nonprogressive, and the involvement of nondopaminergic, mnemonic, and visuospatial networks, such as DMN and VN, which is expected to progressively lead to dementia. Additionally, more than one measure (and possibly more-difficult measures) of visuospatial skills and recruitment of a visual PD-MCI patient group, whose performance will be below a specific SD for the visuospatial domain assessment, would be necessary for such an assessment.

In the second part of this thesis, a limited number of pCASL and te-pCASL MRI scans with same TI and same labeling duration were compared in terms of noise characteristics. In the future, more data will be included for this comparison. Also, deep learning models could be applied for detection of shine-through effect after more te-pCASL data is available in the future. Another limitation was BGS timing to acquire high quality images. One study showed that BGS timing was automatically optimized by using the  $T_1$  spectrum, obtained from M0 scans [114]. To solve signal fluctuations caused by BGS, subject-specific background suppression could be applied in te-pCASL. Additionally, one study combined te-pCASL labeling with a LL readout and a simultaneous multi-slice (SMS) acquisition and reported that this combination could enable acquisition of multi-TI ASL MRI with a whole-brain coverage in a time-efficient manner and calculation of CBF, ATT, as well as arterial blood volume maps [115]. This study has brought a new perspective. In the future, the combination of LL readout and te-pCASL with optimized BGS could be tried and images could be analyzed by using the in-house program, written within the scope of this thesis, for ASL MRI with LL readout, which could provide to enable shine-through artefact at more multi-TI in a short scan time and more accurate results in perfusion deficits patients with neurodegenerative diseases.

## 6. CONCLUSION

ASL-MRI with LL readout data acquired from PD patients and HC subjects were analyzed using in-house written program within the scope of this thesis. At the end of the analysis, a PH pattern was identified in patients with PD-MCI, and these patients were successfully classified with over 90% accuracy using machine learning algorithms. Moreover, the study indicated that the risky gene carriers, which are homozygous for the H1 haplotype of the MAPT gene, clearly had a visual network hypoperfusion without yet having a detectable visuospatial dysfunction. We concluded that multi-TI ASL MRI with LL readout contributed to the increasing evidence that PH was indeed a marker of cognitive impairment in PD. In the future, a GUI will be developed for merging all the ASL-MRI post-processing and analysis steps and will be made publicly available to enable the clinicians and students to assess the perfusion changes at different functional brain parcellations obtained from resting state fMRI.

Our results indicated that te-pCASL and pCASL techniques theoretically produced the same perfusion-weighted images when using the same TI and labeling duration, although in a more time-efficient manner for te-pCASL. However, the perfusion weighted images of te-pCASL and pCASL MRI often reveal differences, which was not related to Hadamard encoding scheme. We concluded that the application of BGS inversion pulses with slice-selection was better in te-pCASL, but could be a potential reason of shine-through artifact, because selective BGS inverts only the spins above the labeling region.

In conclusion, multi-TI ASL MRI techniques could be useful for the identification of brain disorders. Also, the BGS scheme should be optimized to prevent signal fluctuations in multi-TI ASL MRI.

## 7. APPENDIX A: Publications

### Publications

#### First author

1. Arslan DB, Gurvit H, Genc O, et al. The cerebral blood flow deficits in Parkinson's disease with mild cognitive impairment using arterial spin labeling MRI. J Neural Transm (Vienna). 2020;127(9):1285-1294.

#### Not first author

1. Buz-Yalug B, Arslan DB, Ozturk-Isik E. Prospect of data science and artificial intelligence for patient specific neuroprostheses. Somatosensory Feedback for Neuroprosthetics. Elsevier/Academic Press.

### International Conference Proceedings and Abstracts

#### First author

1. Arslan DB, Gurvit H, Genc O, Kicik A, Eryurek K, Cengiz S, Erdogdu E, Yildirim Z, Tufekcioglu Z, Ulug AM, Bilgic B, Hanagasi H, Demiralp T, Ozturk-Isik E. The perfusion deficits in general cognitive, executive, and visual dysfunction in Parkinson's disease measured by arterial spin labeling MRI. International Society for Magnetic Resonance in Medicine. Vancouver, BC, Canada, 15-20 May, 2021. (poster.)
2. Arslan DB, Gurvit H, Genc O, Kicik A, Eryurek K, Cengiz S, Erdogdu E, Yildirim Z, Tufekcioglu Z, Ulug AM, Bilgic B, Hanagasi H, Demiralp T, Ozturk-Isik E.

- The Cerebral Blood Flow Changes in Parkinson's Disease with Mild Cognitive Impairment Using Arterial Spin Labeling MRI. International Society for Magnetic Resonance in Medicine. Virtual Meeting, August 8-14, 2020. (poster)
3. Arslan DB, Gurvit H, Genc O, Kicik A, Eryurek K, Cengiz S, Erdogdu E, Yildirim Z, Tufekcioglu Z, Ulug AM, Bilgic B, Hanagasi H, Demiralp T, Ozturk-Isik E. Perfusion-Based Biomarkers of Mild Cognitive Impairment in Parkinson's disease with different MAPT haplotypes using Arterial Spin Labeling MRI. International Society for Magnetic Resonance in Medicine. Virtual Meeting, August 8-14, 2020. (poster)
  4. Arslan DB, Yildirim Z, Cengiz S, Kicik A, Erdogdu E, Tufekcioglu Z, Bilgic B, Hangasi H, Ulug AM, Demiralp T, Gurvit IH, Ozturk-Isik E. Cerebral Blood Flow Changes in Different Mapt Genotypes of Parkinson's Disease at Cerebral Cortex Parcellations Obtained from Resting State fMRI. Alzheimer's Association International Conference. Los Angeles, USA, July 14-18, 2019. (poster)
  5. Arslan DB, Cengiz S, Eryurek K, Genc O, Kicik A, Erdogdu E, Tufekcioglu Z, Bilgic B, Hanagasi H, Ulug AM, Gurvit IH, Demiralp T, Ozturk-Isik E. Longitudinal Changes in Cerebral Blood Flow Calculated by Arterial Spin Labeling MRI in Parkinson's Disease. International Society for Magnetic Resonance in Medicine. Montreal, Canada, May 11-16, 2019. (poster)
  6. Arslan DB, Cengiz S, Kicik A, Erdogdu E, Yildirim Z, Tufekcioglu Z, Bilgic B, Hanagasi H, Ulug AM, Demiralp T, Gurvit H, Ozturk-Isik E. The Cerebral Blood Flow Changes of Executive Dysfunction in Parkinson's Disease Measured by Arterial Spin Labeling MRI at Cerebral Cortex Parcellations Obtained from Resting State fMRI. International Society for Magnetic Resonance in Medicine. Montreal, Canada, May 11-16, 2019. ( poster)
  7. Arslan DB, Hatay GH, Cebeci H, Hakyemez B, Ozturk-Isik E. Cerebral Perfusion Measurement of Brain Tumors Using Arterial Spin Labeling MRI Accelerated by Compressed Sensing. European Society of Magnetic Resonance in Medicine and Biology Annual Conference. Barcelona, Spain, October 19-21, 2017. (lightning talk)

8. Arslan DB, Cengiz S, Kicik A, Erdogan E, Buker S, Tufekcioglu Z, Ulug AM, Bilgic B, Hanagasi H, Gurvit H, Demiralp T, Ozturk-Isik E. Association of Arterial Spin Labeling MRI with Neurophysiological Test Scores in Parkinson's Disease. Organization for Human Brain Mapping. Vancouver, Canada, June 25-29, 2017. (poster)
9. Arslan DB, Kicik A, Cengiz S, Erdogan E, Buker S, Tufekcioglu Z, Ulug AM, Bilgic B, Gurvit H, Demiralp T, Tuzun E, Hanagasi H, Ozturk-Isik E. Cerebral Perfusion Correlates of MAPT and COMT Genotypes for Mild Cognitive Impairment in Parkinson's Disease at 3T. International Society of Magnetic Resonance in Medicine Annual Conference. Honolulu, HI, USA, April 22-27, 2017. (poster)
10. Arslan DB, Cengiz S, Erdogan E, Kicik A, Hatay GH, Tufekcioglu Z, Bilgic B, Hanagasi H, Ulug AM, Gurvit H, Demiralp T, Ozturk-Isik E. Comparison of cerebral blood volume and arterial blood volume between Parkinson's disease patients with mild cognitive impairment and normal cognition using arterial spin labeling MR at 3T. European Society of Magnetic Resonance in Medicine and Biology Annual Conference. Vienna, Austria, September 29 - October 1, 2016 (oral presentation)

Not first author

1. Václavů L, Arslan DB, Hirschler L, Ozturk-Isik E, Falcon C, Gispert JD, Montesinos P, Ven K, Osch MJP. Investigation of angiographic shine-through in time-encoded pCASL. International Society for Magnetic Resonance in Medicine. Vancouver, BC, Canada, 15-20 May, 2021. (poster)
2. Azamat S, Cengiz S, Arslan DB, Kicik A, Erdogan E, Bilgic B, Hanagasi H, Gurvit H, Demiralp T, Ozturk-Isik E. Determination of Cognitive Impairment in Parkinson's Disease Using Proton Magnetic Resonance Spectroscopic Imaging Based Biomarkers, European Society of Magnetic Resonance in Medicine and Biology Annual Conference. Virtual Meeting, September 30-October 2, 2020. (poster)

3. Tuncer S, Arslan DB, Deniz TI, Aslan O, Kicik A, Eryurek K, Erdogdu E, Yildirim Z, Tufekcioglu Z, Bilgic B, Hanagasi H, Gurvit H, Demiralp T, Ozturk-Isik E. The Evaluation of Cerebral Blood Flow Deficits in Parkinson's Disease Dementia using ASL-MRI at 3T. International Society for Magnetic Resonance in Medicine. Virtual Meeting, August 8-14, 2020. (poster)
4. Cengiz S, Yildirim Z, Arslan DB, Kicik A, Erdogdu E, Yildirim M, Tufekcioglu Z, Bilgic B, Hanagasi H, Ulug AM, Gurvit IH, Demiralp T, Ozturk-Isik E. MRSI Based Biomarkers of Parkinson's Disease with Mild Cognitive Impairment at Resting State fMRI Based Brain Parcellations. Alzheimer's Association International Conference. Los Angeles, USA, July 14-18, 2019. (poster)
5. Cengiz C, Arslan DB, Kicik A, Erdogdu E, Yildirim M, Tufekcioglu Z, Bilgic B, Hanagasi H, Ulug AM, Gurvit H, Demiralp T, and Ozturk-Isik E. Magnetic resonance spectroscopic imaging-based biomarkers of Parkinson's disease with mild cognitive impairment registered to MNI152 brain atlas after chemical shift correction. International Society for Magnetic Resonance in Medicine. Paris, France, June 16-21, 2018. (oral power pitch presentation)
6. Erdogdu E, Kicik A, Arslan DB, Cengiz S, Buker S, Tufekcioglu Z, Ozturk-Isik E, Bilgic B, Hanagasi H, Ulug AM, Basar-Eroglu C, Gurvit H, Demiralp T. DTI measures to track cognitive decline in Parkinson's disease with MCI and Dementia. Rome, Italy, June 9-13, 2019. (poster)
7. Ay U, Erdogdu E, Kicik A, Bayram A, Arslan D, Tufekcioglu Z, Cengiz S, Ozturk-Isik E, Bilgic B, Hanagasi H, Ulug AM, Gurvit H, Demiralp T. Structural Changes in Neurocognitive Networks Related with Cognitive Decline in Parkinson's Disease. Organization for Human Brain Mapping. Rome, Italy, June 9-13, 2019. (poster)
8. Ozturk-Isik E, Cengiz S, Arslan DB, Kicik A, Erdogdu E, Tufekcioglu Z, Bilgic B, Hanagasi H, Ulug AM, Demiralp T, Gurvit H. Machine Learning for Classification of Mild Cognitive Impairment in Parkinson's Disease Based on Multiparametric MRI at 3T. European Society of Magnetic Resonance in Medicine and Biology Annual Conference. Barcelona, Spain, 19-21 October 2017. (poster)

9. Cengiz S, Arslan DB, Kicik A, Erdogdu E, Buker S, Tufekcioglu Z, Ulug AM, Bilgic B, Hanagasi H, Gurvit H, Demiralp T, Ozturk-Isik E. Correlation of MRSI based biomarkers and neuropsychological test scores in Parkinson's disease at 3T. Organization for Human Brain Mapping. Vancouver, Canada, June 25-29, 2017. (poster)
10. Cengiz S, Arslan DB, Kicik A, Erdogdu E, Buker S, Tufekcioglu Z, Ulug AM, Bilgic B, Hanagasi H, Gurvit H, Demiralp T, Ozturk-Isik E. Correlation of cerebral perfusion and metabolic biomarker in Parkinson's disease with mild cognitive impairment using ASL-MRI and 1H-MRSI at 3T. Organization for Human Brain Mapping (OHBM). Vancouver, Canada, June 25-29, 2017. (poster)
11. Erdogdu E, Kicik A, Buker S, Tufekcioglu Z, Arslan DB, Cengiz S, Ozturk-Isik E, Bilgic B, Hanagasi H, Ulug AM, Eroglu CB, Demiralp T, Gurvit H. Functional connectivity changes at different stages of cognitive decline in Parkinson's disease. Organization for Human Brain Mapping (OHBM). Vancouver, Canada, June 25-29, 2017. (poster)
12. Ulug AM, Ozturk-Isik E, Kicik A, Erdogdu E, Cengiz S, Arslan DB, Bayram A, Ulasoglu-Yildiz C, Kurt E, Tufekcioglu Z, Bilgic B, Hanagasi H, Demiralp T, Gurvit H. Diffusion discriminant for mild cognitive impairment in Parkinson's disease. International Society of Magnetic Resonance in Medicine Annual Conference. Honolulu, HI, USA, April 22-27, 2017. (poster)
13. Cengiz S, Kicik A, Erdogdu E, Arslan DB, Buker S, Tufekcioglu Z, Ulug AM, Bilgic B, Gurvit H, Demiralp T, Tuzun E, Hanagasi H, Ozturk-Isik E. Comparison of MR spectroscopic imaging findings between different MAPT and COMT genotypes of cognitively normal or mild cognitively impaired Parkinson's disease patients at 3T. International Society of Magnetic Resonance in Medicine Annual Conference. Honolulu, HI, USA, April 22-27, 2017. (poster)
14. Cengiz S, Arslan DB, Erdogdu E, Kicik A, Hatay GH, Tufekcioglu Z, Bilgic B, Hanagasi H, Ulug AM, Gurvit H, Demiralp T, Ozturk-Isik E. Proton MR spectroscopic imaging of Parkinson's disease with mild cognitive impairment or normal

cognition registered to MNI152 brain atlas. European Society of Magnetic Resonance in Medicine and Biology Annual Conference. Vienna, Austria, September 29 - October 1, 2016. (oral presentation)

## **National Conference Proceedings and Abstracts**

### First author

1. Arslan DB, Yildirim Z, Cengiz S, Kicik A, Erdogdu E, Tufekcioglu Z, Bilgic B, Hanagasi H, Ulug AM, Demiralp T, Gurvit H, Ozturk Isik E. Parkinson Hastalığında MAPT Genotiplerinde Korteks Parselasyonlarında Serebral Kan Akımı Değişiklikleri. Ulusal Nöroloji Kongresi. Antalya, Turkey, November 16-20, 2019. (oral presentation)
2. Arslan DB, Cengiz S, Erdogdu E, Kicik A, Hatay GH, Tufekcioglu Z, Bilgic B, Hanagasi H, Ulug AM, Gurvit H, Demiralp T, Ozturk-Isik E. Atardamar Fırl Etiketleme Manyetik Rezonans Görüntüleme Tekniği Kullanılarak Kognitif Normal ve Hafif Kognitif Bozukluğu olan Parkinson Hastalarının Serebral Kan Akım Değerlerinin Karşılaştırılması. Türk Manyetik Rezonans Derneği. 2016. Ankara, Turkey, May 26-28, 2016. (oral presentation)
3. Arslan DB, Cengiz S, Erdogdu E, Kicik A, Tufekcioglu Z, Bilgic B, Hanagasi H, Ulug AM, Gurvit H, Demiralp T, Ozturk-Isik E. ASL-MR ile Parkinson hastalığı hafif kognitif bozukluğunda serebral perfüzyon değerlendirmesi. Ulusal Sinirbilim Kongresi, Istanbul, Turkey, May 20-23, 2018. (oral presentation)

### Not first author

1. Cengiz S, Yildirim Z, Arslan DB, Kicik A, Erdogdu E, Yildirim M, Tufekcioglu Z, Bilgic B, Hanagasi H, Ulug AM, Gurvit H, Demiralp T, Ozturk Isik E. Parkinson Hastalığı Hafif Kognitif Bozukluğunun Korteks Parselasyonlarında MR Spek-

- trooskopik Görüntüleme Temelli Biyoışaretleyicileri. Ulusal Nöroloji Kongresi. Antalya, Turkey, November 16-20, 2019. (oral Presentation)
2. Tufekcioglu Z, Cebi M, Tuncer S, Arslan DB, Ipek TD, Aslan O, Cengiz S, Kicik A, Erdogdu E, Yildirim Z, Bilgic B, Hanagasi H, Ulug AM, Demiralp T, Gurvit H ve Ozturk Isik E. Parkin Gen Mutasyonu Taşıyan Bireylerde Serebral Kan Akımının Değerlendirilmesi ve Kognitif Normal Parkinson Hastaları ile Karşılaştırılması. Ulusal Nöroloji Kongresi. Antalya, Turkey, November 16-20, 2019. (oral Presentation)
  3. Tuncer S, Arslan DB, Ipek TD, Aslan O, Cengiz S, Kicik A, Erdogdu E, Yildirim Z, Tufekcioglu Z, Bilgic B, Hanagasi H, Ulug AM, Demiralp T, Gurvit H, Ozturk-Isik E. Parkinson Hastalarında Kognitif Bozulmanın Arteriyel Spin Etiketleme Manyetik Rezonans Görüntüleme Temelli Biyoışaretleyicilerinin Değerlendirilmesi. Ulusal Nöroloji Kongresi. Antalya, Turkey, November 16-20, 2019. (oral Presentation)
  4. Erdogdu E, Kicik A, Buker S, Tufekcioglu Z, Arslan DB, Cengiz S, Ozturk-Isik E, Bilgic B, Hanagasi H, Ulug AM, Basar-Eroglu C, Gurvit H, Demiralp T. Parkinson Hastalığı Demansının Beyin İşlevsel Bağlantısallık Özellikleri. Ulusal Nöroloji Kongresi. Antalya, Turkey, November 16-20, 2019. (poster)
  5. Genc O, Arslan DB, Cengiz S, Hatay GH, Kicik A, Erdogdu E, Kaplan OC, Tufekcioglu Z, Bilgic B, Hanagasi H, Gurvit H, Demiralp T, Ulug AM, Ozturk-Isik E. Parkinson hastalığı hafif kognitif bozukluğunun MRG temelli makine öğrenme ile sınıflandırılması. Ulusal Sinirbilim Kongresi. Istanbul, Turkey, May 20-23, 2018. (Oral Presentation)
  6. Kicik A, Erdogdu E, Arslan DB, Cengiz S, Bilgic B, Tufekcioglu Z, Hanagasi H, Ulug AM, Tuzun E, Demiralp T, Ozturk-Isik E, Gurvit H. Parkinson hastalığında kognitif bozulmayla ilişkili yapısal ve fonksiyonel farklılıklar. Ulusal Sinirbilim Kongresi. Istanbul, Turkey, May 20-23, 2018. (Oral Presentation)
  7. Kaplan OC, Arslan DB, Cengiz S, Kicik A, Erdogdu E, Hatay GH, Tufekcioglu Z, Bilgic B, Hanacasi H, Gurvit H, Demiralp T, Ulug AM, Ozturk-Isik E. Parkin-

- son Hastalığı Hafif Kognitif Bozukluğunun Difüzyon Ağırlıklı Manyetik Rezonans Görüntüleme Temelli Biyoişaretleyicilerinin Belirlenmesi. Biyomut. Istanbul, Turkey, November 24-26, 2017. (Poster)
8. Kicik A, Erdogdu E, Tufekcioglu Z, Arslan DB, Cengiz S, Buker S, Bilgic B, Hanagasi H, Ulug AM, Basar-Eroglu C, Tuzun E, Demiralp T, Ozturk-Isik E, Gurvit H. Parkinson hastalığında kognitif bozulma ve beyin fonksiyonel bağlantısallık ağları. Ulusal Sinirbilim Kongresi. Sakarya, Turkey. May 7-10, 2017.
  9. Hatay GH, Arslan DB, Cebebi H, Okeer E, Hakyemez B, Ozturk-Isik E. Sıkıştırılmış Algılama ile Atardamar Fırl İşaretleme Tekniğinin Beyin Tümörlerinde Hızlandırılması için Uygunluğunun Araştırılması. Türk Manyetik Rezonans Derneği. 2016. Ankara, Turkey. 26-28 May 2016. (oral presentation)
  10. Cengiz S, Arslan DB, Erdogdu E, Kicik A, Hatay GH, Tufekcioglu Z, Bilgic B, Hanagasi H, Ulug AM, Gurvit H, Demiralp T, Ozturk-Isik E. Hafif Kognitif Bozukluğu Olan ve Kognitif Normal Parkinson Hastalarının Üç Boyutlu 1H Manyetik Rezonans Spektroskopik Görüntüleme Verilerinin Karşılaştırılması. Türk Manyetik Rezonans Derneği. 2016. Ankara, Turkey, May 26-28, 2016. (oral presentation)
  11. Kicik A, Erdogdu E, Buker S, Tufekcioglu Z, Arslan DB, Cengiz S, Ozturk-Isik E, Bilgic B, Hanagasi H, Ulug AM, Gurvit H. Parkinson hastalığında hafif kognitif bozuklukla ilişkili dinlenim durumu fonksiyonel bağlantısallık ağları. 14.Ulusal Sinir Bilm Kongresi 2016. Ankara, Turkey, May 26-29, 2016.

## REFERENCES

1. Rosner, J., V. Reddy, and F. Lui, "Neuroanatomy, circle of willis," *StatPearls*, 2021.
2. Smith, K. J., and P. N. Ainslie, "Regulation of cerebral blood flow and metabolism during exercise," *Experimental Physiology*, Vol. 102, no. 11, pp. 1356–1371, 2017.
3. Brooks, D. J., K. A. Frey, K. L. Marek, D. Oakes, D. Paty, R. Prentice, C. W. Shults, and A. J. Stoessl, "Assessment of neuroimaging techniques as biomarkers of the progression of Parkinson's disease," *Experimental Neurology*, Vol. 184 Suppl 1, pp. S68–79, 2003.
4. Wahl, R. L., J. M. Herman, and E. Ford, "The promise and pitfalls of positron emission tomography and single-photon emission computed tomography molecular imaging-guided radiation therapy," *Seminars in Radiation Oncology*, Vol. 21, no. 2, pp. 88–100, 2011.
5. Liu, T. T., and G. G. Brown, "Measurement of cerebral perfusion with arterial spin labeling: Part 1. Methods," *Journal of the International Neuropsychological Society*, Vol. 13, no. 3, pp. 517–525, 2007.
6. Williams, D. S., J. A. Detre, J. S. Leigh, and A. P. Koretsky, "Magnetic resonance imaging of perfusion using spin inversion of arterial water," *Proceedings of the National Academy of Sciences of the United States of America*, Vol. 89, no. 1, pp. 212–6, 1992.
7. Buxton, R. B., L. R. Frank, E. C. Wong, B. Siewert, S. Warach, and R. R. Edelman, "A general kinetic model for quantitative perfusion imaging with arterial spin labeling," *Magnetic Resonance in Medicine*, Vol. 40, no. 3, pp. 383–96, 1998.
8. Gunther, M., M. Bock, and L. R. Schad, "Arterial spin labeling in combination with a look-locker sampling strategy: inflow turbo-sampling EPI-FAIR (ITS-FAIR)," *Magnetic Resonance in Medicine*, Vol. 46, no. 5, pp. 974–84, 2001.
9. Petcharunpaisan, S., J. Ramalho, and M. Castillo, "Arterial spin labeling in neuroimaging," *World Journal of Radiology*, Vol. 2, no. 10, pp. 384–98, 2010.
10. Alsop, D. C., J. A. Detre, X. Golay, M. Gunther, J. Hendrikse, L. Hernandez-Garcia, H. Z. Lu, B. J. MacIntosh, L. M. Parkes, M. Smits, M. J. P. van Osch, D. J. J. Wang, E. C. Wong, and G. Zaharchuk, "Recommended Implementation of Arterial Spin-Labeled Perfusion MRI for Clinical Applications: a Consensus of the ISMRM Perfusion Study Group and the European Consortium for ASL in Dementia," *Magnetic Resonance in Medicine*, Vol. 73, no. 1, pp. 102–116, 2015.
11. Dixon, W. T., M. Sardashti, M. Castillo, and G. P. Stomp, "Multiple inversion recovery reduces static tissue signal in angiograms," *Magnetic Resonance in Medicine*, Vol. 18, no. 2, pp. 257–68, 1991.
12. Alsop, D. C., and J. A. Detre, "Reduced transit-time sensitivity in noninvasive magnetic resonance imaging of human cerebral blood flow," *Journal of Cerebral Blood Flow and Metabolism*, Vol. 16, no. 6, pp. 1236–49, 1996.
13. Gunther, M., "Highly efficient accelerated acquisition of perfusion inflow series by cycled arterial spin labeling," *In Proceedings of the 16th Annual Meeting of the International Society for Magnetic Resonance in Medicine*, 2007.

14. Suzuki, Y., M. Helle, P. Koken, M. Van Cauteren, and M. J. P. van Osch, "Simultaneous acquisition of perfusion image and dynamic MR angiography using time-encoded pseudo-continuous ASL," *Magnetic Resonance in Medicine*, Vol. 79, no. 5, pp. 2676–2684, 2018.
15. van Osch, M. J., W. M. Teeuwisse, Z. Chen, Y. Suzuki, M. Helle, and S. Schmid, "Advances in arterial spin labelling MRI methods for measuring perfusion and collateral flow," *Journal of Cerebral Blood Flow and Metabolism*, p. 271678X17713434, 2017.
16. Yu, R., and F. Lui, "Neuroanatomy, brain arteries," *StatPearls*, 2021.
17. Rosengarten, B., O. Huwendiek, and M. Kaps, "Neurovascular coupling and cerebral autoregulation can be described in terms of a control system," *Ultrasound in Medicine and Biology*, Vol. 27, no. 2, pp. 189–193, 2001.
18. Armstead, W. M., "Cerebral blood flow autoregulation and dysautoregulation," *Anesthesiology Clinics*, Vol. 34, no. 3, pp. 465–477, 2016.
19. Phillips, A. A., F. H. Chan, M. M. Zheng, A. V. Krassioukov, and P. N. Ainslie, "Neurovascular coupling in humans: Physiology, methodological advances and clinical implications," *Journal of Cerebral Blood Flow and Metabolism*, Vol. 36, no. 4, pp. 647–64, 2016.
20. Kety, S. S., and C. F. Schmidt, "The determination of cerebral blood flow in man by the use of nitrous oxide in low concentrations," *American Journal of Physiology-Legacy Content*, Vol. 143, no. 1, pp. 53–66, 1945.
21. Roguin, A., "Adolf Eugen Fick (1829-1901) - the man behind the cardiac output equation," *The American Journal of Cardiology*, Vol. 133, pp. 162–165, 2020.
22. Meier, P., and K. L. Zierler, "On the theory of the indicator-dilution method for measurement of blood flow and volume," *Journal of Applied Physiology*, Vol. 6, no. 12, pp. 731–44, 1954.
23. Zierler, K. L., "Theoretical basis of indicator-dilution methods for measuring flow and volume," *Circulation Research*, Vol. 10, no. 3, pp. 393–407, 1962.
24. Jiang, J. J., L. Y. Zhao, Y. Zhang, S. Zhang, Y. H. Yao, Y. Y. Qin, C. Y. Wang, and W. Z. Zhu, "Comparative analysis of arterial spin labeling and dynamic susceptibility contrast perfusion imaging for quantitative perfusion measurements of brain tumors," *International Journal of Clinical and Experimental Pathology*, Vol. 7, no. 6, pp. 2790–2799, 2014.
25. Petrou, M., V. Kotagal, and N. I. Bohnen, "An update on brain imaging in parkinsonian dementia," *Imaging in Medicine*, Vol. 4, no. 2, pp. 201–213, 2012.
26. van Gelderen, P., J. A. de Zwart, and J. H. Duyn, "Pitfalls of MRI measurement of white matter perfusion based on arterial spin labeling," *Magnetic Resonance in Medicine*, Vol. 59, no. 4, pp. 788–95, 2008.
27. Garcia, D., C. De Bazelaire, and D. Alsop, "Pseudo-continuous flow driven adiabatic inversion for arterial spin labeling," in *Proceedings of the 13th Annual Meeting of the International Society for Magnetic Resonance in Medicine*, Vol. 13, p. 37.
28. Detre, J. A., J. S. Leigh, D. S. Williams, and A. P. Koretsky, "Perfusion imaging," *Magnetic Resonance in Medicine*, Vol. 23, no. 1, pp. 37–45, 1992.

29. Ye, F. Q., J. A. Frank, D. R. Weinberger, and A. C. McLaughlin, "Noise reduction in 3D perfusion imaging by attenuating the static signal in arterial spin tagging (ASSIST)," *Magnetic Resonance in Medicine*, Vol. 44, no. 1, pp. 92–100, 2000.
30. Alsop, D., and J. Detre, "Background suppressed 3D RARE arterial spin labeled perfusion MRI," *Proceedings of the 7th Scientific Meeting of the International Society for Magnetic Resonance in Medicine*, p. 601, 1999.
31. Garcia, D. M., G. Duhamel, and D. C. Alsop, "Efficiency of inversion pulses for background suppressed arterial spin labeling," *Magnetic Resonance in Medicine: An Official Journal of the International Society for Magnetic Resonance in Medicine*, Vol. 54, no. 2, pp. 366–372, 2005.
32. Mani, S., J. Pauly, S. Conolly, C. Meyer, and D. Nishimura, "Background suppression with multiple inversion recovery nulling: applications to projective angiography," *Magnetic Resonance in Medicine*, Vol. 37, no. 6, pp. 898–905, 1997.
33. Maleki, N., W. Dai, and D. C. Alsop, "Optimization of background suppression for arterial spin labeling perfusion imaging," *Magma*, Vol. 25, no. 2, pp. 127–33, 2012.
34. Dai, W., P. Robson, A. Shankaranarayanan, and D. Alsop, "Benefits of interleaved continuous labeling and background suppression," *Proceedings of the 18th Annual Meeting of the International Society for Magnetic Resonance in Medicine*, p. 1748, 2010.
35. Aslan, S., F. Xu, P. L. Wang, J. Uh, U. S. Yezhuvath, M. Van Osch, and H. Lu, "Estimation of labeling efficiency in pseudocontinuous arterial spin labeling," *Magnetic Resonance in Medicine*, Vol. 63, no. 3, pp. 765–771, 2010.
36. Hales, P. W., F. J. Kirkham, and C. A. Clark, "A general model to calculate the spin-lattice (T1) relaxation time of blood, accounting for haematocrit, oxygen saturation and magnetic field strength," *Journal of Cerebral Blood Flow and Metabolism*, Vol. 36, no. 2, pp. 370–4, 2016.
37. MacIntosh, B. J., A. C. Lindsay, I. Kyntireas, W. Kuker, M. Gunther, M. D. Robson, J. Kennedy, R. P. Choudhury, and P. Jezzard, "Multiple inflow pulsed arterial spin-labeling reveals delays in the arterial arrival time in minor stroke and transient ischemic attack," *American Journal of Neuroradiology*, Vol. 31, no. 10, pp. 1892–4, 2010.
38. Skurdal, M. J., A. Bjornerud, M. J. P. van Osch, W. Nordhoy, J. Lagopoulos, and I. R. Groote, "Voxel-wise perfusion assessment in cerebral white matter with PCASL at 3T; is it possible and how long does it take?," *PloS one*, Vol. 10, no. 8, pp. e0135596–e0135596, 2015.
39. Look, D. C., "Time saving in measurement of NMR and EPR relaxation times," *Review of Scientific Instruments*, Vol. 41, no. 2, p. 250, 1970.
40. Gowland, P., and P. Mansfield, "Accurate measurement of T1 in vivo in less than 3 seconds using echo-planar imaging," *Magnetic Resonance in Medicine*, Vol. 30, no. 3, pp. 351–4, 1993.
41. Petersen, E. T., T. Lim, and X. Golay, "Model-free arterial spin labeling quantification approach for perfusion MRI," *Magnetic Resonance in Medicine*, Vol. 55, no. 2, pp. 219–32, 2006.

42. Dai, W., A. Shankaranarayanan, and D. C. Alsop, "Volumetric measurement of perfusion and arterial transit delay using hadamard encoded continuous arterial spin labeling," *Magnetic Resonance in Medicine*, Vol. 69, no. 4, pp. 1014–22, 2013.
43. von Samson-Himmelstjerna, F., V. I. Madai, J. Sobesky, and M. Guenther, "Walsh-ordered hadamard time-encoded pseudocontinuous ASL (WH pCASL)," *Magnetic Resonance in Medicine*, Vol. 76, no. 6, pp. 1814–1824, 2016.
44. Teeuwisse, W. M., S. Schmid, E. Ghariq, I. M. Veer, and M. J. P. van Osch, "Time-encoded pseudocontinuous arterial spin labeling: Basic properties and timing strategies for human applications," *Magnetic Resonance in Medicine*, Vol. 72, no. 6, pp. 1712–1722, 2014.
45. Ross, C. A., and M. A. Poirier, "Protein aggregation and neurodegenerative disease," *Nature Medicine*, Vol. 10, no. 7, pp. S10–S17, 2004.
46. Kisler, K., A. R. Nelson, A. Montagne, and B. V. Zlokovic, "Cerebral blood flow regulation and neurovascular dysfunction in Alzheimer disease," *Nature Reviews Neuroscience*, Vol. 18, no. 7, pp. 419–434, 2017.
47. Alosco, M. L., J. Gunstad, B. A. Jerskey, X. Xu, U. S. Clark, J. Hassenstab, D. M. Cote, E. G. Walsh, D. R. Labbe, R. Hoge, R. A. Cohen, and L. H. Sweet, "The adverse effects of reduced cerebral perfusion on cognition and brain structure in older adults with cardiovascular disease," *Brain and Behavior*, Vol. 3, no. 6, pp. 626–636, 2013.
48. Roher, A. E., J. P. Debbins, M. Malek-Ahmadi, K. Chen, J. G. Pipe, S. Maze, C. Belden, C. L. Maarouf, P. Thiyyagura, H. Mo, J. M. Hunter, T. A. Kokjohn, D. G. Walker, J. C. Kruchowsky, M. Belohlavek, M. N. Sabbagh, and T. G. Beach, "Cerebral blood flow in Alzheimer's disease," *Vascular health and risk management*, Vol. 8, pp. 599–611, 2012.
49. Melzer, T. R., R. Watts, M. R. MacAskill, J. F. Pearson, S. Rueger, T. L. Pitcher, L. Livingston, C. Graham, R. Keenan, A. Shankaranarayanan, D. C. Alsop, J. C. Dalrymple-Alford, and T. J. Anderson, "Arterial spin labelling reveals an abnormal cerebral perfusion pattern in Parkinson's disease," *Brain*, Vol. 134, no. Pt 3, pp. 845–55, 2011.
50. Syrimi, Z. J., L. Vojtisek, I. Eliasova, J. Viskova, A. Svatkova, J. Vanicek, and I. Rektorova, "Arterial spin labelling detects posterior cortical hypoperfusion in non-demented patients with Parkinson's disease," *Journal of Neural Transmission*, Vol. 124, no. 5, pp. 551–557, 2017.
51. Kamagata, K., Y. Motoi, M. Hori, M. Suzuki, A. Nakanishi, K. Shimoji, S. Kyougoku, R. Kuwatsuru, K. Sasai, O. Abe, Y. Mizuno, S. Aoki, and N. Hattori, "Posterior hypoperfusion in Parkinson's disease with and without dementia measured with arterial spin labeling MRI," *Journal of Magnetic Resonance Imaging*, Vol. 33, no. 4, pp. 803–7, 2011.
52. Fernandez-Seara, M. A., E. Mengual, M. Vidorreta, M. Aznarez-Sanado, F. R. Loayza, F. Villagra, J. Irigoyen, and M. A. Pastor, "Cortical hypoperfusion in Parkinson's disease assessed using arterial spin labeled perfusion MRI," *Neuroimage*, Vol. 59, no. 3, pp. 2743–50, 2012.
53. Wei, X. B., R. H. Yan, Z. Y. Chen, R. H. Weng, X. Liu, H. M. Gao, X. F. Xu, Z. Kang, Z. X. Liu, Y. Guo, Z. H. Liu, J. P. Larsen, J. Wang, B. S. Tang, M. Hallett, and Q. Wang, "Combined diffusion tensor imaging and arterial spin labeling as markers of early Parkinson's disease," *Scientific Reports*, Vol. 6:33762, 2016.

54. Yamashita, K., A. Hiwatashi, O. Togao, K. Kikuchi, H. Yamaguchi, Y. Suzuki, R. Kamei, R. Yamasaki, J. Kira, and H. Honda, "Cerebral blood flow laterality derived from arterial spin labeling as a biomarker for assessing the disease severity of Parkinson's disease," *Journal of Magnetic Resonance Imaging*, Vol. 45, no. 6, pp. 1821–1826, 2017.
55. Le Heron, C. J., S. L. Wright, T. R. Melzer, D. J. Myall, M. R. MacAskill, L. Livingston, R. J. Keenan, R. Watts, J. C. Dalrymple-Alford, and T. J. Anderson, "comparing cerebral perfusion in alzheimer's disease and parkinson's disease dementia: an asl-mri study,"
56. Jia, X., Y. Li, K. Li, P. Liang, and X. Fu, "Precuneus dysfunction in Parkinson's disease with mild cognitive impairment," *Frontiers in Aging Neuroscience*, Vol. 10, p. 427, 2018.
57. Hasselbalch, S. G., G. Oberg, S. A. SÃrensen, A. R. Andersen, G. Waldemar, J. F. Schmidt, K. Fenger, and O. B. Paulson, "Reduced regional cerebral blood flow in Huntington's disease studied by SPECT," *Journal of Neurology, Neurosurgery and; Psychiatry*, Vol. 55, no. 11, pp. 1018–1023, 1992.
58. Liepelt-Scarfone, I., S. Graeber, A. Feseker, G. Baysal, J. Godau, A. Gaenslen, W. Maetzler, and D. Berg, "Influence of different cut-off values on the diagnosis of mild cognitive impairment in Parkinson's disease," *Parkinson's Disease*, p. 540843, 2011.
59. Hughes, A. J., S. E. Daniel, L. Kilford, and A. J. Lees, "Accuracy of clinical diagnosis of idiopathic Parkinson's disease: a clinico-pathological study of 100 cases," *Journal of Neurology, Neurosurgery, and Psychiatry*, Vol. 55, no. 3, pp. 181–4, 1992.
60. Braak, H., K. Del Tredici, U. Rub, R. A. de Vos, E. N. Jansen Steur, and E. Braak, "Staging of brain pathology related to sporadic Parkinson's disease," *Neurobiology of Aging*, Vol. 24, no. 2, pp. 197–211, 2003.
61. Alexander, G. E., M. R. DeLong, and P. L. Strick, "Parallel organization of functionally segregated circuits linking basal ganglia and cortex," *Annual Review of Neuroscience*, Vol. 9, pp. 357–81, 1986.
62. Muslimovic, D., B. Post, J. D. Speelman, and B. Schmand, "Cognitive profile of patients with newly diagnosed Parkinson's disease," *Neurology*, Vol. 65, no. 8, pp. 1239–45, 2005.
63. Litvan, I., D. Aarsland, C. H. Adler, J. G. Goldman, J. Kulisevsky, B. Mollenhauer, M. C. Rodriguez-Oroz, A. I. Troster, and D. Weintraub, "MDS Task Force on mild cognitive impairment in Parkinson's disease: critical review of PD-MCI," *Movement Disorders*, Vol. 26, no. 10, pp. 1814–24, 2011.
64. Janvin, C. C., J. P. Larsen, D. Aarsland, and K. Hugdahl, "Subtypes of mild cognitive impairment in Parkinson's disease: progression to dementia," *Movement Disorders*, Vol. 21, no. 9, pp. 1343–9, 2006.
65. Martinez-Horta, S., and J. Kulisevsky, "Is all cognitive impairment in Parkinson's disease "mild cognitive impairment"?", *Journal of Neural Transmission*, Vol. 118, no. 8, pp. 1185–90, 2011.
66. Kehagia, A. A., R. A. Barker, and T. W. Robbins, "Cognitive impairment in Parkinson's disease: the dual syndrome hypothesis," *Neurodegenerative Diseases*, Vol. 11, no. 2, pp. 79–92, 2013.

67. Litvan, I., J. G. Goldman, A. I. Troster, B. A. Schmand, D. Weintraub, R. C. Petersen, B. Mollenhauer, C. H. Adler, K. Marder, C. H. Williams-Gray, D. Aarsland, J. Kulisevsky, M. C. Rodriguez-Oroz, D. J. Burn, R. A. Barker, and M. Emre, "Diagnostic criteria for mild cognitive impairment in Parkinson's disease: Movement Disorder Society Task Force guidelines," *Movement Disorders*, Vol. 27, no. 3, pp. 349–56, 2012.
68. Yeo, B. T., F. M. Krienen, J. Sepulcre, M. R. Sabuncu, D. Lashkari, M. Hollinshead, J. L. Roffman, J. W. Smoller, L. Zollei, J. R. Polimeni, B. Fischl, H. Liu, and R. L. Buckner, "The organization of the human cerebral cortex estimated by intrinsic functional connectivity," *Journal of Neurophysiology*, Vol. 106, no. 3, pp. 1125–65, 2011.
69. Dosenbach, N. U., D. A. Fair, A. L. Cohen, B. L. Schlaggar, and S. E. Petersen, "A dual-networks architecture of top-down control," *Trends in Cognitive Sciences*, Vol. 12, no. 3, pp. 99–105, 2008.
70. Morley, J. F., S. X. Xie, H. I. Hurtig, M. B. Stern, A. Colcher, S. Horn, N. Dahodwala, J. E. Duda, D. Weintraub, A. S. Chen-Plotkin, V. Van Deerlin, D. Falcone, and A. Siderowf, "Genetic influences on cognitive decline in Parkinson's disease," *Movement Disorders*, Vol. 27, no. 4, pp. 512–8, 2012.
71. Nombela, C., J. B. Rowe, S. E. Winder-Rhodes, A. Hampshire, A. M. Owen, D. P. Breen, G. W. Duncan, T. K. Khoo, A. J. Yarnall, M. J. Firbank, P. F. Chinnery, T. W. Robbins, J. T. O'Brien, D. J. Brooks, D. J. Burn, I.-P. s. group, and R. A. Barker, "Genetic impact on cognition and brain function in newly diagnosed Parkinson's disease: ICICLE-PD study," *Brain*, Vol. 137, no. Pt 10, pp. 2743–58, 2014.
72. Goris, A., C. H. Williams-Gray, G. R. Clark, T. Foltynie, S. J. Lewis, J. Brown, M. Ban, M. G. Spillantini, A. Compston, D. J. Burn, P. F. Chinnery, R. A. Barker, and S. J. Sawcer, "Tau and alpha-synuclein in susceptibility to, and dementia in, Parkinson's disease," *Annals of Neurology*, Vol. 62, no. 2, pp. 145–53, 2007.
73. Williams-Gray, C. H., J. R. Evans, A. Goris, T. Foltynie, M. Ban, T. W. Robbins, C. Brayne, B. S. Kolachana, D. R. Weinberger, S. J. Sawcer, and R. A. Barker, "The distinct cognitive syndromes of Parkinson's disease: 5 year follow-up of the CamPaIGN cohort," *Brain*, Vol. 132, no. Pt 11, pp. 2958–69, 2009.
74. Schaefer, A., R. Kong, E. M. Gordon, T. O. Laumann, X. N. Zuo, A. J. Holmes, S. B. Eickhoff, and B. T. T. Yeo, "Local-global parcellation of the human cerebral cortex from intrinsic functional connectivity MRI," *Cerebral Cortex*, Vol. 28, no. 9, pp. 3095–3114, 2018.
75. Ishizaki, J., H. Yamamoto, T. Takahashi, M. Takeda, M. Yano, and M. Mimura, "Changes in regional cerebral blood flow following antidepressant treatment in late-life depression," *International Journal of Geriatric Psychiatry*, Vol. 23, no. 8, pp. 805–11, 2008.
76. Duckrow, R. B., "Regional cerebral blood flow during spreading cortical depression in conscious rats," *Journal of Cerebral Blood Flow and Metabolism*, Vol. 11, no. 1, pp. 150–4, 1991.
77. Uysal-Canturk, P., H. A. Hanagasi, B. Bilgic, H. Gurvit, and M. Emre, "An assessment of Movement Disorder Society Task Force diagnostic criteria for mild cognitive impairment in Parkinson's disease," *European Journal of Neurology*, Vol. 25, no. 1, pp. 148–153, 2018.

78. Hoehn, M. M., and M. D. Yahr, "Parkinsonism: onset, progression and mortality," *Neurology*, Vol. 17, no. 5, pp. 427–42, 1967.
79. Goetz, C. G., B. C. Tilley, S. R. Shaftman, G. T. Stebbins, S. Fahn, P. Martinez-Martin, W. Poewe, C. Sampaio, M. B. Stern, R. Dodel, B. Dubois, R. Holloway, J. Jankovic, J. Kulisevsky, A. E. Lang, A. Lees, S. Leurgans, P. A. LeWitt, D. Nyenhuis, C. W. Olanow, O. Rascol, A. Schrag, J. A. Teresi, J. J. van Hilten, N. LaPelle, and U. R. T. F. Movement Disorder Society, "Movement Disorder Society-sponsored revision of the Unified Parkinson's Disease Rating Scale (MDS-UPDRS): scale presentation and clinimetric testing results," *Movement Disorders*, Vol. 23, no. 15, pp. 2129–70, 2008.
80. Perlmutter, J. S., "Assessment of Parkinson disease manifestations," *Current Protocols in Neuroscience*, Vol. Chapter 10, p. Unit10 1, 2009.
81. Nasreddine, Z., N. Phillips, V. Bedirian, S. Charbonneau, V. Whitehead, I. Collin, J. Cummings, and H. Chertkow, "The Montreal Cognitive Assessment, MOCA: A Brief Screening Tool For Mild Cognitive Impairment," *Journal of the American Geriatrics Society*, Vol. 53, 2005.
82. Mioshi, E., K. Dawson, J. Mitchell, R. Arnold, and J. R. Hodges, "The Addenbrooke's Cognitive Examination Revised (ACE-R): a brief cognitive test battery for dementia screening," *International Journal of Geriatric Psychiatry*, Vol. 21, no. 11, pp. 1078–85, 2006.
83. Folstein, M. F., S. E. Folstein, and P. R. McHugh, "'Mini-mental state'. A practical method for grading the cognitive state of patients for the clinician," *Journal of Psychiatric Research*, Vol. 12, no. 3, pp. 189–98, 1975.
84. Stroop, J. R., "Studies of interference in serial verbal reactions," *Journal of Experimental Psychology-General*, Vol. 121, no. 1, pp. 15–23, 1992.
85. Robinson, A. L., R. K. Heaton, R. A. Lehman, and D. W. Stilson, "The utility of the Wisconsin Card Sorting Test in detecting and localizing frontal lobe lesions," *Journal of Consulting and Clinical Psychology*, Vol. 48, no. 5, pp. 605–14, 1980.
86. Benton, A. L., K. D. Hamsher, N. R. Varney, and O. Spreen, "Contributions to neuropsychological assessment: a clinical manual," *Oxford University Press, USA*, 1983.
87. Smith, A., *The Symbol-Digit Modalities Test: a Neuropsychologic Test of Learning and Other Cerebral Disorders.*, Learning Disorders, Special Child Publication, 1968.
88. Kelley, C., "Iterative methods for optimization," *SIAM*, 1999.
89. Chappell, M. A., B. J. MacIntosh, M. J. Donahue, M. Gunther, P. Jezzard, and M. W. Woolrich, "Separation of macrovascular signal in multi-inversion time arterial spin labelling MRI," *Magnetic Resonance in Medicine*, Vol. 63, no. 5, pp. 1357–65, 2010.
90. Buckner, R. L., F. M. Krienen, A. Castellanos, J. C. Diaz, and B. T. Yeo, "The organization of the human cerebellum estimated by intrinsic functional connectivity," *Journal of Neurophysiology*, Vol. 106, no. 5, pp. 2322–45, 2011.
91. Chawla, N., K. Bowyer, L. Hall, and W. Kegelmeyer, "SMOTE: Synthetic minority oversampling technique," *Journal of Artificial Intelligence Research*, Vol. 16, pp. 321–357, 2002.

92. Liu, P., J. Uh, and H. Lu, "Determination of spin compartment in arterial spin labeling MRI," *Magnetic Resonance in Medicine*, Vol. 65, no. 1, pp. 120–7, 2011.
93. Abe, Y., T. Kachi, T. Kato, Y. Arahata, T. Yamada, Y. Washimi, K. Iwai, K. Ito, N. Yanagisawa, and G. Sobue, "Occipital hypoperfusion in Parkinson's disease without dementia: correlation to impaired cortical visual processing," *Journal of Neurology, Neurosurgery, and Psychiatry*, Vol. 74, no. 4, pp. 419–22, 2003.
94. Wolpert, D. H., *The relationship between PAC, the statistical physics framework, the Bayesian framework, and the VC framework*, pp. 117–214. CRC Press, 2018.
95. Blagus, R., and L. Lusa, "SMOTE for high-dimensional class-imbalanced data," *BMC Bioinformatics*, Vol. 14, p. 106, 2013.
96. Pievani, M., W. de Haan, T. Wu, W. W. Seeley, and G. B. Frisoni, "Functional network disruption in the degenerative dementias," *Lancet Neurology*, Vol. 10, no. 9, pp. 829–43, 2011.
97. Amboni, M., A. Tessitore, F. Esposito, G. Santangelo, M. Picillo, C. Vitale, A. Giordano, R. Erro, R. de Micco, D. Corbo, G. Tedeschi, and P. Barone, "Resting-state functional connectivity associated with mild cognitive impairment in Parkinson's disease," *Journal of Neurology*, Vol. 262, no. 2, pp. 425–34, 2015.
98. Bezdicek, O., T. Ballarini, F. Ruzicka, J. Roth, K. Mueller, R. Jech, and M. L. Schroeter, "Mild cognitive impairment disrupts attention network connectivity in Parkinson's disease: a combined multimodal MRI and meta-analytical study," *Neuropsychologia*, Vol. 112, pp. 105–115, 2018.
99. Diez-Cirarda, M., A. P. Strafella, J. Kim, J. Pena, N. Ojeda, A. Cabrera-Zubizarreta, and N. Ibarretxe-Bilbao, "Dynamic functional connectivity in Parkinson's disease patients with mild cognitive impairment and normal cognition," *NeuroImage: Clinical*, Vol. 17, pp. 847–855, 2018.
100. van Eimeren, T., O. Monchi, B. Ballanger, and A. P. Strafella, "Dysfunction of the default mode network in Parkinson disease: a functional magnetic resonance imaging study," *Archives of Neurology*, Vol. 66, no. 7, pp. 877–83, 2009.
101. Gorges, M., H. P. Muller, I. Liepelt-Scarfone, A. Storch, R. Dodel, L. Consortium, R. Hilker-Rogendorf, D. Berg, M. S. Kunz, E. Kalbe, S. Baudrexel, and J. Kassubek, "Structural brain signature of cognitive decline in Parkinson's disease: DTI-based evidence from the LANDSCAPE study," *Therapeutic Advances in Neurological Disorders*, Vol. 12, p. 1756286419843447, 2019.
102. Kamagata, K., Y. Motoi, H. Tomiyama, O. Abe, K. Ito, K. Shimoji, M. Suzuki, M. Hori, A. Nakanishi, T. Sano, R. Kuwatsuru, K. Sasai, S. Aoki, and N. Hattori, "Relationship between cognitive impairment and white-matter alteration in Parkinson's disease with dementia: tract-based spatial statistics and tract-specific analysis," *European Radiology*, Vol. 23, no. 7, pp. 1946–1955, 2013.
103. Hattori, T., S. Orimo, S. Aoki, K. Ito, O. Abe, A. Amano, R. Sato, K. Sakai, and H. Mizusawa, "Cognitive status correlates with white matter alteration in Parkinson's disease," *Human Brain Mapping*, Vol. 33, no. 3, pp. 727–739, 2012.

104. Wirth, M., A. Pichet Binette, P. Brunecker, T. Kobe, A. V. Witte, and A. Floel, "Divergent regional patterns of cerebral hypoperfusion and gray matter atrophy in mild cognitive impairment patients," *Journal of Cerebral Blood Flow and Metabolism*, Vol. 37, no. 3, pp. 814–824, 2017.
105. Asllani, I., A. Borogovac, and T. R. Brown, "Regression algorithm correcting for partial volume effects in arterial spin labeling MRI," *Magnetic Resonance in Medicine*, Vol. 60, no. 6, pp. 1362–71, 2008.
106. Dolui, S., M. Vidorreta, Z. Wang, I. M. Nasrallah, A. Alavi, D. A. Wolk, and J. A. Detre, "Comparison of PASL, PCASL, and background-suppressed 3D PCASL in mild cognitive impairment," *Human Brain Mapping*, Vol. 38, no. 10, pp. 5260–5273, 2017.
107. Shao, X., Y. Wang, S. Moeller, and D. J. J. Wang, "A constrained slice-dependent background suppression scheme for simultaneous multislice pseudo-continuous arterial spin labeling," *Magnetic resonance in medicine*, Vol. 79, no. 1, pp. 394–400, 2018.
108. Pollock, J. M., H. Tan, R. A. Kraft, C. T. Whitlow, J. H. Burdette, and J. A. Maldjian, "Arterial spin-labeled MR perfusion imaging: clinical applications," *Magnetic Resonance Imaging Clinics of North America*, Vol. 17, no. 2, pp. 315–38, 2009.
109. Deshmane, A., V. Gulani, M. A. Griswold, and N. Seiberlich, "Parallel MR imaging," *Journal of Magnetic Resonance Imaging*, Vol. 36, no. 1, pp. 55–72, 2012.
110. Cox, S. R., D. A. Dickie, S. J. Ritchie, S. Karama, A. Pattie, N. A. Royle, J. Corley, B. S. Aribisala, M. V. Hernandez, S. M. Maniega, J. M. Starr, M. E. Bastin, A. C. Evans, J. M. Wardlaw, and I. J. Deary, "Associations between education and brain structure at age 73 years, adjusted for age 11 IQ," *Neurology*, Vol. 87, no. 17, pp. 1820–1826, 2016.
111. Asllani, I., C. Habeck, N. Scarmeas, A. Borogovac, T. R. Brown, and Y. Stern, "Multivariate and univariate analysis of continuous arterial spin labeling perfusion MRI in Alzheimer's disease," *Journal of Cerebral Blood Flow and Metabolism*, Vol. 28, no. 4, pp. 725–36, 2008.
112. Ma, Y., C. Huang, J. P. Dyke, H. Pan, D. Alsop, A. Feigin, and D. Eidelberg, "Parkinson's disease spatial covariance pattern: noninvasive quantification with perfusion MRI," *Journal of Cerebral Blood Flow and Metabolism*, Vol. 30, no. 3, pp. 505–9, 2010.
113. Huang, C., P. Mattis, C. Tang, K. Perrine, M. Carbon, and D. Eidelberg, "Metabolic brain networks associated with cognitive function in Parkinson's disease," *Neuroimage*, Vol. 34, no. 2, pp. 714–23, 2007.
114. Huber, J., D. Hoinkiss, and M. Gunther, "Subject-specific background suppression in 3D pseudo-continuous arterial spin labeling perfusion imaging," *Proceedings of the 28th Annual Meeting of the International Society for Magnetic Resonance in Medicine*, 2020.
115. van der Plas, M. C. E., W. M. Teeuwisse, S. Schmid, M. Chappell, and M. J. P. van Osch, "High temporal resolution arterial spin labeling MRI with whole-brain coverage by combining time-encoding with Look-Locker and simultaneous multi-slice imaging," *Magnetic resonance in medicine*, Vol. 81, no. 6, pp. 3734–3744, 2019.